Synthesis of Transition Metal Dichalcogenides from Solid-Phase Precursors



A thesis presented to the University of Dublin, Trinity College

for the degree of

Doctor of Philosophy in Chemistry

by

John Mc Manus

Under the supervision of Prof. Georg Duesberg and Prof. Wolfgang Schmitt

School of Chemistry

Trinity College Dublin

2019

Declaration

I declare that this thesis has not been submitted as an exercise for a degree at this or any other university and it is entirely my own work.

I agree to deposit this thesis in the University's open access institutional repository or allow the library to do so on my behalf, subject to Irish Copyright Legislation and Trinity College Library conditions of use and acknowledgement.

. . . . . .

John Mc Manus B.A. (Mod.)

when she thought it over afterwards it occurred to her that she ought to have wondered at this, but at the time it all seemed quite natural

-Lewis Carroll, Alice's Adventures in Wonderland

Summary

A huge array of layered materials have been examined as potential 2-dimensional (2D) materials in recent years. Of these, one of the mostly widely studied classes have been transition metal dichalcogenides (TMDs) due to their varied properties and numerous potential applications. Nanoscale TMDs have been examined for use in logic electronics, light-emitting diodes, photovoltaics, spintronics, catalysis and sensing. Despite this, there remains many challenges associated with the growth of these materials, especially in a scalable fashion. Of the production processes that are scalable, many require high temperatures or long growth times, making them less industrially attractive. Some of the vapour-phase precursors can also be challenging to work with. These issues are especially pronounced for the less studied TMDs, such as those containing tellurium.

Unlike those containing sulfur or selenium, the majority of telluride TMDs are most stable in the octahedral or distorted octahedral structure. As a result of this, they are predominantly metallic or semimetallic, with some also displaying exotic physical phenomena. WTe_2 has demonstrated giant magnetoresistance and is also a type-II Weyl semimetal, while $PtTe_2$ is predicted to be a type-II Dirac semimetal. Aside from this, there is also interest in these materials for thermoelectrics, electronics and catalysis. The majority of research effort thus far has focussed on mechanically exfoliated flakes from chemical vapour transport (CVT) grown crystals of these materials, a very labour intensive production method. This presents an opportunity for research into more scalable and efficient growth of telluride TMDs.

The primary focus of this thesis is the scalable growth of tellurium containing TMDs through the conversion of pre-deposited metal and tellurium films. The growth of sulfide and selenide TMDs, using the thermally-assisted conversion (TAC) method of exposing pre-deposited metal films to chalcogen vapour, is initially examined. A new method for telluride films is then developed by adapting this TAC growth method. For the telluride TMDs, the tellurium is electrodeposited onto the transition metal layer prior to the furnace step. The two layers

are then reacted at close to atmospheric pressure to form the TMD. This avoids the need for vapour phase Te precursors, while still allowing strong control over reactant concentrations during the growth.

This process is applied to grow films of molybdenum ditelluride ($MoTe_2$), tungsten ditelluride (WTe_2) and platinum ditelluride ($PtTe_2$). These are thoroughly characterised using a range of spectroscopy and microscopy techniques. Both Raman and X-ray diffraction (XRD) of the films matched closely to previously reported bulk spectra for the respective materials. X-ray photoelectron spectroscopy (XPS) confirmed the growth of each material, while indicating that the surface oxidises to between 10% and 30%. WTe_2 was found to be most prone to oxidation, but this was shown to be limited to the surface of the film. All three telluride TMDs were found to grow at temperatures as low as 450 °C. This is on the lower end of reported growths in literature for $MoTe_2$ and WTe_2, while being the lowest reported value for $PtTe_2$. This large-scale, low-temperature growth offers an efficient was to produce TMDs films and could be further expanded to other materials.

Microscopy analysis found that all of the films had larger grain sizes than films grown by standard TAC. There was however significant differences between the morphology of each. $MoTe_2$ films were uniform with flakes measuring hundreds of nanometres at large angles to the surface. WTe_2 films had patches of flakes with lengths up to 10μm, surrounded by areas of much smaller flakes. The $PtTe_2$ films were found to contain flakes that were much more 3D in nature and did not cover the entire surface. The majority of the differences in morphologies were accounted for by the behaviour of the Te during the growth, namely the extent to which it dewet from the surface.

The films were examined for electrical and electrochemical applications. Initial electrical characterisation of single WTe_2 flakes yielded promising results. The application of the films as electrocatalysts of the hydrogen evolution reaction (HER) found that the most active was $PtTe_2$, while WTe_2 showed the least activity. The 1T' $MoTe_2$ gave results competitive with previous reports in literature and thicker films were shown to be more catalytically active. $PtTe_2$ films also demonstrated high electrocatalytic activity towards the oxygen reduction reaction (ORR). However, a caveat associated with this result is that the films appeared to lose Te during the measurements. Therefore, further studies are needed to verify that the results are due to the $PtTe_2$ and not the formation of a Pt rich phase.

Acknowledgements

Firstly I would like to thank Prof. Georg Duesberg for giving me the opportunity to complete my research in his group and for all his support, guidance and encouragement throughout. I would also like to thank Prof. Wolfgang Schmitt for his support in co-supervising the second half of my PhD. I would like to acknowledge the financial support that I have received from the Irish Research Council through their Postgraduate Scholarship Program.

It has been a pleasure to be part of the ASIN group over the last four years and there are a huge number of past and present members without whom I would have never managed to start my research project, to say nothing of completing it. I owe a great debt of gratitude to both Dr. Toby Hallam and Dr. Niall McEvoy for the training, guidance, advice, discussions and feedback they have provided throughout my PhD. I wouldn't have gotten it over the line without them. I would also like to thank Dr. Graeme Cunningham for all his help during my work on the telluride TMD growth process. Thanks to Mike Finneran, Julia Kremer, Neal O'Hara and all the technical staff in CRANN and the AML for always giving freely of their time and expertise for both training and fixing tools.

I would like to thank Conor Cullen for the numerous XPS measurements and analysis, Clive Dowling and Dr. Farzan Gity for TEM measurements, Dr. Michelle Browne and Dr. David McAteer for assistance with electrochemical characterisation and Dr. Daragh Mullarkey for XRD analysis. I would also like to thank Lisanne Peters for the fabrication of EBL devices.

I am exceptionally grateful to everybody else in the ASIN group, both past and present, for helping me with training, discussions and advice during my PhD - Dr. Maria O'Brien, Dr. Riley Gatensby, Dr. Sinead Winters, Dr. Christian Wirtz, Dr. Kangho Lee, Chris Murray, Dr. Maria Daniela Angione, Dr. Hugo Nolan, Katie O'Neill and Dr. Cormac Ó'Coileáin.

I would like to thank all of the summer and project students who I have had the pleasure of working and supervising throughout my PhD - Dominik Horvath,

Bastien Balsamo, Jean-Baptiste Salemme and Alison Hennessy. They contributed greatly to this thesis.

I would like to especially thank everyone who made CRANN more than just a work place over the last few years. The office and lab chats, lunches and general craic, these are what kept me going through the abundance of frustrating results and made it all worthwhile.

Thanks to all of the PCAM crew who have been a constant source of friendship and encouragement over the last decade. And to all my other friends who have always been there to keep me sane. To my parents who have always fully supported me in any and all decisions I make. To Emer, Martin and Claire (and Ciara, Sinead, Darragh and Niamh), thanks for the consistent reminders that gold medals aren't all that.

Finally, a special thanks to my girlfriend Shauna for her unwavering support and encouragement, and for listening to my many complaints about failed experiments. I wouldn't have gotten here without you.

Publications and Presentations

List of publications

1. "Growth of 1T' $MoTe_2$ by Thermally Assisted Conversion of Electrodeposited Tellurium film", *ACS Applied Energy Materials*, 2018, **2**, 521-530
   J. B. Mc Manus, G. Cunningham, N McEvoy, C. P. Cullen, F Gity, M. Schmidt, D. McAteer, D. Mullarkey, I. V. Shvets, P. K. Hurley, T. Hallam and G. S. Duesberg

2. "Controlling defect and dopant concentrations in graphene by remote plasma treatment", *physica status solidi (b)*, 2017, **254**, 1700214
   J. B. Mc Manus, A. Hennessy, C. P. Cullen, T. Hallam, N. Mc Evoy and G. S. Duesberg

3. "A New 2H-2H'/1T Cophase in Polycrystalline MoS_2 and $MoSe_2$ Thin Films", *ACS Applied Materials & Interfaces*, 2016, **8**, 31442-31449
   M. Naz, T. Hallam, N. C. Berner, N. McEvoy, R. Gatensby, **J. B. Mc Manus**, Z. Akhter and G. S. Duesberg

4. "$PtSe_2$ grown directly on polymer foil for use as a robust piezoresistive sensor", arXiv preprint, arXiv:1903.11894
   C. S. Boland, C. Ó ' Coileáin, S. Wagner, **J. B. Mc Manus**, C. P. Cullen, M. C. Lemme, G. S. Duesberg and N. McEvoy

5. "Wafer-Scale Fabrication of Recessed-Channel $PtSe_2$ MOSFETs With Low Contact Resistance and Improved Gate Control", *IEEE Transactions on Electron Devices*, 2018, **65**, 4102-4108
   L. Li, K. Xiong, R. J. Marstell, A. Madjar, N. C. Strandwitz, J. C. M. Hwang, N. McEvoy, **J. B. Mc Manus**, G. S. Duesberg, A. Goritz, M. Wietstruck and M. Kaynak

6. "Defect sizing, separation and substrate effects in ion-irradiated monolayer two-dimensional materials", *Physical Review B*, 2018, **98**

P. Maguire, D. S. Fox, Y. Zhou, Q. Wang, M. O' Brien, J. Jadwiszczak, C. P. Cullen, **J. B. Mc Manus**, S. Bateman, N. McEvoy, G. S. Duesberg and H. Zhang

7. "Nonradiative Energy Transfer and Photocurrent Enhancements in Hybrid Quantum Dot-MoS_2 Devices", 2018 20th International Conference on Transparent Optical Networks (ICTON), 2018
   J. J. Gough, N. McEvoy, M. O'Brien, A. P. Bell, **J. B. Mc Manus**, D. McCloskey, J. B. Boland, J. N. Coleman, G. S. Duesberg and A. L. Bradley

8. "Suppression of the shear Raman mode in defective bilayer MoS_2", *Journal of Applied Physics*, 2019, **125**, 064305
   P. Maguire, C. Downing, J. Jadwiszczak, M. O'Brien, D. Keane, **J. B. Mc Manus**, G. S. Duesberg, V. Nicolosi, N. McEvoy and H. Zhang

9. "Dependence of Photocurrent Enhancements in Hybrid Quantum Dot-MoS_2 Devices on Quantum Dot Emission Wavelength", *ACS Photonics*, 2019
   J. J. Gough, N. McEvoy, M. O'Brien, **J. B. Mc Manus**, J. Garcia-Coindreau, A. P. Bell, D. McCloskey, C. Hrelescu, G. S. Duesberg and A. L. Bradley,

List of presentations

1. "Growth and Characterisation of $MoTe_2$", NanoApp Workshop 2018, Universiät der Bundeswehr, Munich, 19-21 September 2018 (oral)

2. "Controlling defect and dopant concentrations in graphene by plasma treatments", Munich Nanodays Workshop, Universiät der Bundeswehr, Munich, 13-15 September 2017 (poster)

3. "Two-dimensional Heterostructures for Tranisition Metal Dichalcogenides", 69th Irish Universities Chemistry Research Colloquium, Dublin City University, Dublin, 22-23 June 2017 (poster)

4. "Two-dimensional heterostructures from transition metal dichalcogenides", Third Year Talk, University College Dublin, 30th May 2017 (oral)

5. "P-n junction diodes from organic-inorganic semiconductor heterojunctions", International Winterschool on Electronic Properties of Novel Materials, Kirchberg, Tirol, 4-11 March 2017 (poster)

6. “Transition Metal Dichalcogenide Heterostack p-n Junction Diodes Flatlands beyond Graphene”, Bled, 5-8 July 2016 (poster)

Contents

Summary iii

Acknowledgements v

Publications and Presentations vii

Contents ix

List of Figures xvi

List of Tables xvii

List of Acronyms xix

Introduction 1

0.1 Thesis Scope 2

1 Theory and Background 5

1.1 Transition Metal Dichalcogenides 5

1.1.1 TMD applications 8

1.1.2 Telluride TMDs 10

1.1.3 Applications of telluride TMDs 12

1.2 Synthesis of layered materials 14

1.2.1 Exfoliation from bulk 14

1.2.2 CVD methods 15

1.2.3 TMD thin film growth 17

1.2.4 Telluride TMD growth 20

1.2.5 TAC with electrodeposited Te 21

1.3 Electrochemistry 22

1.3.1 Electrochemical measurements 24

1.3.2 Electrocatalysis 28
1.4 Characterisation 31
1.4.1 Raman Spectroscopy 31
1.4.2 X-ray Photoelectron Spectroscopy 34
1.4.3 X-ray Diffraction 36
1.4.4 Scanning Electron Microscopy 37
1.4.5 Transmission Electron Microscopy 39
1.4.6 Atomic Force Microscopy 40
1.5 Electrical Characterisation 41
1.5.1 Heterojunctions 41

2 Experimental **45**
2.1 General materials 45
2.2 Film synthesis 46
2.2.1 Metal deposition 46
2.2.2 Tellurium electrodeposition 46
2.2.3 Film conversion: Sulfides and Selenides 48
2.2.4 Film Conversion: Tellurides 49
2.2.5 Pyrolytic Carbon Layer 50
2.3 Characterisation 50
2.3.1 Raman Spectroscopy 50
2.3.2 X-ray Photoelectron Spectroscopy 51
2.3.3 X-ray Diffraction 52
2.3.4 Atomic Force Microscopy 52
2.3.5 Line profilometry 52
2.3.6 Scanning Electron Microscopy 52
2.3.7 Transmission Electron Microscopy 53
2.3.8 Electrical measurements 53
2.3.9 Electrochemical characterisation 54
2.4 Acknowledgement of contributions 55

3 Sulfide and Selenide TMDs **57**
3.1 Introduction 57
3.2 Growth of TMD films 59
3.2.1 TMD film characterisation 60
3.2.2 Film morphology 62
3.2.3 Electrical characterisation of films 64
3.3 TMD film heterostructures 66

3.3.1 Raman of heterostructures . . . 69
3.3.2 Heterostructure analysis . . . 72
3.4 Conclusions . . . 73

4 Molybdenum Ditelluride 75
4.1 Introduction . . . 75
4.2 Growth of $MoTe_2$ films . . . 76
4.3 Raman spectroscopy of films . . . 80
4.4 XPS & XRD of $MoTe_2$ films . . . 81
4.5 Growth temperature investigation . . . 82
4.6 Stability of films . . . 85
4.7 Film morphology . . . 88
4.7.1 SEM & AFM . . . 88
4.7.2 Cross-sectional TEM analysis . . . 90
4.7.3 Growth mechanism . . . 91
4.8 Application as an electrocatalyst . . . 91
4.9 Conclusion . . . 96

5 Tungsten Ditelluride 99
5.1 Introduction . . . 99
5.2 Growth of WTe_2 films . . . 100
5.3 Raman spectroscopy of films . . . 101
5.4 XRD of WTe_2 . . . 103
5.5 XPS of WTe_2 . . . 103
5.6 Morphology of films . . . 108
5.7 Growth temperature investigation . . . 109
5.7.1 Growth mechanism . . . 110
5.8 Morphology variation . . . 112
5.8.1 Morphology mechanism . . . 114
5.9 Application as electrocatalyst . . . 115
5.10 Transferred flakes of WTe_2 . . . 117
5.10.1 Transfer process . . . 117
5.10.2 AFM of flakes . . . 117
5.10.3 Raman analysis . . . 118
5.10.4 TEM/STEM of WTe_2 crystals . . . 120
5.10.5 Electrical characterisation . . . 123
5.11 Conclusions . . . 125

6 Platinum Ditelluride **129**
6.1 Introduction . . . 129
6.2 Growth of $PtTe_2$ films . . . 130
6.3 Raman spectroscopy of $PtTe_2$ . . . 131
6.4 XPS analysis of films . . . 133
6.5 XRD of films . . . 135
6.6 Growth mechanism and optimisation . . . 135
6.7 Morphology of $PtTe_2$ films . . . 138
6.8 Application as an electrocatalyst . . . 144
6.8.1 Hydrogen Evolution Reaction . . . 145
6.8.2 Oxygen Reduction Reaction . . . 147
6.9 Conclusion . . . 150

7 Conclusions & Future Work **153**
7.1 Future work . . . 156

Bibliography **178**

List of Figures

1.1 TMD bonding configurations and phases 7
1.2 MoS_2 ligand field splitting 8
1.3 W chains in WTe_2 12
1.4 Exfoliation techniques for layered materials 15
1.5 TAC growth process 18
1.6 Mo-S binary phase diagram 19
1.7 Electrode and electrolyte energy levels in electrochemical cell . . . 24
1.8 Three-electrode electrochemical cell 25
1.9 Typical plots of CV and LSV 27
1.10 Energy states and typical spectrum for Raman spectroscopy . . . 32
1.11 Diagram of SEM and interaction volumes of signals 38
1.12 Diagram of AFM 41
1.13 Bandstructure of p-n junction diode 43

2.1 Electrochemical deposition of Te 47
2.2 Diagrams of furnaces for sulfide and telluride TMDs, ... 49

3.1 Raman spectra od TMD films 61
3.2 XPS spectra of TMDs 62
3.3 Line profilometry thicknesses of MoS_2 and WS_2 63
3.4 SEM images of MoS_2, WS_2 and $MoSe_2$ 64
3.5 Electrical results of sulfide and selenide TMDs 66
3.6 Electrical and SEM results of TMD heterostructures 68
3.7 Raman analysis of TMD heterostructures 70

4.1 Electrodeposition and furnace for $MoTe_2$ growth 78
4.2 Raman of $MoTe_2$ films 80
4.3 XPS and XRD of $MoTe_2$ films 82
4.4 Phase diagram and $MoTe_2$ growth conditions 84

4.5 Stability analysis of $MoTe_2$ . . . 86
4.6 SEM of $MoTe_2$ . . . 88
4.7 SEM and AFM analysis of morphology change with thickness . . . 89
4.8 Cross-sectional TEM of $MoTe_2$ . . . 90
4.9 Growth mechanism of telluride TMD films . . . 92
4.10 HER results for $MoTe_2$ . . . 93
4.11 Variation in electrocatalytic properties with roughness . . . 96

5.1 CVs of Te deposition on W . . . 101
5.2 Raman of WTe_2 . . . 102
5.3 XRD of WTe_2 . . . 104
5.4 Depth profile XPS of WTe_2 . . . 105
5.5 SEM images of WTe_2 . . . 109
5.6 Raman spectra of films grown at different temperatures . . . 110
5.7 W-Te binary phase diagram . . . 111
5.8 Morphology change with reactant quantity . . . 113
5.9 WTe_2 HER results . . . 116
5.10 Schematic of transfer process . . . 118
5.11 Tranferred WTe_2 flakes . . . 118
5.12 Raman of WTe_2 flakes . . . 119
5.13 TEM of WTe_2 . . . 121
5.14 WTe_2 electrical results . . . 124

6.1 Raman spectrum of $PtTe_2$ film . . . 132
6.2 Raman spectra of $PtTe_2$ flakes of various thicknesses . . . 133
6.3 XPS and XRD measurements of $PtTe_2$ films . . . 134
6.4 Raman of films grown at different temperatures . . . 136
6.5 Pt-Te binary phase diagram . . . 137
6.6 SEM and AFM of $PtTe_2$ films . . . 139
6.7 Raman map of $PtTe_2$ film . . . 140
6.8 Electrodeposition of Te on Pt . . . 141
6.9 Surface coverage variation with reactant quantity . . . 143
6.10 HER of $PtTe_2$ . . . 146
6.11 ORR of $PtTe_2$ . . . 148
6.12 XPS of film after ORR . . . 149

List of Tables

3.1 Growth conditions for TMD film by TAC 60
3.2 Thickness and roughness of Mo/MoS_2 64

4.1 Literature $MoTe_2$ HER activity results 94

5.1 WTe_2 XPS data 107
5.2 Morphology data for WTe_2 films 113

6.1 $PtTe_2$ XPS data 135
6.2 Morphology data for $PtTe_2$ films 144

List of Acronyms

AFM Atomic force microscopy

BE binding energy

BSE Backscattered electrons

CB conduction band

CV Cyclic voltammetry

CVD chemical vapour deposition

CVT chemical vapour transport

EBL electron-beam lithography

EDX energy-dispersive X-ray spectroscopy

EIS electrochemical impedance spectroscopy

FET field-effect transistor

FFT fast Fourier transform

FIB focussed ion beam

FWHM full width at half maximum

HAADF high-angle annular dark field

HER hydrogen evolution reaction

HOMO highest occupied molecular orbital

HRTEM high-resolution transmission electron microscopy

IDE interdigitated electrodes

LPE liquid-phase exfoliation

LSV linear sweep voltammetry

LUMO lowest unoccupied molecular orbital

MIGS metal-induced gap states

MOCVD metal-organic chemical vapour deposition

OER oxygen evolution reaction

OP overpotential

ORR oxygen reduction reaction

PVD physical vapour deposition

PyC Pyrolytic carbon

QCM quartz crystal microbalance

RHE reference hydrogen electrode

SE Secondary electrons

SEM scanning electron microscopy

SiO_2/Si 300 nm silicon oxide on silicon

STEM scanning transmission electron microscopy

TAC thermally-assisted conversion

TEM transmission electron microscopy

TFET tunnelling field-effect transistor

TMD transition metal dichalcogenide

VB valence band

XPS X-ray photoelectron spectroscopy

XRD X-ray diffraction

Introduction

The allure of controlling materials at an unimaginably small scale has undoubtedly existed since the first description of an atom, if not before. It has only been in the last 50 years that, thanks to a range of technological developments, said dream has become a reality.

The first recorded usage of the term nano-technology is by Norio Taniguchi in 1974, though the term was independently coined in 1981 by Eric Drexler.[1,2] Drexler also served to popularise, and imbibe the term with its current meaning in his 1986 book *Engines of Creation: the coming era of nanotechnology*.

Nanomaterials have been unknowingly exploited for millennia, from the use of nanoparticles to colour glass, and in certain pigments.[3,4] While these nanomaterials conferred desirable properties, their development was haphazard. True mastery and understanding of a field for humans almost invariably involves visualisation, thus the invention of scanning probe microscopy (SPM) techniques at IBM in the 1980s was a huge leap forward.[5,6] Although techniques such as transmission electron microscopy (TEM) had previously imaged atomic scale carbon, SPM techniques offered a clear, intuitive pictures of surfaces in atomic resolution for the first time.[7] This ability to directly image nanoscale features was one of the driving forces of the nanotechnology revolution.

Another powerful factor in the nanotechnology revolution was the semiconductor manufacturing industry. This industry not alone encouraged the development and improvement of a multitude of relevant fabrication and characterisation

techniques, it also served as a challenge to the field. Attempting to surpass benchmarks set by silicon (and previous generations of Si, since nanotech includes improvements in Si) has been a constant spur for the field of nanotechnology. Along with this, the ever increasing power, and ubiquity, of computing has enabled ever larger scale simulations of materials to aid understanding of results.

A combination of these, along with other advances in synthesis and characterisation, enabled the isolation of fullerenes in 1985.[8] This was soon followed by the characterisation of carbon nanotubes in 1991.[9] These discoveries highlighted the exotic properties conferred through quantum confinement of electrons in materials.[10] However, it was the superlative laden mechanical and electronic properties demonstrated by graphene, that led to the wild excitement, and explosion of research effort into the characterisation of an abundance of new nanomaterials.[11]

This has given rise to the current paradigm where thousands of papers are published every year on graphene, along with countless more on other 2D materials. Of these, one of the most widely studied classes have been transition metal dichalcogenides (TMDs).[12] TMDs have demonstrated potential applicability to a wide variety of industries, and range from semiconductors to metals to superconductors.[13] This has led to copious amounts of research into methods to fabricate, modify and combine these materials into products and devices.

0.1 Thesis Scope

This thesis will present the fabrication and characterisation of a number TMDs. For the telluride TMDs, this will be achieved through the modification of the thermally-assisted conversion (TAC) growth method for TMD films. A number of electrical and electrochemical applications of the fabricated TMDs will be subsequently examined. In Chapter 1 an overview of TMDs, with a focus on those containing tellurium, will be given. Discussion of their properties, and potential applications that motivate their study, will also be provided. This chapter will,

in addition, outline the theory of the fabrication and characterisation methods used to study these materials in this thesis. The details of the specific tools used for the fabrication and characterisation will be provided in Chapter 2.

The experimental results of this thesis are divided among four chapters. Chapter 3 will outline the low-pressure TAC growth method for sulfide and selenide TMD films. The characterisation of these films will highlight some of the strengths and weaknesses of this growth method and the films it produces. The three remaining Chapters discuss the growth of the telluride TMDs: molybdenum ditelluride ($MoTe_2$), tungsten ditelluride (WTe_2) and platinum ditelluride ($PtTe_2$). While the majority of the description of the modified TAC method is provided in Chapter 4, in relation to $MoTe_2$, further insights into the characteristics and mechanism behind it are provided in relation to WTe_2 and $PtTe_2$ in Chapters 5 and 6 respectively. The characterisation of the films will reveal polycrystalline films, which differ significantly from those grown by TAC, along with giving insights into the mechanism of the growth. Suitability of each telluride TMD as an electrocatalyst will be examined for hydrogen evolution reaction (HER) and oxygen reduction reaction (ORR), while the electrical response of WTe_2 flakes will also investigated.

Finally Chapter 7 will give a summary of all results obtained, along with offering guidance as to potential future work, on this method and these materials.

1

Theory and Background

This chapter will introduce the various layered materials studied throughout this thesis, their properties, the motivation behind studying them and their potential applications. The typical fabrication and characterisation methods used to study these materials will be discussed, with a particular focus on the techniques used in this work.

1.1 Transition Metal Dichalcogenides

Layered materials have become some of the most studied materials in nanoscience. This interest has stemmed from their anisotropic bonding scheme that enables the growth and extraction of atomically-thin sheets.

Aside from graphene, one of the most prominently studied groups of layered materials has been TMDs. TMDs are layered materials consisting of a transition metal, M, and a chalcogen, X, in the general formula MX_2. A single TMD layer, referred to as a monolayer, has a layer of metal atoms surrounded on both sides by a layer of chalcogens atoms. Within each monolayer atoms are covalently bonded. The monolayers are then stacked vertically to form bulk crystals, with only much weaker van der Waals bonds between the layers. This is the defining

feature that has allowed very thin, large-area nanoscale sheets of TMDs to be fabricated, isolated and studied.

The first TMD that was extensively studied on the nanoscale was MoS_2, an earth-abundant compound that is widely used as a solid lubricant due to is layered structure and also in hydrodesulfurization during petroleum refining.[14,15] Subsequently, a host of different TMDs, especially those with Group VI transition metals, have been examined. These include WS_2, WSe_2, $MoSe_2$, $MoTe_2$, WTe_2, PtS_2, $PtSe_2$, $PdSe_2$, many of which have shown unique and interesting properties.[16,17]

In TMDs, each metal atom, M, is bonded to 6 chalcogen atoms in a trigonal prismatic, octahedral or distorted octahedral configuration as shown in Figure 1.1. These then form monolayers with structures referred to as 2H, 1T and 1T' respectively.[18] When the monolayers are stacked together another degree of freedom is introduced. 2H monolayers can be stacked to give the 2H or 3R structures. While more complicated 2H stacking arrangements are possible, they usually have very little bearing on the material properties and will not be discussed further within the scope of this thesis. 1T monolayers only have a single stacking configuration, in contrast to those with the 1T' structure, which can be stacked in two different manners to give either the 1T' (e.g. $MoTe_2$) or the T_d (e.g. WTe_2) structures. The stacking arrangements and unit cells of each of these structures are shown in Figure 1.1.

Group VI TMDs tend to be most stable in the 2H phase (WTe_2 is an exception to this), whereas those with a Group X transition metal centre are more stable in the 1T octahedral configuration.[19] The phase has a large influence on the electronic character of a TMD, with the majority of those in the 2H phase being semiconducting, while many in the 1T phase are metallic or semimetallic. This primarily holds for the Group VI TMDs and can be understood by examining the orbital splitting of the compounds.

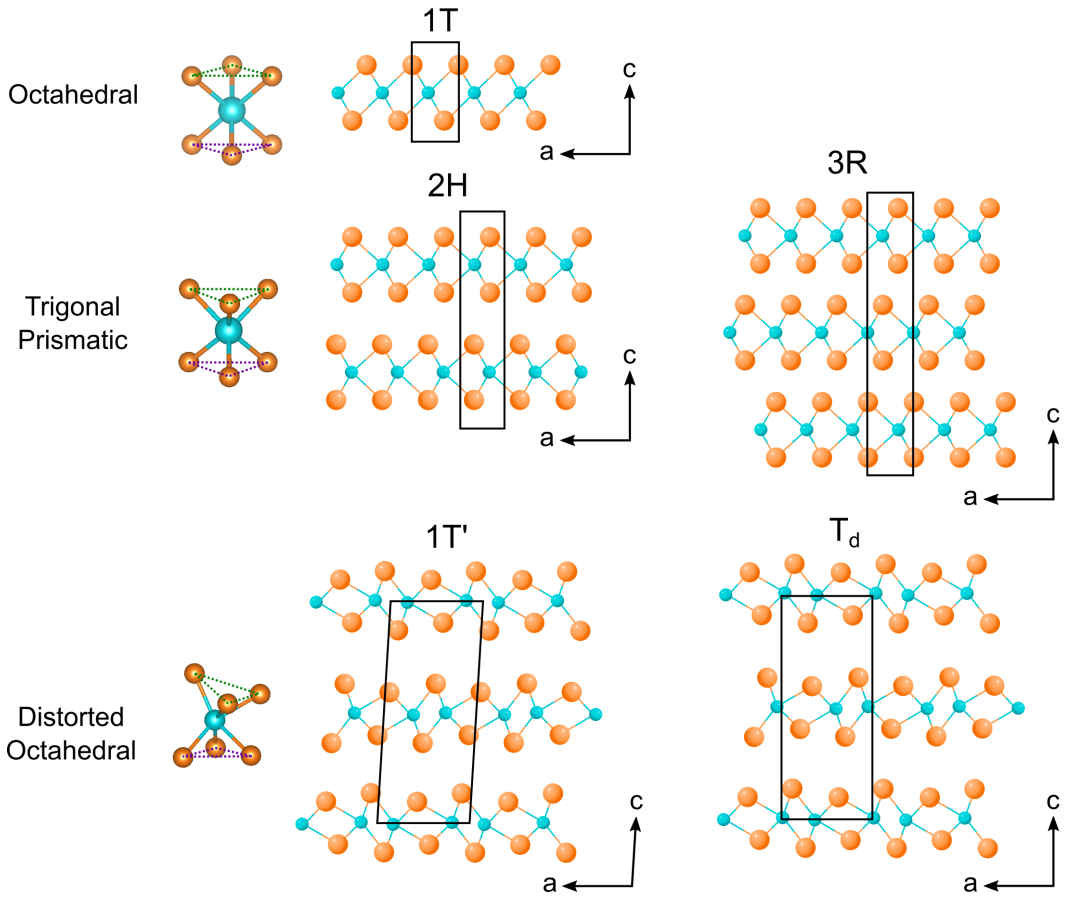


Figure 1.1: Schematic of the three possible bonding configurations of TMDs; octahedral, trigonal prismatic and distorted octahedral, along with their associated stacking configurations and unit cells. The crystallographic directions of each are also indicated.

In the octahedral structure, the d-orbitals of the transition-metal centre are split into the triply degenerate $d_{xy,yz,zx}(t_{2g})$ set and the doubly degenerate $d_{x^2-y^2,z^2}$ (e_g) set. In contrast, the 2H trigonal prismatic structure results in two doubly degenerate sets, the $d_{xz,yz}$ and the $d_{x^2-y^2,xy}$, and the most stable d_{z^2} orbital.[20,21] Examining this for MoS_2 results in both valence electrons occupying the d_{z^2} orbital for the 2H structure and the electrons singly occupying two of the triply degenerate t_{2g} orbitals for the 1T structure as shown in Figure 1.2. The stability of MoS_2 in the 2H phase is due to the combined energy of these electrons being lower in this structure. The semiconducting nature of 2H MoS_2 is due to the filled orbital.[22] Conversely, the 1T phase is metallic due to its partially filled orbitals. This analysis also demonstrates why other TMDs with differing numbers

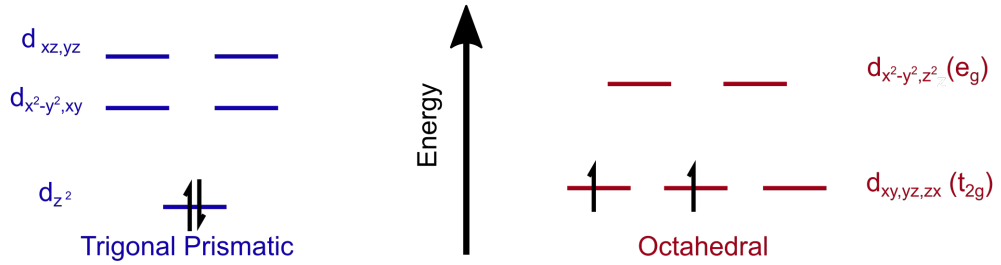


Figure 1.2: Schematic of the ligand field splitting in MoS_2 for 2H and 1T crystal structures.

of valence electrons, such as those from Group X, may be more stable in the 1T phase.

As one moves down the periodic table in both the transition metal (Mo to W) and chalcogen (S to Se to Te) component, the electronegativity between the elements reduces and the bonding orbitals become more delocalised and covalent in character. This results in increased fabrication and stability challenges for the TMDs. It also explains why WTe_2 is more stable in the T_d phase. This phase is less favourable when examining the crystal field splitting, however this is offset by the increased stabilisation due to the charge density wave stabilisation stemming from the distorted octahedral structure. This is static modulation of conduction electrons to reduce energy and is accompanied by periodic distortion of the lattice[19] It is also the balance between these two stabilisation mechanisms that results in the 1T' and 2H phases of $MoTe_2$ being so similar in energy.[23,24]

1.1.1 TMD applications

As with other layered materials, studying TMDs on the nanoscale is of interest due to their anisotropic electronic and mechanical properties, bond-free interfaces, layer dependant properties and exceptionally large surface-area-to-volume ratios. Along with this, 2D TMDs have also demonstrated exceptionally varied material properties and potential applications, depending on the constituent metal and chalcogen.[25–30]

A number of TMDs are semiconductors, with bandgaps similar to that of silicon that can be tuned by changing their thickness (layer number), making them strong candidates for applications in nanoelectronics. A huge advantage that TMDs bring to nanoelectronics is their ultimate thinness, which allows superior gate control of the channel. This property can be leveraged to reduce the power consumption of current integrated circuits and potentially in architectures such as tunnelling field-effect transistors (TFETs).[31] TMDs are also very attractive for use in flexible electronics due to their stability. A number of works have demonstrated high performance MoS_2 field-effect transistors (FETs) on flexible substrates.[30,32]

TMDs have also shown promise in the field of optoelectronics. Due to their tunable bandgap, strong light matter interaction and viability for use in atomic heterostructures, they have been implemented in photodetectors with low dark currents, high responsivity and fast switching speeds over a wide spectral range.[33–35] As many TMDs are direct bandgap semiconductors in their monolayer form, with high photoluminescence efficiency, they are well suited for use in LEDs. TMDs have been examined for this application in a variety of p-n junction, Schottky junction and tunnelling junction configurations with promising results.[36–38]

Modifying TMDs, through chemical functionalisation, doping or plasma treatments, further broadens their range of potential applications. These treatments have been investigated in the context of (opto-)electronic devices and, while interesting in this regard, any modification to the TMD device can have a large impact on the electrical properties of the device. Chemical functionalisation is especially relevant for applications such as sensing and catalysis. 2D materials are particularly suited to these due to their exceptionally large surface-area-to-volume ratio. TMDs have been successfully implemented as sensors for a multitude biomolecules such as DNA, adenine and glucose.[39] As gas sensors, TMDs have been shown to be competitive with the state of the art for certain analytes.[40]

These materials have also shown promising catalytic behaviour for water splitting and CO_2 photoreduction.[41,42] It has been found that increasing the density of under-coordinated edge sites or defects, can increase the catalytic activity of TMDs.[43,44] Additionally, converting the material to the 1T phase, which is more conductive, can also enhance the behaviour due to improved charge transfer to active sites and increased basal plane activity.[45,46]

Finally, individual members of the TMD family have also been investigated for more specific properties such as for superconductors, 2D magnets and application in spintronics and valleytronics.[47–50] They are also interesting as systems in which to study novel physical phenomena such as topological insulators, Weyl semimetals and type-II Dirac semimetals.[51,52]

It is for these reasons that TMDs are such a huge area of interest and have been heralded with such enthusiasm for a wide range of potential applications, making synthesis of TMDs in various forms a worthwhile investigation.

1.1.2 Telluride TMDs

While adhering to many of the trends seen with other TMDs, tellurium containing TMDs do differ in a number of interesting ways. The properties of these will be discussed here, with a focus on $MoTe_2$, WTe_2 and $PtTe_2$.

Three structural phases of $MoTe_2$ have been studied: the 2H, trigonal prismatic phase; the 1T' distorted-octahedral or monoclinic phase and finally the T_d orthorhombic phase. The 1T phase of $MoTe_2$ is unstable, however there are reports of it being stabilised by extrinsic effects, such as adsorbates, in the monolayer form.[53] The semiconducting, 2H phase of $MoTe_2$ is the most thermodynamically stable, similar to MoS_2 and $MoSe_2$. However, in the case of $MoTe_2$, the ground state energy difference between the semiconducting 2H and the semimetallic 1T' phase is much smaller - only 35 meV per formula unit.[23,24] This means that at ambient conditions both phases can be stable. The T_d is a

metallic phase that has been shown to be stable at low temperatures and with dopants, such as W, present.[54,55]

Unlike $MoTe_2$, WTe_2 only exists in one phase at room temperature - the semimetallic T_d phase, and it is the only Group VI TMD that is not most thermodyncamically stable in the 2H phase.[56,57] The space group of bulk WTe_2 is $Pnm2_1$ or the point group $C_{2v}{}^7$. In monolayer, WTe_2 has a distorted octahedral structure, isostructural with $MoTe_2$, as the only difference between the 1T' and T_d phases is how the monolayers are stacked, as shown in Figure 1.1. It has been observed that at high pressure, 4 - 5 GPa, WTe_2 undergoes a phase transition to the 1T' phase, with further theoretical predictions that the 2H phase would be stable at $\sim$10 GPa.[56]

Despite WTe_2 being considered a layered, or 2D material, it has some 1D character due to its distorted octahedral structure. This distortion causes quasi-1D chains of W atoms to be formed within the layers, shown in Figure 1.3. In these 1D chains W-W bond lengths are close to that of tungsten metal.[56] This leads to a strong anisotropy of properties, such as conductivity and mechanical responses, within a monolayer of WTe_2.[58] The effect of this anisotropy is also seen in the growth of WTe_2 crystals as they tend to grow with one dimension significantly longer than the others.[59]

$PtTe_2$ has a 1T structure similar to that of other Group X dichalcogenides such as $PtSe_2$. It is a semimetallic TMD that to-date has not been extensively studied.[60] A notable property of $PtTe_2$ is that the interlayer bonding is significantly stronger than in many Group VI TMDs such as MoS_2. This makes the fabrication of monolayers of $PtTe_2$, through chemical vapour deposition (CVD) or exfoliation, challenging.[21,61] It also means that making atomically-thin flakes, with appreciable lateral dimensions, using liquid-phase exfoliation (LPE) would be extremely difficult.

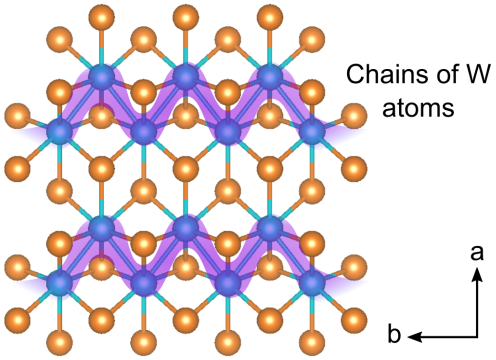


Figure 1.3: Diagram of T_d phase WTe_2 showing the 1D W chains along the b crystallographic direction.

1.1.3 Applications of telluride TMDs

As the majority of telluride TMDs are semimetals they have not been investigated heavily for logic electronic applications. An exception to this is the 2H phase of $MoTe_2$. $MoTe_2$ has two stable phases under ambient conditions. While presenting a fabrication challenge, this property also offers a number of opportunities with regards to electronic applications, if phase selective growth can be mastered. By creating 1T':2H junctions in $MoTe_2$, it could be possible to create 2D-to-2D edge contacts on semiconducting 2H $MoTe_2$ devices.[62] These ultra-low contact resistance devices would be interesting as it gives a chance to address the issue of contact resistance in semiconducting 2D devices. 2H $MoTe_2$ is also a promising candidate for use in optoelectronics including visible and short-wave IR photodetection.[63–65] T_d WTe_2 has been examined as a potential interconnect material in nanoelectronics due to its ability to withstand current densities of up to 100 MA cm^2.[66]

Recent explorations into the mono- and few-layer forms of telluride TMDs have resulted in a large amount of interest in using these materials as a platform to explore exotic physical phenomena. WTe_2, $PtTe_2$ and 1T' $MoTe_2$ have all been examined as type-II Weyl or Dirac semimetals.[67–70] 1T' $MoTe_2$ and WTe_2 have also shown pressure-sensitive superconductivity, and monolayer WTe_2 is a promising candidate for large-gap quantum spin Hall insulators.[55,71,72] Further-

more, WTe_2 has been found to have extremely-large positive magnetoresistance at low temperature, due to its balanced electron-hole population.[73,74] 1T' $MoTe_2$ has also shown similar results.[75]

Due to their relatively high electrical conductivity and Seebeck coefficient, along with their low thermal conductivity, TMDs have attracted attention for their potential as high-performance thermoelectric materials. Interest in the thermoelectric properties of WTe_2 are well established - the ability to grow stable, mixed-phase films of semiconducting 2H and the strongly anisotropic, semimetallic 1T' $MoTe_2$ is an especially interesting prospect in this regard.[76,77]

Nanomaterials have an exceptionally high surface-area-to-bulk-ratio, this serves to enhance intrinsic catalytic properties of the materials. Layered TMDs have been shown to be viable candidates for electrocatalytic applications, especially when in a (semi-)metallic phase, due to their much higher conductivity. All three of the TMDs being examined here, $MoTe_2$, WTe_2 and $PtTe_2$, have been investigated for catalytic applications. $PtTe_2$ has been shown to be an excellent catalyst for the oxygen evolution reaction (OER) and the ORR, and demonstrated improved catalytic behaviour post surface modification.[78,79] Investigations of $MoTe_2$ for catalytic applications have found the 1T' phase to be much more active than the semiconducting 2H phase.[80,81] There have also been some electrochemical investigations of using WTe_2 as a catalyst for the HER. Li *et al.* examined the catalytic behaviour of WTe_2 nanoribbons and found them to be much superior to WS_2 and WSe_2 in a similar form.[82] Gholamvand *et al.* measured a lower response for LPE flakes of WTe_2 and found WTe_2 to be among the worst performing of the Group VI TMDs, despite being semimetallic.[80] The suggested cause of this is the relatively large positive Gibbs free energy of adsorption of H atoms on WTe_2.[83]

There have been numerous investigations of telluride TMDs for various other applications such as possible phase-change materials for energy storage or sensors and as an anode material in sodium ion batteries.[84,85] Due to these many and

varied potential applications, developing reliable fabrication methods for telluride TMDs is of immediate interest.

1.2 Synthesis of layered materials

The study of 2D materials has been carried out on both material extracted from bulk crystals, top-down methods, and materials fabricated from the constituent elements, bottom-up methods. A brief overview of the most common techniques of each will be given below, with a focus on those most applicable to this work.

1.2.1 Exfoliation from bulk

Extraction of thin crystalline layers from bulk layered crystals has been ongoing for decades, with monolayers of graphite observed by TEM as early as 1962.[86,87] However, it was when graphene was isolated using mechanical exfoliation (Scotch-tape method) in 2004 that the area of nanoscale research into layered materials exploded.[11] The first investigations of 2D materials were conducted almost exclusively on mechanically-exfoliated flakes from natural or chemical vapour transport (CVT) grown crystals. The technique of micro-mechanical cleavage is based on the conceptually simple Scotch-tape method, Figure 1.4(a). It involves repeated exfoliation of a crystal with an adhesive tape to produce mono- or few-layer flakes that can then be deposited on substrates. While simple in theory, there is a great deal of work involved in obtaining reliable, relatively large-area flakes on a consistent basis. For this reason, this method will never be able to produce material on an industrially relevant scale. It does however create very high-quality 2D materials, ideal for fundamental studies along with proof-of-concept devices.[88]

In stark contrast, the other popular exfoliation method, LPE, is perhaps the most scalable method to produce 2D materials. LPE involves applying sonic or shear energy to a suspension of layered material to separate the layers of crystalline powder from each other, Figure 1.4(b).[89,90] If this is performed in an

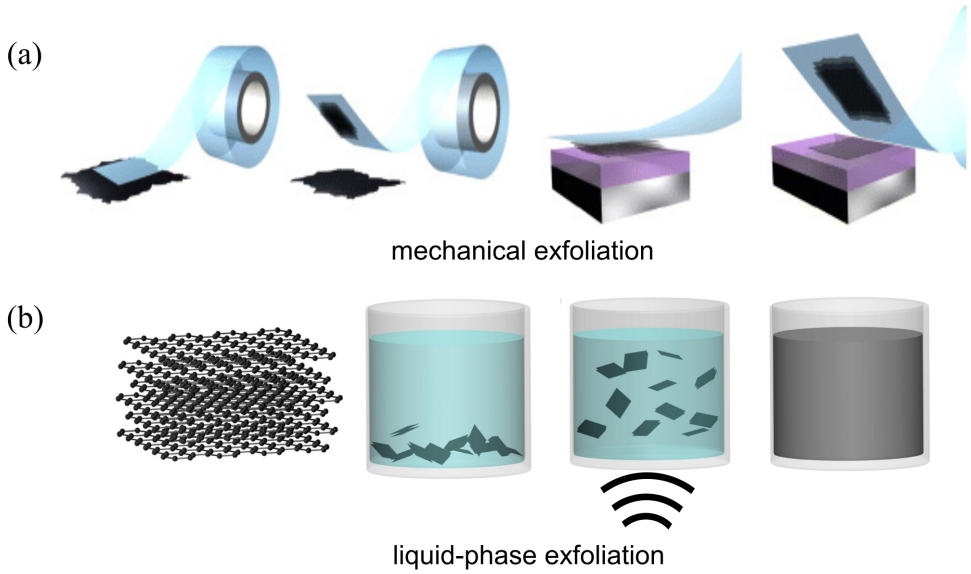


Figure 1.4: (a) Diagram of mechanical exfoliation of layered materials.[93] (b) Diagram of the liquid-phase exfoliation processing method.[94]

appropriate solvent, or surfactant, the flakes are prevented from re-aggregating through the interactions of the solvent (surfactant) molecules with the flakes. Repeated centrifugation allows the separation of flakes on the basis of size. However, achieving solutions with high concentrations of large-area, mono- or few-layer flakes is exceptionally difficult. This is because the energy applied to separate the layers also tends to break flakes into smaller pieces. The flakes can be separated from the solvent through methods such as vacuum filtration or deposited onto substrates by printing from inks.

LPE offers the advantage being one of the most scalable methods of 2D material production and is especially suitable for producing materials for use in reinforcement and low-cost electronics.[91] It is not suitable for high-quality electronics as the films are dominated by the properties of the flake junctions, and due to the flakes tending to have small lateral dimensions with a distribution of flake thicknesses in a given dispersion.[92]

1.2.2 CVD methods

CVD offers the ability to produce high-quality 2D materials with a much higher

throughput than mechanical exfoliation, while still being of comparable quality, and so offers an excellent production method for 2D materials. More generally, CVD is defined as the formation of a solid film on a substrate through the reaction of vapour phase chemicals containing the necessary constituents.[95] CVD is a widely used industrial process that can be used to make high-quality materials and coatings. It is a promising method for the production of 2D materials due to its ability to integrate with traditional silicon processing techniques and fabricate device geometries down to length scales limited only by lithographic patterning.

CVD has been used successfully to produce 2D materials over large areas with good control and reproducibility, as well as high crystalline quality. When applied to TMDs however, it is challenging to produce layer selective and controlled growth on a large scale.[96–98] Nevertheless, there is progress being made on this front, with wafer-scale, homogenous TMD growth being demonstrated for a number of materials, with careful optimisation of growth parameters.[99] Along with this, the use of metal-organic chemical vapour deposition (MOCVD), which relies on gaseous, rather than solid precursors, has enabled progress towards large-area, layer-controlled growth of TMD films.[100,101]

The ability to combine multiple materials together in reproducible ways is a significant step towards integrating 2D materials into industrial processes and devices. CVD can be used to grow *in situ* heterojunctions of TMDs down to the monolayer limit.[102] CVD has allowed the growth of lateral and vertical heterostructures of numerous TMD combinations. These heterostructures offer the opportunity to make devices at the ultimate thickness limit, and have been used to create atomic scale p-n junctions and diodes.[103–105]

Despite the success achieved, precise control over heterostructure geometry and reproducibility remains a challenge. There are a number of other disadvantages of CVD growth, such as potentially toxic precursors or by-products.[106] Many TMDs require quite high growth temperatures (600 - 800 °C), which is

a challenge for integration with current silicon technologies and limits substrate choice.[107] Despite this, CVD is considered the most promising method for the scalable production of large-area mono- or few-layer 2D materials.

1.2.3 TMD thin film growth

Producing metallic films with sub-nanometre thickness control, using sputtering or evaporation is a well-established process. This made such films an excellent starting point from which to produce TMDs with controlled thicknesses and geometries.

The process of converting pre-deposited metal films to corresponding TMDs will be referred to here as thermally-assisted conversion (TAC). The basis of this technique is that a thin film of metal, or metal oxide, is first deposited on a substrate, typically by sputtering or evaporation. This sample is then exposed to chalcogen vapour at an elevated temperature (usually 400 - 900 °C) facilitating conversion to the corresponding TMD, Figure 1.5. Since the reactants are not all in the vapour phase this cannot be considered true CVD, rather it could be described as a CVD-like process or a CVD variant.

Though not new, it was when this method was reported in the context of ultrathin 2D TMDs by Zhan *et al.*[108] that it sparked widespread interest.[108] This work examined converting e-beam evaporated Mo to MoS_2 films. The films showed characteristic MoS_2 Raman and X-ray photoelectron spectroscopy (XPS) signals, while electrically they had a low gate response and charge-carrier mobilities on the order of 0.01 $cm^2V^{-1}s^{-1}$. This technique has since been used to produce a wide range of TMDs e.g. $MoSe_2$, WSe_2, WS_2, $PtSe_2$, PtS_2, among others.[40,109,110]

While not suitable for producing highly-crystalline monolayer samples, the TAC growth method has a number of advantages. Certain materials that can be very difficult to grow by CVD, such as $PtSe_2$, can be grown quite readily using this

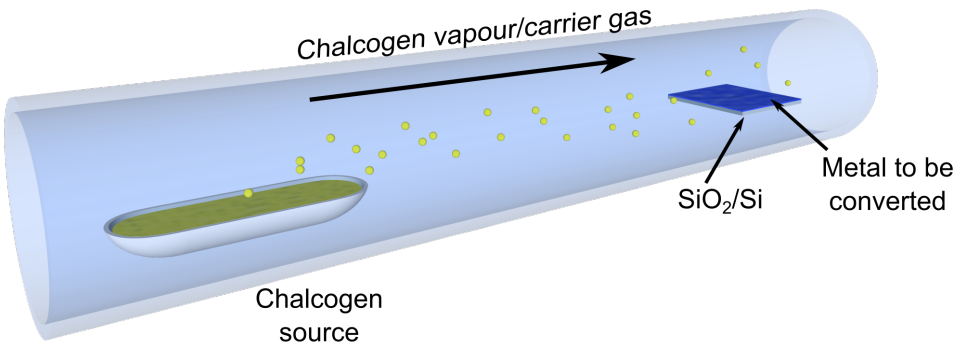


Figure 1.5: Diagram of the quartz tube furnace for the TAC growth process.

method.[40] TAC is an inherently scalable process and gives uniformity over a large area. It also allows simple patterning of samples to produce devices, achieved by patterning the initial metal layer using shadow masking or lithography. This is all possible on a wide variety of substrates.

Film thickness is controlled through variation of the initial metal layer thickness, meaning that TAC films can be grown that have bulk-like properties all the way down to those which show monolayer qualities, such as photoluminescence.[109] Purely monolayer films are not generally possible with TAC, the thinnest films are non-continuous with mono- and bilayer areas.[111] Due to the incorporation of the chalcogen, the thickness of the TMD films is typically 2 - 3 times that of the initial metal film, though this is not the case for TMDs fabricated from metal oxide precursor films.[112,113]

Somewhat similar to LPE films, TAC films are not well suited to high-quality electronic applications.[112,114] They are polycrystalline (with grains on the order of 10s - 100s of nanometres) and can have high levels of defects, which can cause high and varied levels of unintentional doping in the films. As such, field-effect transistors based on TAC-grown materials often show comparatively low gating response and typical mobilities below 10 $cm^2V^{-1}s^{-1}$.[108,114–116] These same characteristics however, make them exceptionally well-suited to applications such as gas sensing and catalysis.[117,118] TAC-grown TMD films have been used as chemire-

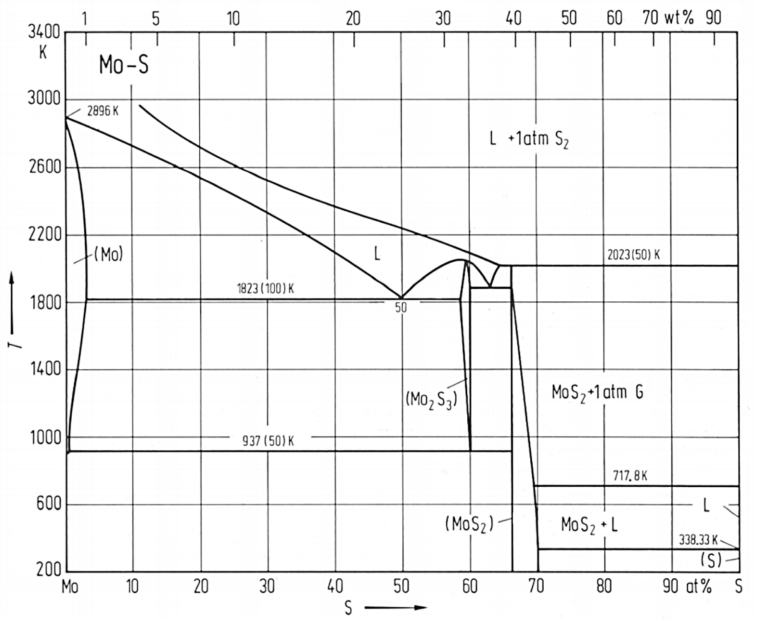


Figure 1.6: Mo-S binary phase diagram, adapted from reference.[121]

sistor sensors,[40,117] with other works having demonstrated the promise of MoS_2 and $MoSe_2$ films as catalysts for the HER.[119]

The mechanism of TAC growth is often described as a direct chemical reaction or alloying between the metal and chalcogen.[120] The TAC growth process will be discussed here in the context of MoS_2, by examining the Mo-S binary phase diagram, reproduced in Figure 1.6.[121] The Mo film is initially heated to growth temperature of 1073 K, before the S vapour is introduced. At this temperature the diffusivity of S into Mo is high and would result in a rapid increase in the S content of the nanoscale films. This would move the films towards the right across the phase diagram. As the S is kept in excess throughout the growth, a full reaction of the Mo film to MoS_2 would be expected, with the remaining S being pumped away in the gaseous phase. The films are exposed to atmosphere prior to conversion, as a result there is likely some level of molybdenum oxide on the surface, the conversion reaction of this oxide to MoS_2 is discussed in the report by Weber *et al.*[122] Finally, if S is not kept in excess quantities throughout the growth phase the films will not completely convert to MoS_2.[123]

1.2.4 Telluride TMD growth

The vast majority of studies on telluride TMDs thus far, have relied on CVT-grown crystals, and mechanically exfoliated flakes thereof, to obtain high-quality samples for study.[55,67,124] The CVT growth of $MoTe_2$, WTe_2 and $PtTe_2$ requires long growth times and high temperatures, on the order of days and 1000 °C respectively.[51] Therefore, the process is energy and time intensive and, as such, less attractive to scaling. The issues with mechanical exfoliation that were discussed in Section 1.2.1 add to this also. This gives a large incentive for exploration of alternative synthesis methods, as, for any potential future applications, a scalable growth method will be needed.

The CVD growth of telluride TMDs is more challenging than for sulfides and selenides due to the lower chemical reactivity between Te and Mo/W/Pt, along with the smaller electronegativity difference between these.[125] Despite this, CVD growth of $MoTe_2$, WTe_2 and $PtTe_2$ has been demonstrated to varying extents. $MoTe_2$ has been grown most extensively using this method, with a number of works demonstrating monolayer growth of both the 1T' and 2H phases.[126–128] The majority of $MoTe_2$ CVD growths were achieved using precursor powders, such as MoO_3, $MoCl_5$, Te and $(NH_4)_6Mo_7O_{24}$, which were vaporised and reacted during the growth. One work achieved wafer-scale, phase-selective growth of few layer $MoTe_2$ using an MOCVD process.[129] Nevertheless, monolayer growth, of either phase, on this scale has yet to be achieved.

CVD growth of WTe_2 has also been shown in a number of works. Similar to $MoTe_2$, growth of monolayer single-crystal WTe_2, from Te, WO_3 and WCl_6 powders, has been demonstrated.[130,131] Other works have achieved larger monolayer films, however these consisted of smaller crystals knitted together.[127] Despite these promising works there remains quite a way to go before reproducible, directed, layer-specific growth of WTe_2 is achieved.

For $PtTe_2$ there have been few reports of CVD growth. Currently there are

only two published reports, both of which grow small area $PtTe_2$ crystals, neither of which achieved monolayer growth.[60,132] This is perhaps due to the stronger interlayer bonding in $PtTe_2$ that would inhibit large-area monolayer formation.[21,61] One of these used $PtCl_4$, Te and NaCl powders as the precursors while the other simply employed elemental Pt and Te powders.

The growth of thin films of $MoTe_2$ through TAC-like processes has also been reported.[126] This has involved the conversion of Mo and molybdenum oxide films to one, or both, $MoTe_2$ phases.[133] Growth temperatures of between 500°C and 800°C, have been used, with some reports demonstrating phase-selective growth by adjusting the temperature and gas flow parameters.[134,135] A similar work on WTe_2 by Kwak *et al.* used predeposited layers of W and Cu exposed to Te vapour to synthesise crystalline WTe_2 nanobelts that could then be removed from the substrate and re-deposited for further examination.[136] This yielded nanobelts of WTe_2 that were highly crystalline but required a post-growth etch to remove Cu from the sample. The same authors also demonstrated this process for $MoTe_2$. Finally Hao *et al.* grew $PtTe_2$ through the reaction of a predeposited Pt layer directly with Te powder at an elevated temperature.[61]

While there is clearly a number of reports examining the growth of telluride TMDs by various methods, this field is far from mature and leaves a pressing need for further work on straight-forward scalable growth processes.

1.2.5 TAC with electrodeposited Te

In this work polycrystalline thin films of telluride TMDs are produced using a variation of the TAC method. In this case, the metal layer is deposited, followed by electrodeposition of tellurium. This stack of metal and tellurium is then annealed in an inert atmosphere to grow the TMD. While being conceptually quite similar to TAC, in this case the growth is at a solid-liquid interface rather than a solid-vapour one. This leads to a much higher chalcogen concentration

and results in the polycrystalline TMD film having much larger grain sizes and also being quite rough.

1.3 Electrochemistry

The following discussion on electrochemistry has been adapted from books by Bard,[137] Saji and Cook[138] and the Southampton Electrochemistry Group.[139]

Electrochemistry is a broad area which is concerned with the study of chemical changes caused by application of an electric current, or conversely, the production of electrical energy from chemical reactions.

In an electrochemical system, where there is a valid half reaction possible at each electrode, an equilibrium will be reached where no net current is flowing, and a fixed potential difference can be measured between the electrodes. This potential difference is dependent on the nature of the elements and condition of the system. The chemical reaction taking place in the electrolyte, at one electrode, can be described by

$$R \leftrightharpoons O + ne^- \tag{1.1}$$

where R and O are the oxidised and reduced form of the species, and ne^- is the number of electrons transferred between the electrode and the species during the reaction. At equilibrium, the potential measured at this electrode is described by the Nernst equation:

$$E = E^0 + \frac{RT}{nF}\ln\frac{c_O^\infty}{c_R^\infty} \tag{1.2}$$

where E^0 is the standard electrode potential - the potential versus the reference hydrogen electrode (RHE) at standard conditions, R is the universal gas constant, T is temperature, F is Faraday's constant, n is the number of electrons involved in the reaction and c_O^∞ and c_R^∞ represent the bulk concentrations of the

oxidant and reductant respectively as shown in Equation 1.1.

When a voltage other than E, is applied to the cell the reaction in Equation 1.1 will be driven in one direction, resulting in electrons being passed across the electrode interface and a current flow being measured. This process can be understood by examining the band/energy level diagrams of the electrode and the molecular species involved, as shown in Figure 1.7. At equilibrium the Fermi level (E_f) of the electrode is, by definition, situated at the same energy as the highest occupied molecular orbital (HOMO) of the molecule, as shown by Figure 1.7(a). If a sufficiently negative voltage is applied to the electrode, the E_f will be raised above the lowest unoccupied molecular orbital (LUMO) of the molecule and electrons will flow from the metal to the molecule, reducing it. Conversely, if a more positive voltage is applied the species will be oxidised. The amount of voltage applied above the equilibrium potential, to drive the reaction, is known as the overpotential (OP). It is defined as:

$$\eta = E_{app} - E \tag{1.3}$$

where η is the OP, E_{app} is the applied potential and E is the equilibrium potential.

When a voltage is applied across a cell, almost all of the potential drop occurs at the interface between the electrode and the electrolyte. This potential difference will cause a flow of charge across the boundary resulting in a charge separation and the formation of an electrical double layer. As the electrochemistry of interest occurs in this region, understanding this interfacial region is of utmost importance. One model of this is the Gouy-Chapman-Stern model, which describes an adsorbed layer of ions at a certain very small distance from the metal surface, and beyond this a diffuse layer of ions of slowly decreasing concentration.[140]

Up to this point the electrode reactions have been discussed in terms of un-

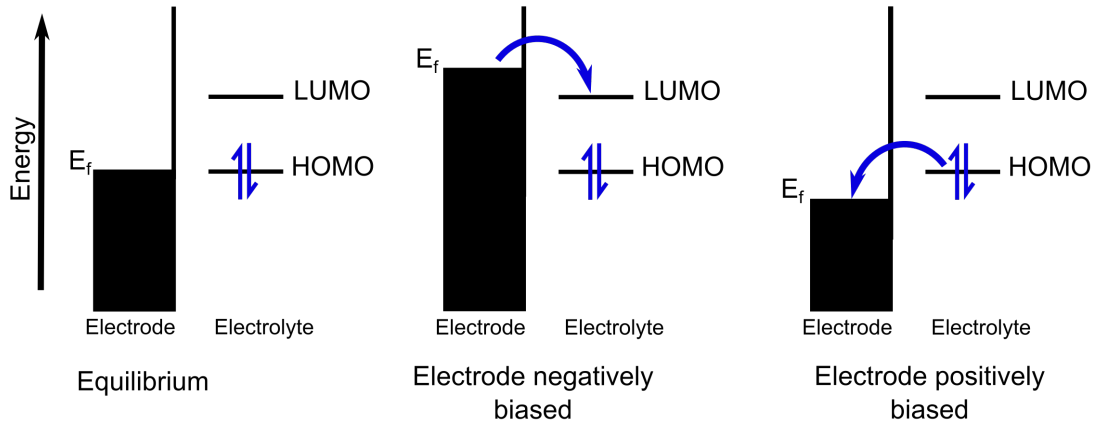


Figure 1.7: Diagram of the relevant energy levels of the electrode and electrolyte at equilibrium and with the electrode positively and negatively biased.

changing bulk concentrations, whereas in reality the concentrations of reactants and products can change significantly in the vicinity of the electrode surface. As a reaction proceeds, reactant concentration will be diminished, as concurrently the concentration of products will increase. This will lead to a concentration gradient within the electrolyte, and diffusion of reactants (products) towards (away from) the electrode. This diffusion can become the limiting factor in the reaction if the reaction kinetics are fast.

1.3.1 Electrochemical measurements

In this work all electrochemical measurements and processes are conducted using a three-electrode cell. The cell consists of the sample acting as the working electrode, a reference electrode that has a standard unchanging potential and a counter electrode that is used to complete the circuit. A diagram of this set-up is shown in Figure 1.8.

Electrodeposition

Electrodeposition is a type of electrocrystallisation where ions in solution are reduced and form a solid layer on the electrode. Electrodeposition is extensively used in industry to produce protective coatings against wear and for cosmetic

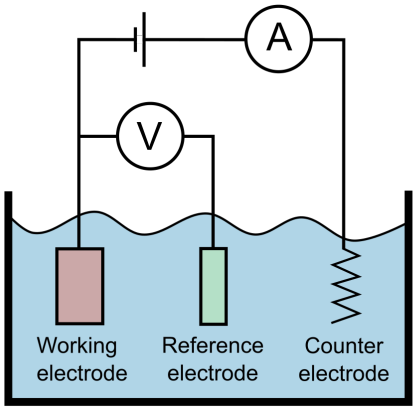


Figure 1.8: Schematic of a three-electrode electrochemical cell, similar to those used throughout this work

reasons. It has also become a versatile technique for the preparation of nanomaterials.

In electrodeposition the cathode (working electrode) is a conducting substrate on which the desired material will be electrodeposited. The species to be reduced (TeO_2 in this work) is in solution. When a negative potential is applied to the cathode, this will drive the reaction and the species in solution will be reduced and deposit onto the electrode. The steps involved in this process are: diffusion of ions to the electrode surface, electron transfer, formation of ad-atoms, formation of critical nuclei, incorporation into the lattice sites and development of crystallographic characteristics. The rate of the reduction will be determined by the slowest among these.

The amount of material deposited on the electrode during a period, t, will be related to the total current as described by Faraday's law. The total amount of charge passed through the cell, Q is given by

$$Q = \int I \partial t = nmF \tag{1.4}$$

$$m = \frac{Q}{nF} = \frac{1}{nF} \int I \partial t \tag{1.5}$$

where I is the current measured, m is the number of moles deposited on the electrode involving n electrons per molecule and F is Faraday's constant. It should be noted that Q is not a parameter that can be directly controlled during an electrodeposition. The applied voltage can be controlled, but not the current itself as it is related to the applied voltage by $I = V/R$. This means that slight variations in the resistance of the system from sample to sample will cause changes in the amount of material deposited for the same conditions.

There are a number of parameters that can be tuned to control the adhesion, morphology and uniformity of the deposited film. These include electrolyte concentration, OP, voltage profile and geometry. Increasing the OP is related to reduced critical nucleation radius and so higher nuclei formation rate, however as the reactant concentration decreases dramatically in the vicinity of the electrode this will quickly become limited by diffusion. If a pulsed voltage profile is used, this can give time for fresh reactants to diffuse to the surface from the bulk and has been shown to give more uniform film growth.[141]

Electrodeposition was used in this work as a method of spatially controlling and directing the Te deposition on each sample prior to conversion to the desired TMD. This deposition method allowed a small, yet well-defined, amount of Te to be used in the reaction. It ensured that the deposited Te was always located directly in contact with the metal allowing for high local Te concentrations during conversion.

Cyclic Voltammetry

Cyclic voltammetry (CV) is a versatile technique that gives information on the potentials at which electrochemical processes occur. In this work, CV allowed the optimal potential for electrodeposition to be experimentally determined for each sample set. The simplest potential sweep technique is linear sweep voltammetry (LSV), this involves sweeping the applied electrode potential from an initial value,

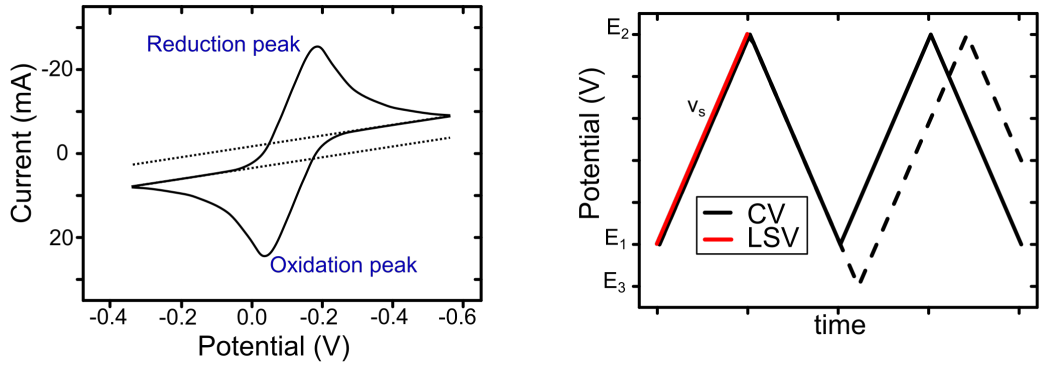


Figure 1.9: (a) A typical cyclic voltammogram with reduction and oxidation peaks labelled (b) Plot of the variation in applied potential with time in a LSV and CV.

E_1, to another final potential, E_2, at a known sweep rate, v_s. In CV, when the final potential is reached, the sweep is reversed, and the potential returns to E_1 or another value E_3, at which the potential reverses again as shown in Figure 1.9. This continues for a predetermined number of cycles.

It is usual to plot the measured current as a function of the applied potential for a CV. On this plot peaks correspond to Faradaic processes occurring at the electrode surface - oxidation and reduction events. The position and width of peaks measured under different conditions and scan rates can give a large amount of information about the system being examined.

A typical CV for a reversible reaction, as described by Equation 1.1, is shown in Figure 1.9. Initially only the oxidised species, O, is present. As an increasing negative voltage is applied to the cathode material O is reduced to R at an increasing rate. This holds until the initial concentration of O present near the electrode is depleted and diffusion of new reactant limits the current. The current measured begins to fall to the steady state level determined by diffusion. When the sweep direction is reversed, the reverse process takes place with R being oxidised to O.

Electrochemical Impedance Spectroscopy

In this work, electrochemical impedance spectroscopy (EIS) is used to measure the uncompensated cell resistance during the electrocatalytic measurements. Without compensating for this resistance, which is due to the solution and external elements of the circuit, a lower current than is realistic would be measured especially, in regions of higher OP.

The technique of EIS examines the electrochemical response of a system when an alternating potential is applied. The basis of EIS is the application of a small AC perturbation on top of a fixed DC potential between the electrodes. The perturbation frequency is varied over time allowing the response of the system, as a function of frequency, to be measured. EIS measurements are conducted in a potential region where there are no Faradaic processes occurring in the cell. In this region the system can be modelled as a capacitor and the uncompensated series resistance. By looking at the high-frequency region of the measurements, the capacitor will have effectively no impedance and the impedance measured is the real impedance of the uncompensated series resistance. This value can then be multiplied by the current and subtracted from the applied potential in the measured LSV.

1.3.2 Electrocatalysis

Many electrochemical reactions only occur at very high OP due to sluggish reaction kinetics. Electrocatalysts provide alternative, more kinetically favourable, reaction pathways in electrochemical reactions. The use of catalysts to reduce the OP required to achieve an appreciable reaction rate is widespread. This is normally achieved by changing the material or morphology of the electrode. By modulating the kinetics of the various reaction steps, the electrode can have a huge influence on the efficiency of a given reaction. The morphology of the electrode plays a large role in catalysis by changing the effective surface area and

also the type and density of catalytic sites available. In 2D materials, such as 2H MoS_2, it has been found that the basal plane is almost inactive for catalysis of the HER, however defects and edge sites are efficient catalystic sites.[142,143]

There has been a large amount of promising work using TMDs as electrocatalysts for various reactions, such as water splitting.[144] The broad trends found for TMD electrocatalysts are that semimetallic phases tend to be more active e.g. 1T' $MoTe_2$ vs 2H $MoTe_2$.[81,145] While the basal plane of semiconducting phases is generally reported as being relatively inactive, the creation of defects or functional groups can improve its behaviour.[146,147] In a similar vein, edge-sites and grain boundaries have been shown to be efficient catalytic sites in many cases, making polycrystalline films of TMDs interesting for electrocatlytic applications.[119]

Hydrogen Evolution Reaction

A major area of research for electrocatalysis is the efficient production of hydrogen through the HER. Realisation of this would have a plethora of benefits including improved energy storage to complement renewable energy production. At present one of the major challenges is that efficient hydrogen evolution requires expensive platinum-group catalysts.[148]

The activity of a catalyst towards the HER is measured using LSV. An increasing potential is applied in a three-electrode cell and the current as a function of the applied OP is measured. A higher current density at a lower OP is indicative of an efficient electrocatalyst.

By plotting the log of the current density versus the overpotential, the Tafel plot is obtained. Taking the slope of the linear region gives the Tafel slope, which is related to the kinetics of the reaction steps involved in the evolution of hydrogen. Hydrogen evolution in acid can proceed by either the Volmer-Tafel or Volmer-Heyrovsky mechanisms. The Volmer reaction step is the electrochemical reduction of a proton in solution and adsorption of an intermediate hydrogen

atom. If this is the rate-determining step, then a Tafel slope of 120 mV dec^{-1} is expected. Desorption of H_2 from the surface then occurs via either the Heyrovsky or the Tafel reaction. If the Heyrovsky step is rate determining a slope of 40 mV dec^{-1} to 120mV dec^{-1} is anticipated, depending on surface coverage. The Tafel reaction exhibits a slope of ∼30 mV dec^{-1}.[149]

Oxygen Reduction Reaction

The reduction of oxygen is technologically important as it is the desired cathode reaction in fuel cells and metal air batteries. The efficiency of fuel cells in particular is hampered by the high OP required to reduce oxygen at the cathode, even with the use of expensive Pt catalysts. While of great interest, it has proven challenging to find efficient catalysts for the ORR as many materials are not stable and may oxidise or reduce in the electrochemical region of interest.[139]

The reduction of oxygen requires the transfer of four electrons, and as such there are a large number of potential reaction mechanisms for the ORR. These mechanisms can be divided into two types. The first type involves complete $4e^-$ reduction and gives water as the only identifiable product. The other involves two steps with hydrogen peroxide as an intermediate.[139] The reactions for each in neutral or basic solutions are shown in Equation 1.6 and 1.7 respectively.

$$O_2 + 2\,H_2O + 4\,e^- \longrightarrow 4\,OH^- \tag{1.6}$$

$$O_2 + H_2O + 2\,e^- \longrightarrow HO_2{}^- + OH^- \xrightarrow[+2e^-]{+H_2O} \longrightarrow 4\,OH^- \tag{1.7}$$

Due to the may possible reaction pathways the mechanism of ORR can rarely be determined for certain. However, indications of which mechanism type is dominant for a particular case can be determined by the use of a rotating disc electrode.

1.4 Characterisation

1.4.1 Raman Spectroscopy

The following section will introduce Raman spectroscopy and briefly discuss the theory behind it. This section is adapted from the book by Ferraro, Nakamoto and Brown.[150]

Raman is an incredibly flexible, non-destructive characterisation technique that provides crystal structure information. Raman spectroscopy is based on the principle of Raman scattering of light, which was first discovered by Sir C.V. Raman in 1928, earning him the Nobel prize in physics two years later. When light is incident on a material (lattice or molecule) it can be absorbed, reflected or scattered. Of the photons that are scattered, the vast majority will scatter elastically, leaving with the same frequency ω_0 as the incident light, in what is known as Rayleigh scattering. In this case, after the energy is absorbed by the molecule and re-emitted, the molecule will return to the same energy state as it was initially in. About one in 10^7 photon however are scattered inelastically by interacting with molecular or lattice vibrations in the sample, this is Raman scattering. Here the frequency of the emitted photon will differ from that of the initial by a magnitude corresponding to the frequency of the molecular vibration which it excited or deactivated, $\omega_0 \pm \omega_q$.

If the molecule gains energy from the photon, it will be left in an exited state and a lower frequency photon, $\omega_0 - \omega_q$, will be re-emitted in what is known as Stokes scattering. If the molecule was initially in an excited state and after the interaction returns to the ground state, losing energy in the process, the photon emitted will have higher frequency, $\omega_0 + \omega_q$, known as Anti-Stokes scattering. The quantum mechanical Raman theory representation of this, involving virtual states, is shown in Figure 1.10(a), while Figure 1.10(b) shows the typical spectrum measured in Raman spectroscopy. As the vast majority of molecules are

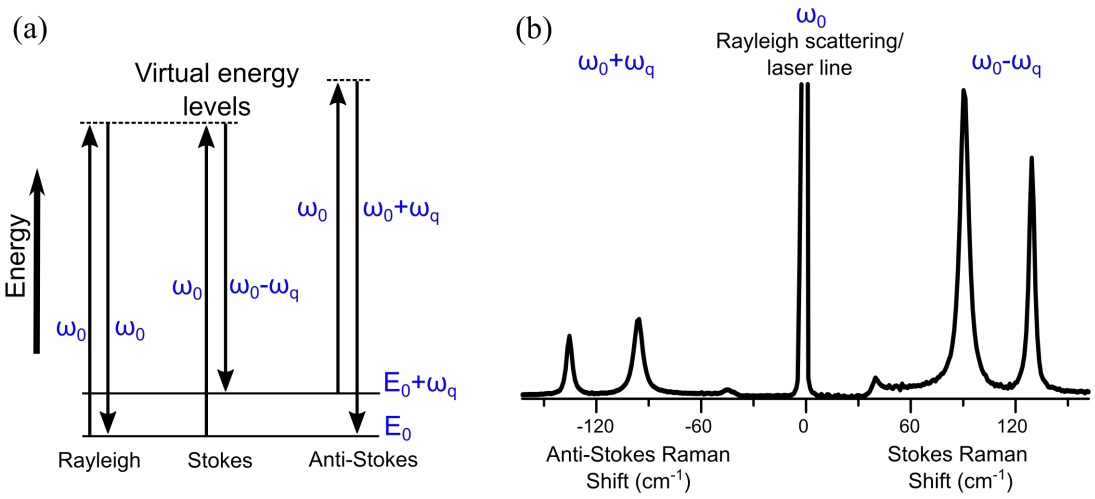


Figure 1.10: (a)The excitation to, and relaxation from, a virtual energy state for Rayleigh, Stokes and Anti-Stokes scattering. (b) Schematic of the Raman spectra obtained showing the three scattering types.

in the ground state at ambient temperatures, as predicted by the Boltzmann distribution, Stokes scattering will be much more intense.

A Raman spectrum is generally displayed as shift in wavenumber (inverse wavelength in cm) of the emitted photon relative to the incident light. This Raman shift represents the difference in energy between the incident and emitted photon, and so also gives the energy difference of the initial and final vibrational energy levels of the molecule involved in the transition.

While quantum mechanical Raman theory is needed to describe fully the Raman process, including resonant Raman scattering and the involvement of virtual energy states, classical Raman theory offers a good explanation for the majority of observed Raman effects. In this system the incident light interacts with harmonically oscillating atoms to induce an oscillating electric field and so a molecular dipole moment, μ, in the molecule. This is described by

$$\mu = \alpha E \tag{1.8}$$

where α is the polarisability of the molecule. This describes how the electric field E influences the electron density of the molecule. The interaction of the light

with the molecule can be fully described in the classical manner by the following equation

$$\mu(t) = \underbrace{\alpha_0 E_0 \cos(w_0 t)}_{Rayleigh} + \underbrace{\frac{1}{2}\left(\frac{\partial \alpha}{\partial q}\right)_{q_0} q_0 E_0 cos\left[(w_0 - w_q)\, t\right]}_{Stokes} + \underbrace{\frac{1}{2}\left(\frac{\partial \alpha}{\partial q}\right)_{q_0} q_0 E_0 cos\left[(w_0 + w_q)\, t\right]}_{Anti-Stokes} \quad (1.9)$$

where q is a normal coordinate of the molecule and t is the time. In this equation, the first term represents the Rayleigh scattering, which has the same frequency as the incident light. The second and third terms describe the Stokes and Anti-Stokes scattering respectively. In these cases, the frequency of the emitted light differs by the magnitude of the frequency of the molecular vibration excited.

Not all vibrational modes will be Raman active, this depends on the symmetry of the vibration. As can be seen in Equation 1.9, in order to be Raman active a vibration must change the polarisability of the molecule with respect to q, a normal coordinate of the molecule. Whether or not a vibration results in a change in polarisability can be determined by examining which symmetry group a molecule belongs to, and ascertaining the symmetry of the vibrational mode in question. Furthermore, if the excitation energy of the incident photon is close to the energy of an electronic transition in the material, the intensity of the Raman scattering will be greatly increased due to resonant Raman scattering.

Raman of TMDs

As a fast non-destructive technique Raman spectroscopy is widely used throughout material science, and has become a staple characterisation tool of nanomaterials. Raman spectroscopy can give insights into the crystallinity, strain and

layer number of these materials. In the case of TMDs, Raman is often used to gain insight into the quality and number of layers in a sample by examining the position, width and relative intensity of the visible peaks.

As already stated, the peaks visible in a Raman spectrum are determined by the symmetry of the sample. Bulk 2H MoS_2 belongs to the D_{6h} symmetry group and as a result displays two primary, characteristic Raman-active modes, the in-plane E^1_{2g} and the out-of-plane A_{1g} mode. The E^1_{2g} mode stems from the in-plane vibrations of the metal and chalcogen atoms, while the A_{1g} mode is a result of the out-of-plane vibration of the chalcogen atoms. In mono- and few-layer MoS_2 the separation of these two peaks can allow determination of the number of layers in a sample. Due to the lower symmetry of 1T' $MoTe_2$ and T_d WTe_2, they have a larger number of characteristic modes that cannot be easily assigned as in- or out-of-plane vibrations.

1.4.2 X-ray Photoelectron Spectroscopy

XPS is a powerful, surface sensitive, spectroscopic technique that allows the elements present in the sample, along with their chemical state, to be determined. The principle of XPS is based on the photoelectric effect. This is the emission of electrons from a sample that has been illuminated by electromagnetic radiation with a photon energy above a specific threshold. In an XPS system the sample is irradiated by predominantly monochromatic X-rays in a vacuum. The X-rays interact with the sample and cause emission of electrons by the photoelectric effect. The kinetic energy of the emitted electrons is governed by

$$E_{KE} = h\nu - E_{BE} - \phi_s \tag{1.10}$$

where $h\nu$ is the energy of the incident photon, E_{BE} is the binding energy of the atomic orbital from which the electron is emitted and ϕ_s is the work function of the spectrometer. The work function of the spectrometer and the energy of

the incident light are known and fixed, this allows the binding energy (BE) of the emitted electron to be determined by measuring the electron kinetic energy. X-rays with high enough energy to enable the emission of core-level electrons from the sample are chosen. This results in spectra with peaks of characteristic intensity and position that give elemental identification. The position, or BE, of a peak is a result of not only the energy of a particular atomic orbital but also of the chemical environment an atom is in. Depending on the bonding environment of an atom the core-level electrons will be screened to a greater or lesser extent resulting in a change in E_{KE} when they are emitted. This allows an atom's exact bonding configuration and chemical state to be determined using XPS, giving full chemical identification of the sample.

The mean free path of the emitted electrons is on the order of a few nanometres meaning that XPS is a very surface sensitive technique, making it ideally suited to the study of 2D and layered materials. In this work XPS was used to verify the chemical purity of grown materials and examine their stability and oxidation state.

XPS analysis and fitting

XPS measurements typically consist of an initial scan over a large range of binding energies, known as a survey scan, followed by more high resolution scans of regions of interest based on the material(s) being examined. These high resolution scans will focus on binding energies associated with specific core-level orbitals of interest. The peaks in these spectra are then fitted to give information about the chemical environment of specific atomic species.

The position of the orbital peaks are first charge corrected to the C 1s, adventitious carbon or C-C species, and then a background subtracted. The peaks are then fitted generally with Gaussian-Lorentzian peak shapes, the details of which vary depending on the material and XPS system. The position of the fitted peaks

then allow determination of the chemical state of the atomic species by reference to literature values. The majority of peaks examined in this work have doublets associated with each orbital due to spin-orbit coupling. The area of each of these spin-orbit split peaks will have a specific ratio based on their occupancies.

The area of the peaks is related to the abundance of the particular atomic species on the surface. This can therefore be used to give information on the relative amounts of different elements and compounds on the surface, once orbital sensitivity factors to different X-ray energies are taken into account. For example, when looking at an MoS_2 sample, comparison of the area of the Mo bound to S and Mo bound to O peaks can indicate the percentage of the Mo on surface in the form of molybdenum oxides compared to the amount as MoS_2. Furthermore, comparison of the Mo bound to S peak and the S bound to Mo, can give stoichiometry information on the MoS_2.

1.4.3 X-ray Diffraction

X-ray diffraction (XRD) is a non-destructive technique that is primarily used to study crystalline materials. It gives information on crystalline phase, lattice parameters, composition and strain. As X-rays have wavelengths of comparable magnitude to the lattice parameters of many materials, the crystalline lattice will act to diffract incident X-rays. At certain angles the diffracted beams from parallel crystalline planes will constructively interfere to produce a high intensity signal. The angle of such interference is dependent on the inter-atomic distances of the crystal and as such measuring this angle will allow determination of said spacings. This is quantified by Bragg's Law which states

$$n\lambda = 2d_{hkl}\sin\theta \tag{1.11}$$

where λ is the wavelength of the incident X-rays, θ the angle between the lattice plane(hkl) and the incident (or diffracted) beams, n is the order of the

diffraction and d_{hkl} is the perpendicular distance between planes of atoms (hkl) in the crystal. The diffracted X-rays only constructively interfere when the Bragg condition is satisfied.

XRD operates by directing a beam of monochromatic X-rays at a sample and measuring the intensity of the diffracted signal over a range of angles. If it is a single-crystal sample the Bragg condition will only be satisfied at specific angles. If a powder or polycrystalline sample is being examined, there will be grains in every orientation allowing all angle conditions to be concurrently satisfied.

1.4.4 Scanning Electron Microscopy

The following two sections on scanning electron microscopy (SEM) and TEM are adapted from *The Physical Principles of Electron Microscopy* by R.F Egerton.[151]

Imaging nanomaterials can be quite challenging due to their feature sizes often being below the diffraction limit of light, limiting the use of optical microscopy. Electron microscopies have been an invaluable alternative to provide information on the structure and morphology of these materials.

Electron microscopy is based on using the interactions of a beam of electrons with a sample to produce images that contain morphological, crystallographic and chemical information on the sample. In the case of SEM, a beam of high-energy electrons impinge on the sample and the resulting electrons that are emitted, are collected to form an image of the surface. The incident beam typically has an energy of 1 - 30 keV, it is focused onto the surface using magnetic lenses, and is rastered over the surface with scanning coils to produce the image, shown in Figure 1.11(a).

When these electrons impinge on the surface, they interact in a number of ways, resulting in a variety of signals that can be then detected to obtain information and build up an image of the surface. These signals are shown in Figure 1.11(b). Backscattered electrons (BSE) are scattered incident electrons

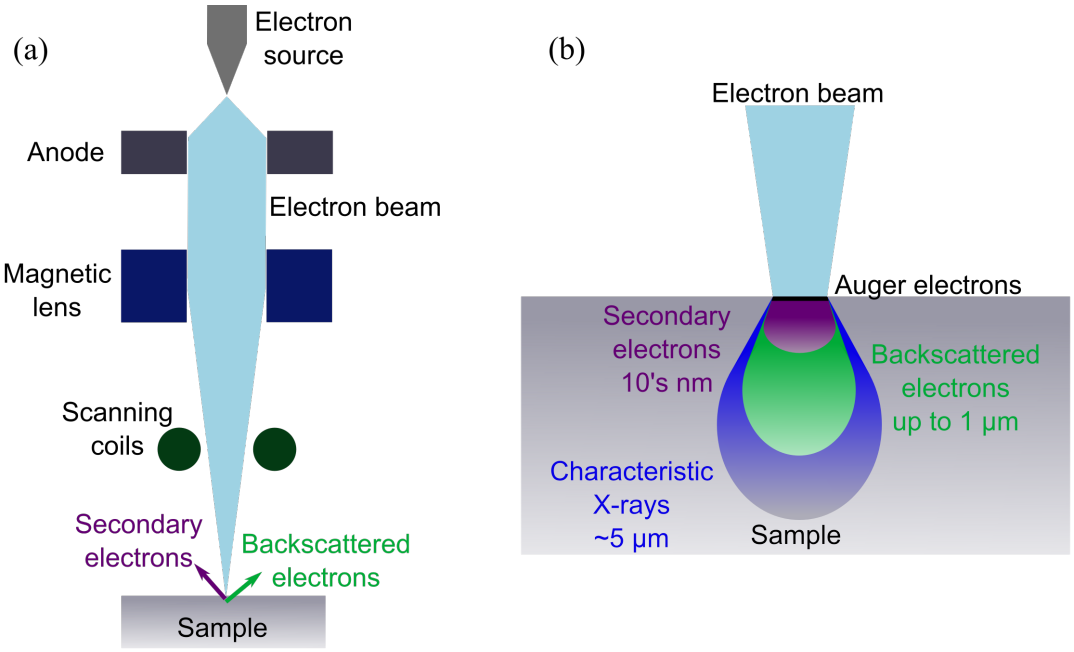


Figure 1.11: (a) Schematic of lens and rastering coils of SEM. (b) Diagram showing the approximate interaction volumes of the various signals measured in SEM.

that can be used to form an image. Since the cross-section for backscattering is greater for higher atomic number elements, they also give some elemental contrast in images. Secondary electrons (SE) are electrons that are knocked out of the sample by the incident beam. These have lower energy than BSE and as such will only escape from a smaller depth in the sample. Therefore they provide a more surface-sensitive image than BSE but do not give any elemental contrast. The incident beam will also cause the emission of X-rays that can be measured by energy-dispersive X-ray spectroscopy (EDX) and can be used to build up an elemental map of the surface.

The interaction volume of the electron beam is dependent on the accelerating voltage, with lower accelerating voltages giving more surface sensitive images. For this reason when examining nanomaterials it is common to use low accelerating voltages. In this work the majority of images were taking at an acceleration voltages of 3 keV. The absolute resolution of SEM is on the order of a couple of nanometres, however, this is quite sample dependent.

SEM is an integral part of nanoscience research offering a quick and versatile method to visualise and determine sample morphology. It is often used as a precursor for other techniques such as TEM. The topographical images obtained in this work facilitated the extraction of crystallite sizes and determination of film thickness and coverage.

1.4.5 Transmission Electron Microscopy

Similar to SEM, TEM also involves measuring the interactions of a beam of high-energy electrons with a sample. In TEM the samples being examined are sufficiently thin, and the electron energies sufficiently high, that it is the electrons which pass through the sample that are measured and used to extract information. TEM is a very powerful technique that offers both atomic resolution and information on long-range crystallinity of a sample through the use of electron diffraction patterns. Similar to SEM, analysis of elementally characteristic X-rays emitted from the sample is also possible.

There are two primary modes of operation of a TEM, parallel or convergent beam. These allow imaging in high-resolution transmission electron microscopy (HRTEM)) and scanning transmission electron microscopy (STEM) respectively. In parallel beam mode, a broad parallel electron beam passes through the sample. Contrast in the resultant image is provided due to scattering or diffraction of these electrons as they pass through the sample. This mode can also be used to obtain spot diffraction patterns of crystalline material. In convergent, STEM mode, the beam is focused to a point and rastered over the sample in a similar way to SEM. An image is then formed using a high-angle annular dark field (HAADF) detector, this image is more directly interpretable as atomic contrast than those obtained by TEM. STEM can be used to image a sample with sub atomic resolution.[151]

While it is an exceptionally powerful technique, there are a number of challenges associated with TEM including, damage to samples by the electron beam,

difficulties in obtaining representative sample information due to the extremely small sampling areas and the possibility of misinterpretation of images. Despite these difficulties, TEM is widely used in 2D materials research and can offer atomic-level information on sample crystallinity, size, shape, composition and defect levels. In this thesis HRTEM was used to examine cross sections of TMD films, while STEM was used to investigate the crystallinity of individual flakes of WTe_2.

1.4.6 Atomic Force Microscopy

Atomic force microscopy (AFM) is a form of scanning probe microscopy that takes advantage of the attractive and repulsive force between an atomically sharp tip and the surface of a sample to form an image of said surface.

The tip is brought close to, or in contact with, the surface then rastered across the sample. The interaction forces between it and the surface are measured through the deflection, or change in oscillation, of the cantilever on which the tip is mounted, as shown in Figure 1.12. The forces measured are from a combination of a number of different sources, such as van der Waals interactions, electrostatic, short-range chemical forces and magnetic interactions. These signals can then be used to form a topographical map of the surface. AFM is a very versatile technique which can be used in air, vacuum or liquid, in static or tapping modes. Through the use of special tips it can also provide magnetic, adhesion and electrical information.

AFM is an invaluable tool for the study of nanomaterials providing information on thickness, lateral dimensions, surface roughness and mechanical properties. A challenge of AFM is the very small areas it examines, though this can be offset by conducting complementary analysis by other techniques such as SEM.

1.5 Electrical Characterisation

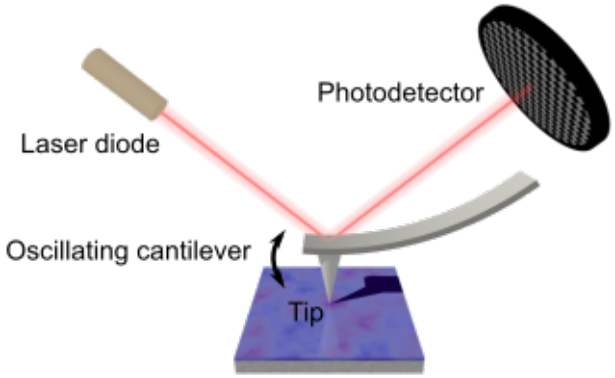


Figure 1.12: Diagram of AFM tip and cantilever

1.5.1 Heterojunctions

Heterojunctions have been the primary feature of electronics since the beginning of solid-state electronics.[152] A heterojunction is usually defined as an interface between two regions, or layers, of dissimilar crystalline semiconductors but can have a wider definition to include metallic junctions.[153]

Heterojunctions made from 2D materials offer a number of distinct advantages over traditional bulk interfaces. Traditional material combinations have always been limited by the need for appropriate lattice matching considerations between the layers, and consideration of interfacial states and bonds.[154] Heterojunctions of vertically-stacked 2D materials have only weak van der Waals interactions in the out-of-place direction. This greatly reduces issues regarding lattice matching of materials. With no dangling bonds perpendicular to the basal-plane, vertical heterostacks offer the opportunity for clean, atomically-sharp interfaces with no bonds between the layers. Furthermore, with the junction thickness on the order of 1 nm, it is possible to electrostatically tune both sides of the junction with very little screening[155].

The study of junctions is also important in the context of contact resistance in devices. The contacts to semiconducting devices are generally metals, leaving the possibility of Schottky barriers forming at the junction and thereby reducing

device performance. This has particularly been an issue for 2D materials with 3D contacts.[156]

P-n Junction Diode

The p-n junction is a component widely used as a photodiode, solar cell, temperature sensor and in various electronic circuits such as rectifiers.[157] A number of groups have successfully fabricated p-n junctions using a variety of 2D materials, primarily TMDs.[158,159]

The basis of a p-n junction is an interface between a region with electrons as the majority carrier (n-type semiconductor) and a region with holes as the majority carrier (p-type semiconductor). Figure 1.13(a) shows the band diagram for a typical type II p-n heterojunction. In equilibrium, the Fermi-level is equal throughout the system. This leads to a built-in potential and a region depleted of charge carriers, at the interface between the two sides of the p-n junction. In Figure 1.13(b) & (c) the junction is shown in forward and reverse bias respectively. In forward bias, the p-type material is biased positively with respect to the n-type. This serves to reduce the built-in potential at the junction and so lower the barrier to majority charge carrier conduction (diffusion current). As the barrier is lowered, more of the majority charge carriers on both sides have enough energy to cross, which causes an exponential increase in the current. If the junction is reverse biased, the built-in potential increases, meaning very little diffusion current flows, only a low level of drift current. This is the case until the breakdown voltage of the junction is reached.

Schottky Barrier Diode

Another widely used junction is the Schottky barrier, formed from the interface between a metal and semiconductor. This junction is an essential part of a MESFET, or metal-semiconductor field effect transistor. A 2D Schottky barrier

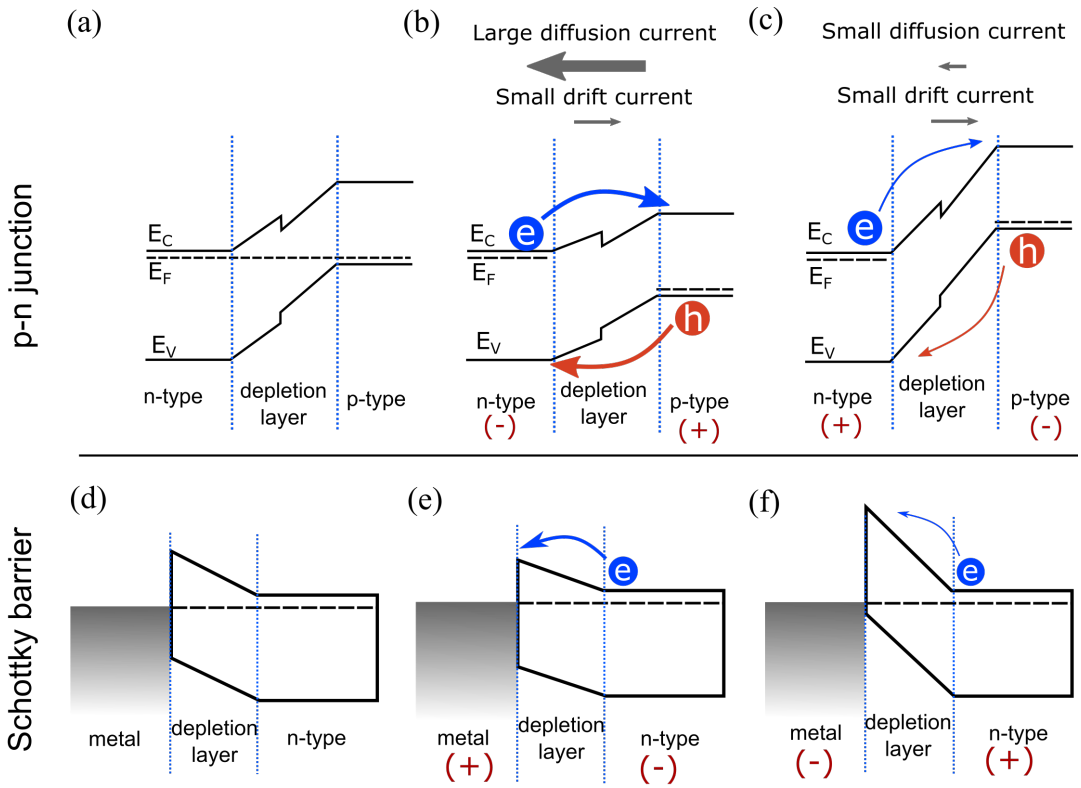


Figure 1.13: (a)Band structure of typical p-n heterojunction when unbiased. (b) The same junction forward biased with arrows showing flow of carriers contributing to the dominant diffusion current and (c) reverse biased with minor diffusion current shown. (d) Band diagram of unbiased Schottky diode consisting of metal and n-type semiconductor. (e) The same junction in forward and (f) reverse bias.

has been investigated by Sata *et al.* from MoS_2 and graphene[160]. Shanmugan *et al.* have reported a promising Schottky barrier solar cell fabricated from WSe_2[161].

At the interface between the metal and the semiconductor, a potential barrier is formed due to charge transfer. In the case shown in Figure 1.13(d), there is a transfer of electrons from the semiconductor to the metal resulting in a potential barrier being formed. When a positive voltage is applied to the metal (Figure 1.13(e)), this decreases the barrier height for electrons to flow from the semiconductor to the metal. The number of electrons in the semiconductor with energy greater than the barrier height increases exponentially as the barrier is lowered. The reverse is the case when a negative voltage is applied to the metal, see Figure 1.13(f). In both cases the barrier for a charge carrier moving from the metal to the semiconductor is unaffected.

Schottky barriers are useful junctions for many applications, but a comprehensive understanding of them is also necessary due to their propensity to form between metal contact electrodes and 2D semiconductors, reducing device performance. The simplest theory of a Schottky barrier suggests that the height of the barrier is simply the energy difference between the metal work function and the electron affinity of the semiconductor.[162] In practice however this is an over simplification with a number of factors, such as the E_f being pinned due to defect levels, or metal-induced gap statess (MIGSs), meaning that the barrier height can be hard to predict.[163]

2

Experimental

This chapter provides details of the various pieces of equipment and techniques used to synthesise and characterise the materials examined in this thesis. The theory and background of these is given in Chapter 1.

2.1 General materials

Tellurium pellets were ordered from Alfa Aesar, all other chemicals were ordered from Sigma-Alderich/Merck. All chemicals were used as received. Metal targets for metal film deposition were ordered from HMW-Hauner. All gases were supplied by BOC gases. 300 nm silicon oxide on silicon (SiO_2/Si) substrate wafers were purchased from University Wafers and Dasom RMS and consisted of 300 nm dry thermal oxide on Si(100). Nitto Denka BT-150E-CM tape was used during the transfer process of WTe_2 flakes.

2.2 Film synthesis

2.2.1 Metal deposition

Metal films of Mo, W and Pt for conversion to the various TMDs, were deposited on substrates using physical vapour deposition (PVD), either argon-ion sputtering or electron-beam (e-beam) evaporation. Argon-ion sputtering was performed using a Gatan Precision Etching and Coating (PECS) tool. The chamber pressure was ∼5 x 10^{-5} mbar during the deposition. The deposition rate was between 0.3 and 1 Å/second. A quartz crystal microbalance (QCM) was used to measure the deposition rate and to measure the nominal thickness of the metal films during deposition. This tool offered quick and versatile deposition but has limited through-put due to the sample size limitation ∼2 x 2 cm.

E-beam evaporation was carried out using a FC-2000 Temescal Evaporation System at 10^{-6} mbar. This tool has a throw distance of ∼1 m ensuring uniform coverage over samples. It also relies on a QCM to monitor both deposition rate and thickness of the film during deposition. The films were deposited at 1 Å/second except for the thinnest metal films which were deposited at a lower rate. This tool offered the ability to deposit on multiple samples per run.

For convenience, all TMD samples are named by referring to the thickness of the starting metal film, unless otherwise stated.

2.2.2 Tellurium electrodeposition

For the tellurium containing TMDs, Te was deposited onto the samples prior to conversion using electrodeposition. The electrodepostion was controlled by a Bio-Logic VMP-300 potentiostat. The Te was deposited using a three-electrode cell with the sample substrate as the working electrode, a Ag/AgCl working electrode and a Pt wire counter electrode, as shown in Figure 2.1. A 3D printed lid was used to ensure consistent placement of the electrodes during electrodeposition. The electrolyte was a 0.02 M solution of TeO_2 in 1 M HNO_3. The TeO_2 was

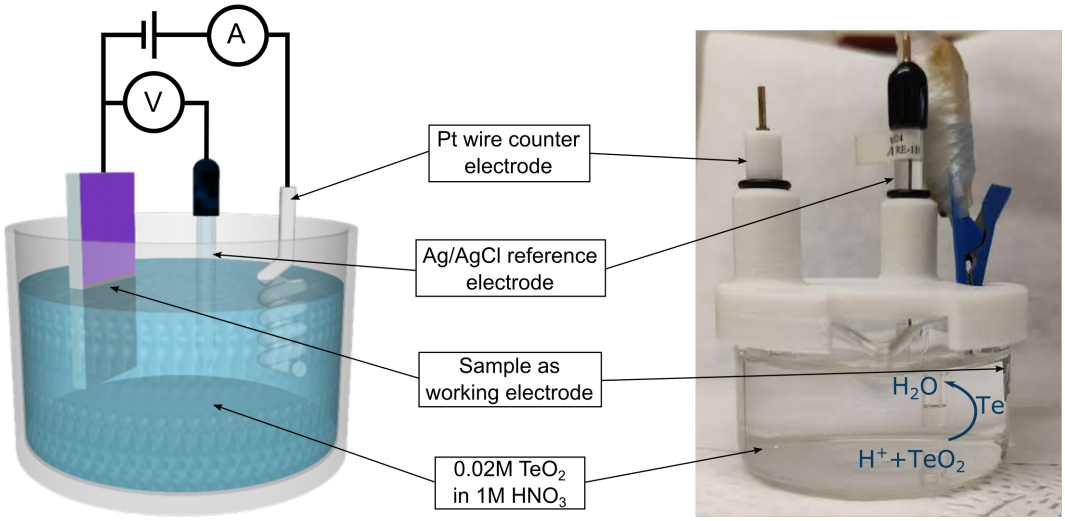


Figure 2.1: Labelled schematic and picture of the experimental set-up to electrochemically deposit Te on the transition metal film. The lid served to keep the electrode positioning consistent for every deposition.

reduced to Te (via the reaction shown in equation 2.1), which then deposited onto the working electrode.

$$HTeO_2^+ + 3\,H^+ \longrightarrow Te + 2\,H_2O \tag{2.1}$$

The reduction potentials were determined using CV for each sample batch. The CVs were run using the same experimental set-up as for the deposition with a sweep rate of 20 mV/s.

The deposition was primarily carried out using a pulsed deposition sequence at this potential (e.g. -0.3 V for $MoTe_2$). The pulse sequence consisted of 10 ms of -0.3 V followed by 50 ms of 0 V, applied to the working electrode with respect to the reference electrode. This was then repeated the desired number of times (1000 - 40,000). The number of pulses was varied depending on the thickness of the metal film, for typical 20 nm films of Mo, 15,000 pulses was used. Less were used for deposition on Pt as it was more conductive and so had a higher deposition rate(as signalled by the current measured) for the same applied voltage.

2.2.3 Film conversion: Sulfides and Selenides

To convert the pre-deposited metal layers to the equivalent TMD, they were exposed to sulfur (selenium) vapour in a low-pressure environment at an elevated temperature. This process is referred to here as TAC and is described in further detail in the work of Gatensby *et al.*[109] The process will be described here for an MoS_2 film, the growth of other films is similar. The SiO_2/Si substrate, with pre-deposited Mo film of the desired thickness, was placed in a home-made, quartz tube furnace with two heating zones, as seen in Figure 2.2. The tube was then evacuated, and the temperature of the high-temperature zone ramped to 800°C, under forming gas (90% Ar and 10% H_2, P∼0.7 Torr, 150 sccm). The forming gas helped to reduce any oxides present on the surface of the metal film.[164] The presence of H_2 was especially necessary for the growth of selenide TMD films due to selenium alone not being reactive enough. In the presence of H_2, H_2Se is formed which is much more reactive.[165]

Once the sample reached the growth temperature, the second hot zone was heated to melt the sulfur powder. The sulfur powder was heated to ∼117 °C, with the vapour carried downstream to the heated metal films. The growth time was 20 minutes, after which the chalcogen heating was removed, and the forming gas replaced with pure Ar gas, at the similar pressure and flow rate. The sample was then annealed at growth temperature for 30 minutes before being cooled to room temperature prior to removal from the furnace.

Separate, dedicated furnaces were used for growing the sulfide and selenide TMDs, but both processes are qualitatively similar. The primary difference was that the sulfur heater was an array of halogen lamps, while the selenium set-up had a furnace to heat the substrate and a second for the selenium source. The selenium films were held at growth temperature for 2 hours and the selenium source was heated to 220 °C.

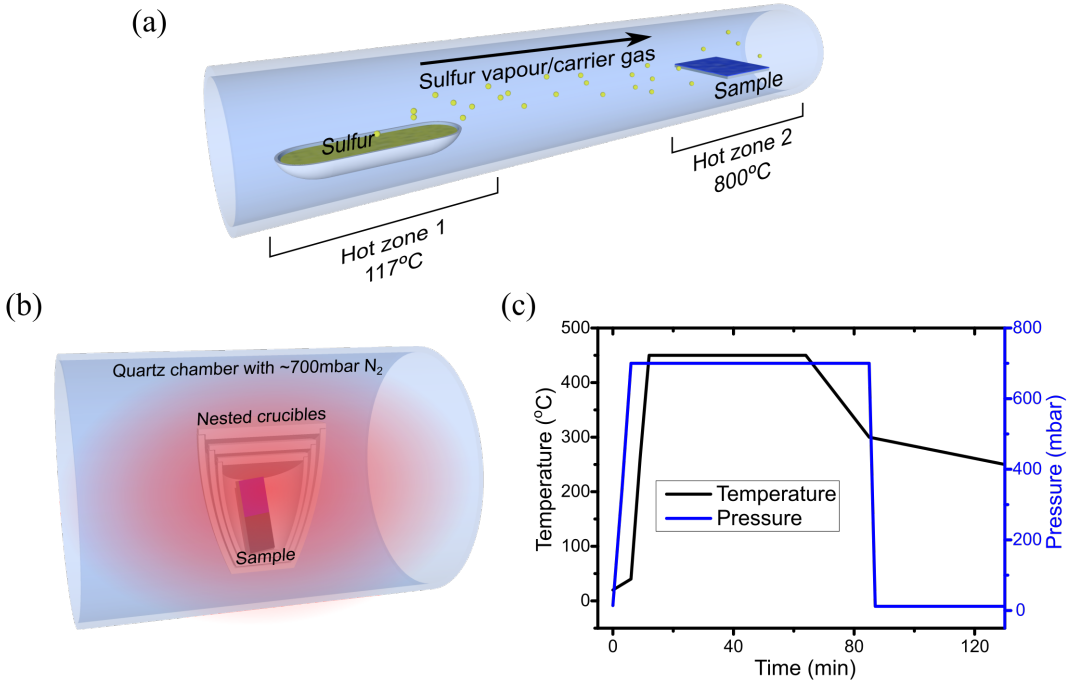


Figure 2.2: (a) Diagram of the quartz tube furnace for the growth of the sulfide TMDs. (b) Diagram of the quartz furnace and nested crucibles used to growth the telluride TMD samples. (c) The furnace temperature and pressure growth conditions for the $MoTe_2$ thin films. WTe_2 and $PtTe_2$ are similar with only the growth temperature and duration changed.

2.2.4 Film Conversion: Tellurides

To grow the telluride TMDs both the transition metal and tellurium were deposited on the sample prior to the furnace step. Following the deposition of both the transition metal and tellurium, the films were converted to the corresponding TMD (e.g. $MoTe_2$) in an ATV PEO 604 quartz furnace at a temperature between 450 °C and 650 °C. The reaction took place under a N_2 atmosphere at a pressure of ∼700 mbar. The samples were placed inside nested crucibles, as shown in Figure 2.2(b), this served to keep a higher partial pressure of Te in the local vicinity of the samples. The crucibles were not sealed with only the weight of the lids serving to keep the Te partially contained.

Shown in Figure 2.2(c) is a plot of the target temperature and pressure conditions during a furnace run. To begin each run the furnace was evacuated to 13 mbar and the temperature ramped to growth temperature at a rate of 180

°C per minute. Concurrently, the pressure was increased by flowing N_2 into the furnace. The pressure stabilised at ∼700 mbar before the growth temperature was reached. A 2 slm flow of N_2 was maintained throughout the process. The samples were held at the growth temperature for between 55 and 90 minutes depending on the process before being allowed to cool to <30 °C, under N_2, over a period of ∼3 hours, before removal from the furnace. During the cooling, at ∼320 °C, the pressure was lowered from 700 mbar to 13 mbar. If the pressure was not lowered, there was found to be an increased likelihood of Te crystals remaining on the surface of the film.

2.2.5 Pyrolytic Carbon Layer

Pyrolytic carbon (PyC) was grown on SiO_2/Si by a CVD process using an acetylene feedstock. Samples were placed onto a quartz shovel and loaded into a hot-wall, quartz-tube furnace pre-heated to 950 °C. The reaction chamber was evacuated to a pressure of <5 mTorr before the introduction of acetylene. During the growth period of 30 minutes, 180 sccm of acetylene was flowed over the samples, while the pressure was kept at 10 Torr. The acetylene was then turned off, and the gases evacuated before the furnace was back-filled with N_2 and the samples removed.

To ensure Te was only deposited on the front of the samples, the PyC was removed from the back of the SiO_2/Si wafers, using carbon tape, prior to the electrodeposition.

2.3 Characterisation

2.3.1 Raman Spectroscopy

All Raman measurements shown in this thesis were carried out on a WITec Alpha 300R Raman spectrometer using a 532 nm excitation laser. As some of the TMDs

were found to be quite sensitive to photodegredation a power of 200 μW was used for the analysis on the telluride TMDs, unless otherwise specified. Measurements were taken with a spectral grating of 1800 lines/mm or 600 lines/mm and a 100x objective lens. All spectra are either averages of maps or line scans. Maps were typically generated by taking scans every 400 nm in x and y directions over 10's of micrometers meaning averages are made up of >1000 spectra. Line scans were typically 30 point spectra with integration times of 3 seconds taken over 10's of micrometers.

2.3.2 X-ray Photoelectron Spectroscopy

XPS spectra shown here were taken using three different systems, two in Trinity College Dublin and one in the Universität der Bundeswehr in Neubiberg, Germany. All analysis was performed using CasaXPS software. Spectral components were fitted using a Shirley background subtraction and appropriate line shapes. Relative atomic percentages were calculated using the relative sensitivity factors provided by the software CasaXPS.

The XPS shown in Chapter 3 was taken with a VG Scientific ESCAlab Mk II system with an Al Kα x-ray source. The XPS in Chapter 4 was measured using monochromated Al Kα X-rays from an Omicron XM1000 MkII X-ray source and an Omicron EA125 energy analyser. An Omicron CN10 electron flood gun was used for charge compensation. Core-level scans were recorded at an analyser pass energy of 15 eV.

For the XPS measurements in Chapter 5 and 6, a PHI VersaProbe III instrument equipped with a micro-focused, monochromatic Al Kα source (1486.6 eV) and a dual beam charge neutralization was used. Core level spectra were recorded with a spot size of 100 m and a pass energy of 69 eV using PHI SmartSoft VersaProbe software, and processed with PHI MultiPak 9.8. Sputter XPS depth profiling was conducted using 1 keV Ar ions. Binding energies were referenced

to the adventitious carbon signal at 284.8 eV. After subtraction of a Shirley type background, the spectra were fitted with Gaussian–Lorentzian peak shapes.

2.3.3 X-ray Diffraction

The XRD measurements were performed on a Bruker D8 Discover diffractometer with a 148 monochromated Cu K-alpha source. The measurements were taken using a θ-2θ configuration.

2.3.4 Atomic Force Microscopy

AFM was carried out on a Bruker Multimode 8 in ScanAsyst Air 146 mode using Nanosensor PointProbe Plus tips. The images were analysed using Gwyddion software.[166]

2.3.5 Line profilometry

Line profilometry measurements to find the thicknesses of films were taken using a Dektak 6M Stylus Profiler.

2.3.6 Scanning Electron Microscopy

SEM images were obtained with a Karl Zeiss Supra microscope operating at 3 kV accelerating voltage, 30 μm aperature and a working distance of typically 3 - 4 mm. Primarily the acquisition was using BSE and the inlens detector.

Throughout this work SEM images were analysed to extract various physical morphological parameters of the films. To extract grain sizes a number of SEM images across a sample were taken and the size ∼30 random grains in each were measured by hand before an average value was taken. To measure the thickness of deposited Te films the samples were first cleaved and a number SEM images taken of the break. The height was then measured in 5+ places in each of the images to obtain an accurate value. The surface coverage of samples was calculated

by using the 'Mask Grains by Threshold' feature in Gwyddion to highlight the covered area, which could then be compared to the overall image size.

2.3.7 Transmission Electron Microscopy

Cross-sectional TEM imaging of $MoTe_2$ was carried out using a JEOL JEM-2100 TEM. Cross-sectional TEM lamallae were prepared using a dual beam focussed ion beam (FIB) FEI Helios NanoLab 600i. A 50 nm carbon layer which was followed by a 300 nm platinum layer were deposited within the dual beam FIB by electron beam induced deposition and a 2 µm thick carbon layer was then deposited by ion beam induced deposition. These three layers were deposited for protection before the milling process. The lamella was prepared and thinned down to less than 200 nm thickness.

HRTEM analysis in Chapter 5 was performed in an FEI Titan TEM at an acceleration voltage of 300 kV. Atomic-resolution STEM images were obtained with a Nion UltraSTEM 100, using a HAADF detector, operated at 200 kV.

2.3.8 Electrical measurements

The sulfide and selenide TMD films were fabricated into devices by using shadow masking during deposition to pattern the initial metal film, and so the TMD, into the desired geometry. The contacts were subsequently also deposited with shadow masking by either e-beam evaporation or sputtering. They typically consisted of 5 nm of Ti covered with 40 nm of Au.

The WTe_2 devices were fabricated by transferring WTe_2 flakes onto a SiO_2/Si substrate. The contacts were then defined using electron-beam lithography (EBL) on a Karl Zeiss Supra microscope. The Ti/Au (5nm / 100nm) metal contacts were then deposited using e-beam evaporation.

EBL involves first covering the sample in a layer of electron-beam sensitive resist through spin coating. This negative resist is then patterned in an SEM

by exposing the desired areas to an appropriate dose of electrons. These areas can then be removed with a solvent before the contact metal is deposited using e-beam evaporation. The remainder of the resist can then be removed. As the pattern for each sample is designed based on sample measurements, EBL offers the advantage of precise, small-scale and unique patterning of irregular samples. It does however become time-consuming and expensive for processing of large numbers of devices and, as such is not widely used in industrial processes.

The electrical characterisation of the TMD devices was carried out using two systems, one in vacuum ($\sim 10^{-6}$ mbar) and the other in air. The air system was a Karl Suss probe station connected to a Keithley 2612A source meter. The vacuum system was a Janis probe station connected to a similar Keithley system. The voltage was applied through needle-probes, contacting gold electrodes deposited on the TMD films. The measured current was gathered and plotted automatically using Labview software to give current-voltage(IV) curves.

2.3.9 Electrochemical characterisation

Catalytic activity of the films for the HER was measured by performing LSV and EIS with either a Gamry Reference 3000 or 600 potentiostat. The samples were measured in a three-electrode electrochemical cell with sulfuric acid (0.5 M) as the electrolyte. The TMD film was the working electrode, a large graphitic as the counter electrode and a Ag/AgCl reference electrode. All potentials quoted are given as OP, the measured potential was converted to overpotential using the Equation 2.2.

$$E_{OP} = E_{\text{measured}} + 0.2\text{V} \tag{2.2}$$

This conversion is needed as the reference used, Ag/AgCl, has a potential of 0.195 mV with respect to the standard hydrogen electrode under these conditions.

Sample conditioning was performed prior to each test. Linear voltage sweeps

were performed at a scan rate of 5 mV s^{-1} in a voltage range -0.2 V to -1.2 V (vs Ag/AgCl). EIS in the frequency range of 0.1 to 10 MHz with perturbation voltage amplitude of 10 mV was used to determine the equivalent series resistance of the system. All the data was corrected for the electrolyte resistance by iR compensation.

Chronoamperometry was carried out using the same experimental set-up with a fixed potential applied for a period of time and the current response measured. This data was not iR compensated.

ORR measurement were performed in a three-electrode electrochemical cell with 1M NaOH as the electrolyte. The TMD film was the working electrode, a graphitic rod as the counter electrode and a Hg/HgO reference electrode. To remove oxygen from the electrolyte it was purged with Argon for 20 minutes prior to some of the measurements.

2.4 Acknowledgement of contributions

XPS results shown in this work were measured by either Conor Cullen in Trinity College Dublin or by Tanja Stimpel-Lindner in the Universität der Bundeswehr in Neubiberg, Germany. All spectra were analysed and fitted by Conor Cullen.

XRD results were measured and analysed in collaboration with Daragh Mullarkey.

The cross-sectional TEM shown in Chapter 4 were carried out by Farzan Gity at the Tyndall National Institute in Cork. The HRTEM and STEM measurements in Chapter 5 were carried out by Clive Dowling at the Advanced Microscopy Lab, Trinity College Dublin.

The EBL to define the WTe_2 electrical devices in Chapter 5 was performed by Lisanne Peters.

The ORR measurements in Chapter 6 were performed by Michelle Browne of the University of Chemistry and Technology, Prague.

3

Sulfide and Selenide TMDs

3.1 Introduction

The study of TMDs thus far has predominantly focussed on the Group VI sulfides and selenides, MoS_2, $MoSe_2$, WS_2 and WSe_2, with MoS_2 being a particular focus. Between them, these materials have demonstrated a wide array of interesting physical and chemical phenomena along with potential applicability in a number of industries.

MoS_2 has been mined as molybdenite throughout history, though was often confused with lead sulfide and graphite.[167] Similar to graphite, there has been some research on very thin sheets of MoS_2 for a long time.[15,168] As such, it was a natural material to investigate on the nanoscale after the interest generated by graphene in 2004.

The most stable form of MoS_2, $MoSe_2$, WS_2 and WSe_2 is the semiconducting 2H polytype.[28] MoS_2 has an indirect bandgap of 1.3 eV in the bulk, while the bulk bandgap values of $MoSe_2$, WS_2 and WSe_2 are 1.1, 1.4 and 1.2 eV respectively.[28,169] One of the properties that generated much of the initial interest in MoS_2 is the ability to substantially tune its bandgap by controlling its thickness - monolayer MoS_2 has a 1.9 eV direct bandgap.[12] The origin of this change is

the varying sensitivity of different parts of the MoS_2 band structure to interlayer interactions.[170] Band structure variation with layer number has also been shown for other TMDs.[169]

Much of the excitement around the sulfide and selenide TMDs has been due to their layer dependent properties and potential for use in future electronic devices.[16] The majority of studies report that MoS_2, WS_2 and $MoSe_2$ are n-type, while WSe_2 is ambi-polar, due to intrinsic defects in these materials.[171] However, especially in ultrathin devices, the dominant carrier type of TMDs has been found to depend on a number of factors including the growth method, contact metal choice and substrate effects.[172–174] Intentional doping of TMD layers has likewise been shown to be possible using various techniques such as plasma treatments and chemical functionalisation.[175–177] Semiconducting TMDs have also demonstrated their suitability for low-power electronics with high on/off ratios and competitive carrier mobilities.[16]

When combined as vertical heterostructures, TMDs offer devices with atomically sharp, bond-free interfaces without the need for lattice matching considerations.[178] As semiconductors with complementary carrier types, along with numerous potential avenues for doping to adjust the carrier levels, this opens up a wide range of possibilities for fabrication of "all 2D" devices, namely p-n junctions or FETs.[179] Group VI TMDs have also been studied for a wide range of other applications including optoelectronics energy storage, thermoelectrics, and for their spin- and valley properties.[180,181]

The majority of the applications discussed so far require high-quality material with large crystals and low defect density. This makes polycrystalline films unsuitable due to their grain boundaries and defect densities that severely limit carrier mobilities and ability to gate.[118] Conversely, there are a number of applications where polycrystalline thin-films of TMDs, such as those made by TAC, have been shown to be advantageous. 2D materials are especially suited for use

in sensors and for catalytic applications due to their high surface-to-body ratios. Polycrystalline TAC films have been shown to be ideal for chemiresistor electronic gas sensors.[118] MoS_2 and $MoSe_2$ films with a high density of edge- and defect sites have also shown very promising catalytic behaviour for the HER.[119,182]

In this chapter polycrystalline films of MoS_2, $MoSe_2$, WS_2 and WSe_2 will be synthesised and characterised. Heterostructures of these will then be investigated to give further insight into the interface properties between the films.

3.2 Growth of TMD films

The TMD thin-films were produced using the process described in Section 2.2.3. While the process for each TMD was qualitatively similar, there were a number of differences depending on the film to be produced.

Specifically, a metal film was deposited on a SiO_2/Si substrate by either e-beam evaporation or argon sputtering, with device geometry defined by shadow masking. The films in this work are named based on the starting thickness of the deposited metal layer, as measured by the deposition tool QCM. For example, a 2 nm MoS_2 films implies a starting Mo thickness of 2 nm was deposited and then converted to MoS_2. This metal film was then reacted with chalcogen vapour, at an elevated temperature, in a quartz-tube furnace. A low pressure, inert atmosphere was maintained in the furnace throughout the growth.

The transition metal disulfides and diselenides, while starting from similar metal thin films, were grown in different furnaces. During the growth, the temperature of the sulfur and selenium was set to just above their respective melting points at ∼117 °C and ∼220 °C. The disulfide films had a 20 minute dwell at growth temperature followed by a 30 minute post-growth anneal without S vapour present. In contrast, the diselenide films had a dwell time of 120 mins at growth temperature, with a 30 mins anneal. Previous work has shown that shorter dwell times can result in incomplete selenisation of the metal film, potentially due to

Table 3.1: Growth conditions for TMD film by TAC

Material	Temperature	Growth time
MoS_2	800 °C	30 mins
WS_2	800 °C	30 mins
$MoSe_2$	800 °C	120 mins
WSe_2	600 °C	120 mins

the lower reactivity of selenium than sulfur.[183]

The growth temperatures for the various TMD films are shown in Table 3.1. MoS_2, $MoSe_2$ and WS_2 were grown at 800 °C, while WSe_2 was grown at 600 °C. The use of a lower growth temperature for the WSe_2 was as a result of previous experimental work in the group. These investigations found that WSe_2 did not grow at 800 °C but only in a narrow temperature window around 600 °C.[183]

During the conversion the chalcogen is vaporised in the upstream low-temperature zone and transported by the carrier gas to the high-temperature reaction zone, where it reacts with the metal films to form the TMD. The chalcogen is supplied in quantities that ensures it is in excess during the growth phase, enabling full conversion of the metal film.[123] Despite being relatively straight forward, the TAC growth used here does have have some drawbacks. It does not allow for precise control and repeatability over the chalcogen concentration, which may lead to run-to-run variation. Furthermore, this excess can result in high amounts of chalcogen condensing inside the furnace. This requires precautions, such as air handling systems and appropriate personal protective equipment (PPE), to be used when opening the furnaces.

3.2.1 TMD film characterisation

Conversion of metal films via the TAC process was confirmed using Raman spectroscopy and XPS. Raman spectroscopy is an extensively used technique for analysis of TMDs, providing a quick and reliable confirmation of the growth of the desired TMD. Figure 3.1 shows Raman spectra of a)MoS_2, b)WS_2, c)$MoSe_2$ and

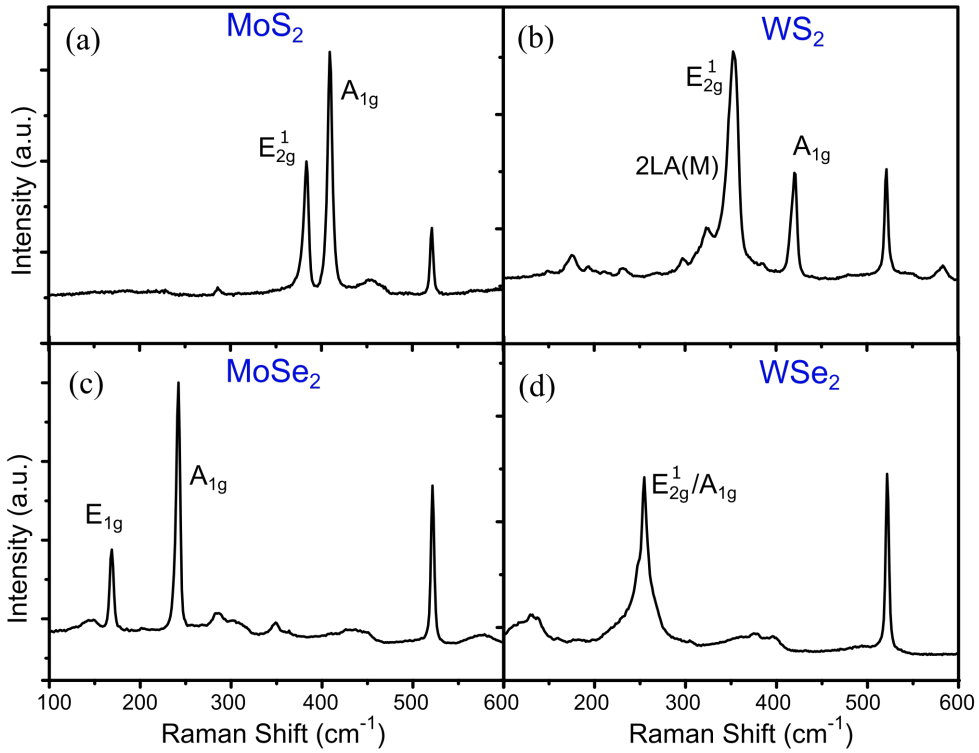


Figure 3.1: (a)-(d) Raman spectra of TMD films with characteristic peaks labelled.

d)WSe_2 films, all with starting metal film thickness of 5 nm on a SiO_2/Si substrate. By identifying characteristic Raman modes for these materials, it was found that all spectra are consistent with their values in polycrystalline bulk form.[184–186]

Further confirmation of the successful growth of each TMD was obtained with XPS. The XPS spectra of MoS_2, $MoSe_2$, WS_2 and WSe_2 thin-films can be seen in Figure 3.2(a),(b),(c) and (d) respectively. All show that the films consist predominantly of the expected TMD, with a small amount of metal oxides present in each case. For both WS_2 and WSe_2 there is also a small quantity of metal atoms that are present in an elemental state, with this being a larger component in the WSe_2 films.

These techniques offer strong evidence that the synthesis of the TMD films, by conversion from the corresponding metals, was successful under the conditions described.

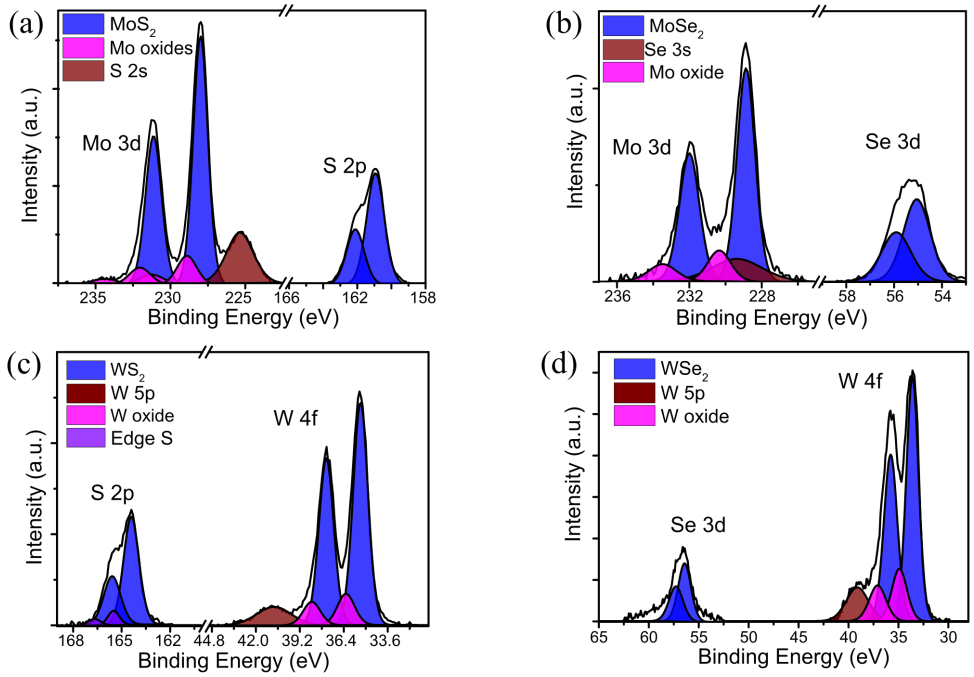


Figure 3.2: (a) & (b) XPS spectra of the Mo 3d and S 2p (Se 3d) regions of MoS_2 and $MoSe_2$ respectively, (c) & (d) XPS spectra of the W 4f and S 2p (Se 3d) regions of WS_2 and WSe_2 respectively. All peaks were first charge corrected to the C 1s orbital at 284.8 eV.

3.2.2 Film morphology

The deposited films were examined before and after conversion using line profilometry. This allowed the thickness of the deposited metal films and corresponding TMD films to be determined. The samples were patterned by shadow masking during deposition to facilitate a more accurate height measurement from the profilometry. While profilometry provides an effective and quick method to measure the film thickness, the error associated with these measurements is on the order of nanometres, resulting in potentially quite a large percentage error for thinner films. As such, the following numbers will be primarily used for the discussion of trends rather than absolute values. A more reliable measurement of film thickness could be obtained using a technique such as spectroscopic ellipsometry or AFM.

Figure 3.3 shows the extracted thickness of the patterned films for Mo, W,

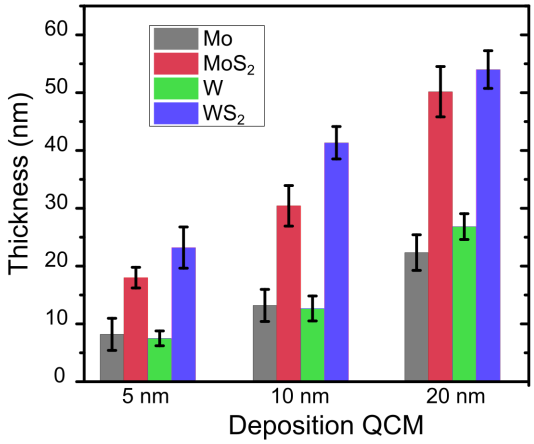


Figure 3.3: Extracted thicknesses from line profiles for Mo, W, MoS_2 and WS_2 with the thickness measured by the deposition tool shown on the x-axis.

MoS_2 and WS_2, with the x-axis being the nominal thickness of the film as measured by the deposition tool QCM. Firstly, it is clear that the metallic films are slightly thicker than is measured by the QCM. This should be kept in mind throughout this work, but it does not affect the results in a material way. The convention of referring to films by the thickness of the starting metal film, as measured by the deposition tool QCM, will be kept for convenience.

The converted MoS_2 and WS_2 films show thicknesses 2 - 3 times that of the initial films, with the WS_2 being usually thicker than the MoS_2. This expansion is expected due to the intercalation of S atoms into the film during the conversion.[109] The unit cell of MoS_2 is ~3 times that of Mo (106Å^3 vs 31Å^3). The selenide films tend to show larger expansions factors of about 3 times, which can potentially be explained by the larger atomic radius of Se versus S (the volume of the $MoSe_2$ unit cell is 121Å^3).

The morphology of the converted films was examined using SEM, Figure 3.4. The films show uniform growth with small grain size on the order of tens of nanometres and random grain alignment with respect to the surface and each other. Previous works have shown that the grain size of TAC films can be increased by using more crystalline substrates, such as sapphire, or increasing the growth temperature.[116] The roughness of MoS_2 films of different thickness were

Table 3.2: Thickness and roughness of Mo/MoS_2

Deposited Mo Dep. tool QCM	Mo Thickness Line Profilometry	MoS_2 Thickness Line Profilometry	MoS_2 Roughness AFM
5 nm	8.2±2.8 nm	18±1.8 nm	4.5 nm
10 nm	13.2±2.8 nm	30.4±3.5 nm	7.5 nm
20 nm	22.3±3.1 nm	50.2±4.4 nm	13.9 nm

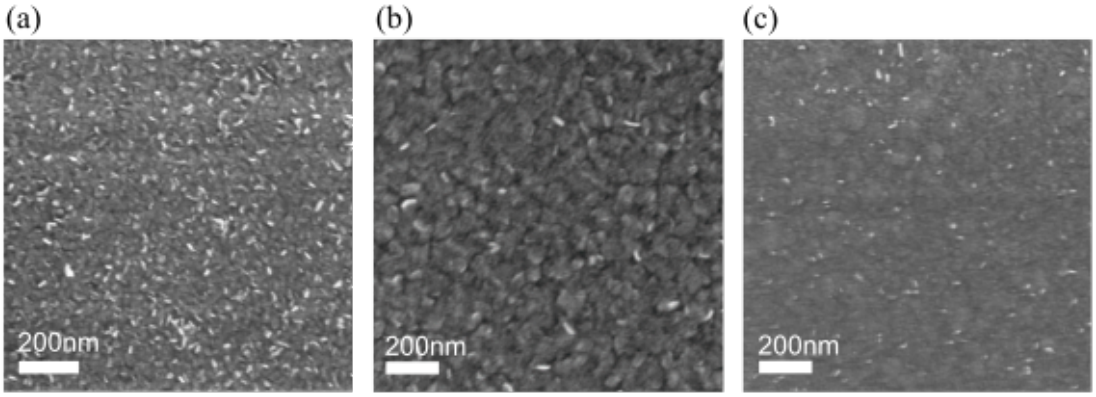


Figure 3.4: (a)-(c) SEM images of 10 nm MoS_2, 10 nm $MoSe_2$ and 20 nm WS_2 films respectively.

subsequently found using AFM and are shown in Table 3.2, along with the line profilometry data previously shown in Figure 3.3. All the films are quite rough, with the roughness increasing for the thicker films.

3.2.3 Electrical characterisation of films

To characterise their electrical properties, interdigitated electrodes (IDE) were deposited on the TMD films, as shown schematically in Figure 3.5(a). The Ti (5 nm)/Au(60 nm) contacts were deposited using e-beam evaporation, in a geometry defined by a shadow mask. Typical current-voltage characteristics of a 2 nm MoS_2 film are shown in Figure 3.5(b). The current response is linear in all regions of applied voltage, which is generally understood to indicate Ohmic contacts. However, it has been shown that linear IV response in 2D materials does not always imply a lack of a Schottky barrier at the contact junction.[187] The pinning of the TMD Fermi level due to MIGS and surface defects can play a large role in

the contact resistance.[163]

The films of $MoSe_2$, WSe_2 and WS_2 all demonstrated similar linear behaviour. Figure 3.5(c) shows average sheet resistance values of the 2 nm TMD films measured in the same IDE configuration. The error bars indicate the standard deviation of the sheet resistances measured. The contact metals used for each film was Ti/Au. From work function matching considerations, Ni is often suggested as a suitable contact metal for WSe_2[188], but due to the lack of electron affinity data for these films it was decided to use a consistent contact metal for each. Furthermore, it is likely that Fermi level pinning, due to defects and MIGS, will dominate any workfunction matching considerations.

There is a large amount of variation in the film resistances between samples of the same materials. MoS_2 and $MoSe_2$ both show resistances that vary by an order of magnitude. There are a number of possible explanations for this behaviour. The polycrystalline nature of the films means that grain boundaries are likely to dominate the electrical behaviour. Thus, variation in domain sizes and type of grain boundaries could greatly affect resistance values. Variation in defect levels, and hence unintentional doping, is another parameter that could explain the observed variability of the resistance values.

The sheet resistance values are difficult to compare meaningfully with literature values due to the polycrystalline nature of the films and uncertainty in film thicknesses. However, an estimated resistivity of the samples is shown on the right axis of Figure 3.5(c) by assuming the thickness of the films to be 5 nm. The MoS_2 films have an average resistivity about an order of magnitude above that of the literature value for crystalline MoS_2. Both WS_2 and $MoSe_2$ display resistivities 3 orders of magnitude above literature values for bulk crystals.[189] These values are not surprising due to the thin, defective, polycrystalline nature of the films. This would result in high levels of charge carrier traps, surface states and scattering centres. It is also consistent with other reports for similar films.[112]

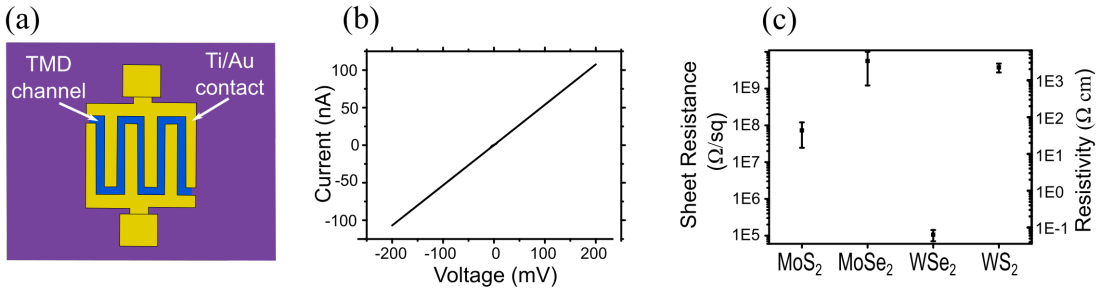


Figure 3.5: (a) Schematic of IDE configuration for electrical characterisation of TMDs films. (b) Source-drain IV measurement of 2 nm MoS_2 film. (c) Average sheet resistance/resistivity values for TMDs.

The resistivity of WSe_2 is anomalously low when compared to the other TMDs. It is also two orders of magnitude below the value for a bulk WSe_2.[189] This indicates that the film is likely not converting fully to the TMD, which is consistent with the observation of elemental W present in the XPS spectrum. It was highlighted earlier that the WSe_2 film had to be grown at a lower temperature (600 °C) than the other three TMDs examined. The electrical analysis of the films shows that even at this temperature the conversion is likely incomplete. An alternative recipe would need to be developed to successfully grow phase-pure films of WSe_2.

This analysis also indicates the importance of using a range of characterisation techniques when examining films such as these. Raman indicated the successful growth of WSe_2, but did not show the presence of unconverted W or oxides, these were picked up by XPS. Neither of these techniques however, gave any information on the crystallinity or morphology, that was highlighted by SEM and AFM. Finally, the combined influence of all these factors on the film properties could only be understood fully by electrical measurements.

3.3 TMD film heterostructures

The ability to combine different TMDs is an essential step on the path to creating 2D devices. One method of combining TMDs into devices is by creating vertical

stacks or heterostructures. In such cases, understanding the properties of the interface between these materials is extremely important, as it defines many of the properties of the structure itself.

A common junction between semiconducting materials is a p-n junction diode ,which rectifies current due to the formation of a depletion layer between the two materials. This depletion layer acts as a potential barrier to charge carriers and results from an offset between the Fermi levels, conduction band (CB) and valence band (VB) of the two semiconductors. This band alignment will influence the strength of the rectification characteristics displayed. While both are n-type materials, due to the small band offset between MoS_2 and WS_2 they have been shown to for rectifying heterojunctions. However due to their differing carrier types, $MoSe_2$ and WSe_2 are expected to have a much larger offset and would form a junction with stronger rectification characteristics.[190,191]

When choosing which TMDs to combine to create p-n junction heterostructures (referred to here as stacks) there were a number of practical considerations to take into account. Separate furnaces were used to grow the sulfide and selenide TMDs, due to the tendency of S to displace Se in TMDs. Therefore, only MoS_2/WS_2 and $MoSe_2/WSe_2$ junctions were examined. These stacks could be created in one of two ways. Either both metals could be deposited, before both are converted to the corresponding TMD concurrently. These are referred to as co-converted samples. Alternatively, one metal is deposited and converted, before a second metal is deposited on top and converted in a second furnace run. This is referred to as sequential conversion. Both methods are illustrated in Figure 3.6(a). As $MoSe_2$ and WSe_2 are grown at different temperatures, it was only possible to convert the selenide stacks sequentially.

Heterojunctions of co- and sequentially converted MoS_2/WS_2 and sequentially converted $MoSe_2/WSe_2$ films were investigated. These were created with the cross structure shown in Figure 3.6(a). All of the TMDs were grown from 5 nm metal

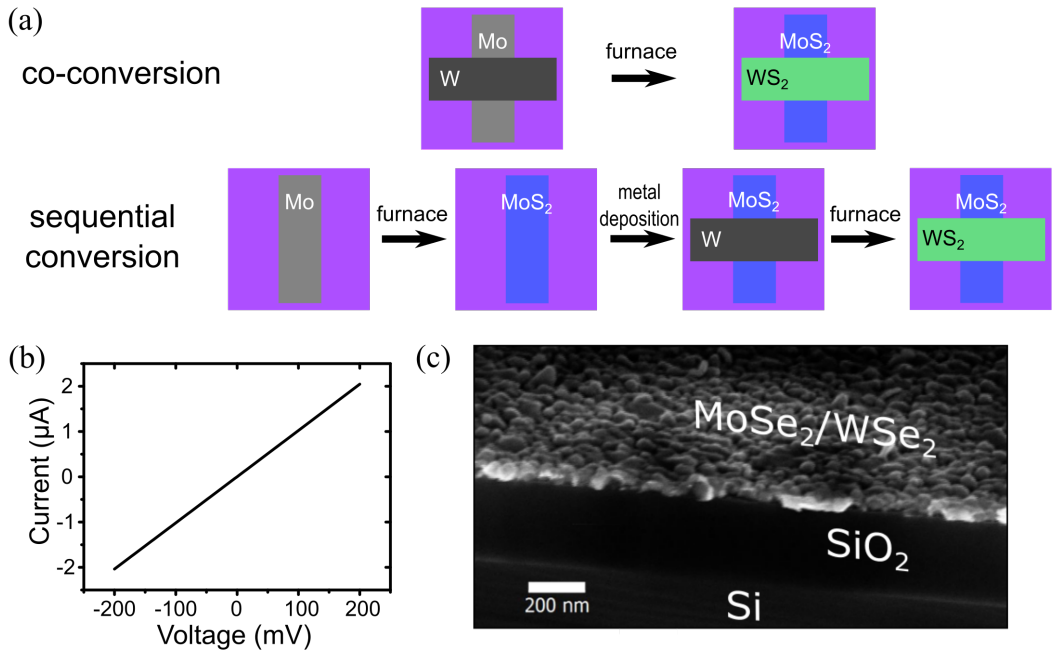


Figure 3.6: (a) Diagram of structure of heterostructures and showing co-conversion and sequential conversion processes (b) Two-terminal IV measurement of a MoS_2/WS_2 heterostructure.(c) Cross-section SEM image of sequentially converted $MoSe_2/WSe_2$ heterostack. Each film was grown from 5 nm deposited metal and the image was taken by cleaving the substrate and imaging along the break interface

films with Ti/Au contacts. These devices all behaved qualitatively in the same manner, an example of which is shown in Figure 3.6(b). The devices showed linear current response to applied bias, with no rectification observed.

This implied that there was not a well defined junction, with a depletion region, forming between the materials in any case. This may be due to a number of reasons. The polycrystalline, defective nature of these films would likely result in high, and varied, levels of unintentional doping within the films. This could prevent formation of an effective depletion region, or offer alternative current pathways at grain boundaries. Similar TMDs films have previously shown very little gating response, indicating their highly defective nature can mask typical semiconductor behaviour.[118] The formation of a clear interface could also be hampered due to the rough nature of the films or alloying between the TMDs during the growth.

To further investigate this interface, a wafer with a $MoSe_2/WSe_2$ sequential stack was cleaved to allow SEM analysis of a cross section of the film to be studied. This is shown in Figure 3.6(c). Observing separate layers of the order ∼10 nm is likely below the resolution of this SEM image, but it is clear from the high level of roughness that it is unlikely two well-defined layers exist in the stack. This indicates that the film roughness is likely one of the issues when using these films in heterostructures.

3.3.1 Raman of heterostructures

Raman spectroscopy was used to gain further insight into the interface between the two TAC films. Specifically, it was used to analyse the effect of co-converting the two metal films versus sequentially converting them. This experiment was performed with MoS_2 and WS_2 as they both can be sulfurised at the same temperature. The co-converted sample had both metals deposited and converted to the corresponding TMD together, while the sequentially converted sample had the Mo deposited and converted, then the W deposited and converted. Again the same cross structure was used to give a region of MoS_2 only, WS_2 only and an interface region with both materials on top of one another. A diagram of this is shown in Figure 3.7(a).

Both sets of samples were mapped with scanning Raman spectroscopy. Figure 3.7(f) and (g) show the average spectra for the MoS_2 only, WS_2 only and interface region of the sequentially and co-converted samples, respectively. All spectra are normalised to the SiO_2 peak at ∼520 cm^{-1}. It is evident that there is a difference between the spectra of the interface regions depending on the growth method of the films, while the spectra of the MoS_2 and WS_2 regions are qualitatively similar in both cases.

To gain further insight into the differences, this data was used to form the Raman maps in Figure 3.7(b) & (c). These are the frequency position maps

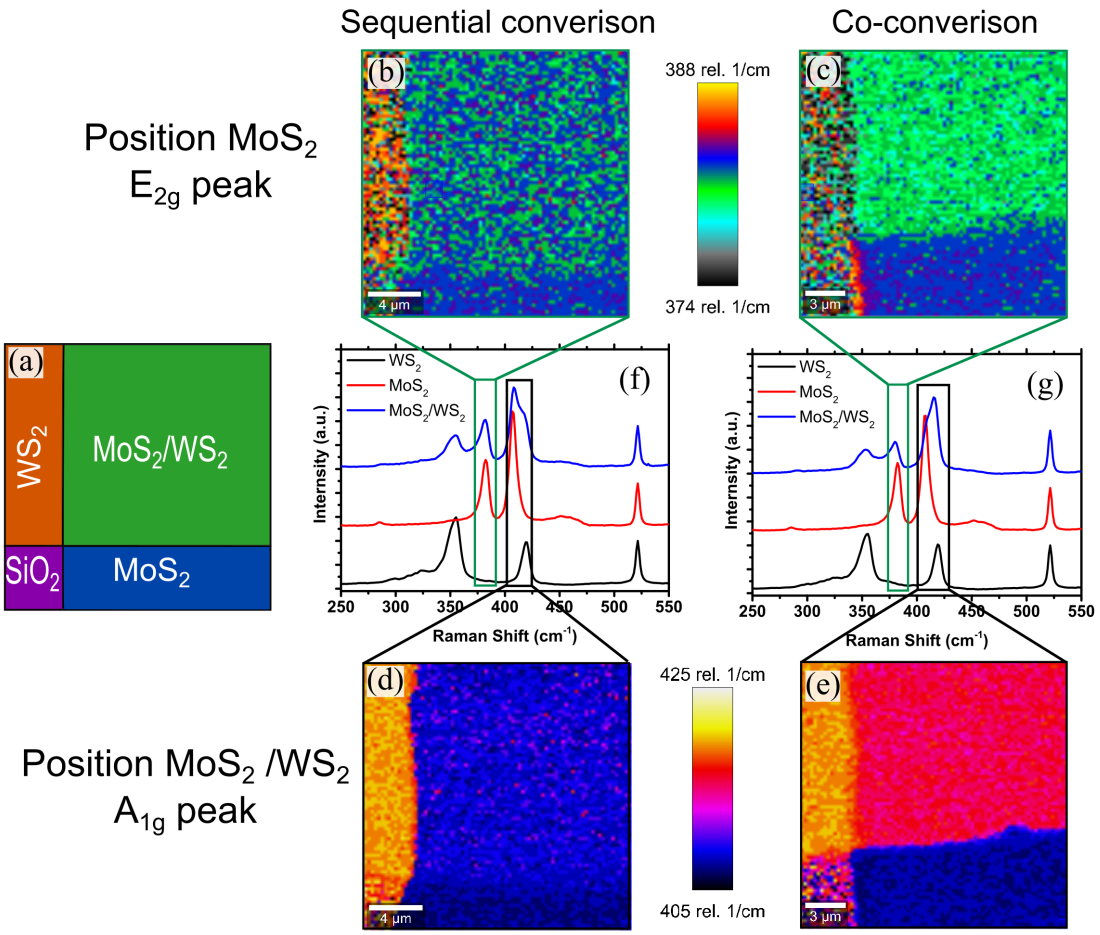


Figure 3.7: (a) Legend for Raman maps. (b) & (c) Raman map of MoS_2 E^1_{2g} peak position for sequentially and co-converted films respectively. (d) & (e) Raman map of MoS_2/WS_2 A_{1g} peak position for sequentially and co-converted films respectively. (f) Raman spectra of MoS_2, WS_2 and stack region of sequentially converted films. (g) The same spectra for a co-converted sample.

of the MoS_2 E^1_{2g} peak for films grown by sequential and co-conversion. For the MoS_2 area, this peak is centred at ~383 cm^{-1} (coloured blue) in both maps. The WS_2 and SiO_2 areas, with no peak in this frequency region, show only random noise. In the interface region, for the sequentially sulfurised sample, Figure 3.7(b), the maximum intensity is very close to the same frequency as the MoS_2 area. However, in the co-sulfurised sample Figure 3.7(c), there is a noticeable shift to a lower wavenumber, as shown by the green colour. This is a potential indication of increased alloying at the interface in the co-sulfurised sample. A similar result was seen by Dumcenco *et al.* in CVT grown crystals, where they saw increasing shift of the MoS_2 E^1_{2g} to lower wavenumber with increasing alloying with W.[192]

The A_{1g} peaks of MoS_2 and WS_2 were subsequently analysed in the same manner. The position maps of these are shown in Figure 3.7(d) & (e). These peaks are both in the same frequency region ~400-430 cm^{-1}, so to distinguish between changing peak intensities and peaks shifting frequency, they were fitted with Lorentzian peaks. What is expected in the case of alloying between the layers is that the A_{1g} peak of MoS_2 and WS_2 will both shift towards an intermediate value. This is exactly what is observed. For the sequential conversion case there is a small shift of both peaks towards each other by ~1 cm^{-1}. For the co-conversion, the peaks each shift by ~4 cm^{-1} towards each other, again indicating much more alloying in the co-conversion case.

This analysis indicates that there is potential alloying between the layers during the TAC growth of TMD heterostructures. As the level of alloying appears to differ depending on the growth method used, it implies that the diffusion of material during the growth phase may be the issue rather than the metal deposition. This issue could potentially be overcome through the use of a thin diffusion barrier between the materials or by growing the materials separately and combining them post-growth.

3.3.2 Heterostructure analysis

This section has shown that heterostructures of two TAC-grown TMD films do not readily form interfaces that possess the rectification characteristics of a heterojunction or p-n junction diode. The reason for this is the defective, polycrystalline and rough nature of the films. The high and variable defect levels, which have previously been demonstrated for TAC films, would inhibit the formation of a depletion region between the layers.[112] The film roughness, as highlighted by AFM and SEM analysis, could prevent the formation of two clearly defined layers at the junction. Finally, the alloying highlighted by the Raman analysis of the interface, would create a gradual change between the layers rather than a clear boundary where a rectifying junction could form. The combination of these leads to the conclusion that the TAC growth method is not suitable to produce heterostructure electrical devices.

Interestingly, there has been a couple of reports in literature of heterojunction diodes from similar films. Xue *et al.* produced an array of photodetectors, which displayed some rectification properties, from MoS_2/WS_2 heterostructures. These were grown from sequential sulfurisation of Mo and WO_3 films respectively, at slightly lower temperatures than used here. Woods *et al.* grew MoS_2/WS_2 heterostructures from Mo and W films by a single-step sulfurisation process. This junction showed weak heterojunction behaviour. While these reports demonstrate that TAC films can be used for electrical heterostructures under certain conditions, there has not been much further work on these systems reported in the three years since these papers were published. This may indicate that these results are difficult to reproduce due to some of the factors discussed in this chapter.

3.4 Conclusions

This chapter demonstrates the successful growth of multiple TMDs through the use of the TAC growth method. This highlights the effectiveness of this method to produce TMD films in a facile manner, while maintaining uniformity over large areas. The films were characterised using Raman spectroscopy and XPS. Both techniques corroborated the successful growth of the TMDs with only a minority of metal oxide present.

Analysis of the morphology of the films, through line profilometry, SEM and AFM, showed that after conversion the films had expanded to 2 - 3 times their initial thickness and had rough surfaces with grain sizes on the order of tens of nanometres. The electrical properties of the films were examined with all showing linear current response. The sheet resistance values indicated that WSe_2 was much lower than expected for a polycrystalline film. This indicated that it was not fully converting, leaving a metallic conductive path. This tallied with the presence of metallic W seen in the XPS analysis of these films. It also demonstrated that it is not adequate to solely rely on one characterisation technique for these materials.

Vertical heterostructures of both the sulfide and selenide TAC grown films were fabricated to evaluate their performance as heterojunction diodes. Neither of the device types demonstrated rectification properties across the junction between the two layers, indicating that no depletion layer was being formed at the interface. Raman analysis indicated that alloying between the MoS_2 and WS_2 layers was taking place, especially when the films were grown using the co-conversion process. It was deduced that the likely reason for failure of the films to form effective heterojunction diodes was due to this alloying, along with the observed roughness and high defect and unintentional doping levels of the films.

These results highlight some of the advantages that the TAC growth method offers. It enables the growth of large area films with thickness uniformity and easy

patterning. However the limitations of these films for electrical applications were also revealed. The growth method itself also presents some practical challenges. As an excess of chalcogen is vaporised during the growth, this means that, when cool, a significant amount of chalcogen will have deposited inside the furnace. This requires appropriate precautions to then be taken when opening the furnace. It would be preferable to avoid this issue, especially for tellurium where it becomes much more difficult to safely manage exposure, making this method less desirable. The following chapters will examine creating telluride TMD films using a modified TAC method that reduces some of these concerns by changing the method of chalcogen introduction.

4

Molybdenum Ditelluride

4.1 Introduction

The current frenetic pace of research into layered materials has led to a constant search for new and interesting 2D materials to investigate. As is often the case, the work on 'new' materials can be more rediscovery and adaption of older work, rather than completely new research. Fabrication of layered telluride TMDs has been described as far back as 1897, despite this, they were relatively unexplored systems prior to the explosion of interest in nanoscale TMDs in the last 10 years.[193–195]

Initially the focus was primarily on the Group VI TMDs containing sulfur or selenium, which were discussed in Chapter 3. The equivalent telluride TMDs have not been studied as extensively, despite having some very exciting properties making their further investigation worthwhile.[55,67,75,196] This may be due to telluride-containing TMDs not being naturally abundant.

Of the telluride TMDs, $MoTe_2$ is the most widely studied, especially in the last two years. In this time, there has been an increasing amount of work on $MoTe_2$, particularly crystals grown by CVT. The use of CVT grown crystals, and mechanically exfoliated flakes there of, mirrors the approach that initial research into

other 2D materials took. These methods provide a simple initial approach that nevertheless yields very high quality materials for proof-of-concept experiments. Following from this, there has been a number of works that have demonstrated growth of both phases of $MoTe_2$ by CVD,[128–130] with others achieving large-area polycrystalline film growth.[126,197] Despite this progress, the growth of large-area, monolayer films remains elusive. There are also challenges in obtaining phase-pure growth of $MoTe_2$.[23]

$MoTe_2$ has been explored for a range of applications with many focussing around it having two phases, one semiconducting and one semimetallic, which are very close in energy (35 meV per formula unit). This is interesting for applications in thermoelectrics and as a phase-change material.[23,77] Having both a semiconducting and semimetallic phase also offers the opportunity to make devices with ultra-low contact resistance by utilising $MoTe_2$ as both channel and contact material.[198] There are however a number of open challenges with $MoTe_2$ growth and application. The telluride TMDs tend to have lower stability and oxidise more readily than other TMDs, like MoS_2. This makes integrating them into devices more problematic. The synthesis can be challenging due to the low reactivity of Te with Mo and W, along with many of the tellurium precursors required for growth of $MoTe_2$ having a high toxicity.[130]

4.2 Growth of $MoTe_2$ films

The TAC growth method has many advantages but, as mention in the previous chapter, it does involves a large amount of vaporised chalcogen in the furnace system. Although this system is sealed during the growth, the chalcogen will tend to condense and redeposit inside cool zones of the furnace, leaving the potential for exposure when the furnace is opened. For sulfur furnaces, this can be quite effectively counteracted with exhaust systems and PPE, or even enclosing the entire furnace in a glove-box. However, for more toxic chalcogens such as Te, it

may be preferable to find an alternative growth method that would avoid this issue altogether.[199]

Another challenge of using the TAC growth method for telluride TMDs is the lower vapour pressure of Te compared to the other chalcogens.[200]. This makes it more difficult to achieve the chalcogen excess needed during the film conversion using remote vaporisation of Te. Along with this, as the chalcogen size increases, the transition metal-chalcogen bond strength decreases making the compound less stable. This makes telluride TMD synthesis more challenging.[201]

The growth method described here will introduce Te onto the surface of the metal film prior to conversion, thereby ensuring excess chalcogen at the reaction interface, without requiring a large amount of Te to be vaporised in the furnace. This will be achieved by using solid sources for the transition metal and the chalcogen, both of which will be deposited onto the surface prior to the furnace step. The furnace step will also be kept close to atmospheric pressure to reduce the vaporisation rate of the chalcogen from the sample.

The starting transition metal films were deposited in the same way as for sulphide and selenide TAC, by e-beam evaporation or Ar ion sputtering. A Te layer was then deposited on top by electrodeposition. Te was deposited onto the sample by using the Mo coated SiO_2/Si wafer as the working electrode in an electrochemical cell. The electrolyte was a solution of 0.02 M TeO_2 in 1 M HNO_3. TeO_2 was reduced to Te and deposited on the substrate by the reaction shown in Equation 4.1.

$$HTeO_2^+ + 3\,H^+ + 4\,e^- \longrightarrow Te + 2\,H_2O \tag{4.1}$$

The system was initially probed using CV, Figure 4.1(a), to determine the appropriate reduction potential for the reaction to proceed. It was found that a potential of -0.3 V with respect to the Ag/AgCl reference electrode allowed for efficient deposition of a Te film. It is notable that in Figure 4.1(a) the thinner

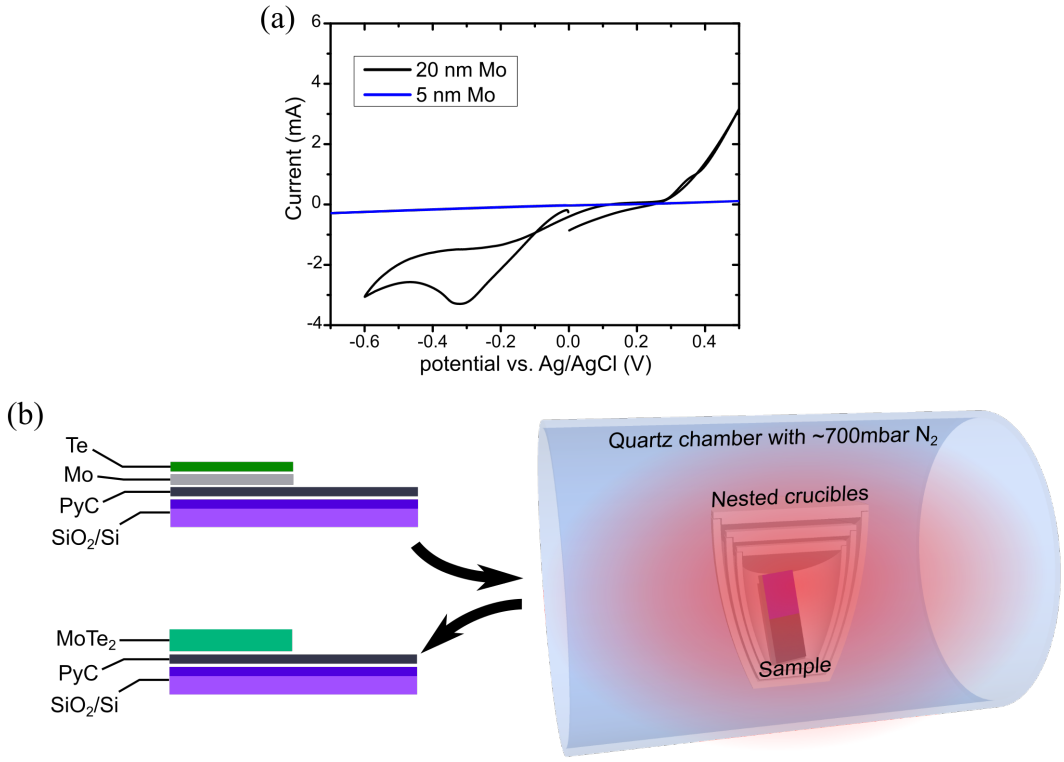


Figure 4.1: (a) CV showing the response of 20 nm and 5 nm Mo films with the TeO_2 reduction peak visible at ∼-0.3 V. (b) Schematic of the samples after deposition of PyC, Mo and Te layers. Also shown is a diagram of furnace with samples inside nested crumbles that keep the local concentration of Te elevated during the growth phase.

5 nm Mo film is quite resistive with no clear reduction peak observed. This meant that it was not possible to apply the correct overpotential for reduction due to the Ohmic loss over the length of the metal electrode. This issue was circumvented in two ways. Initially only thicker (20+ nm) films of Mo were used, to ensure reliable Te deposition. While effective, this limited some experiments and led to the development of a different solution. This was to grow a layer of PyC on the substrate prior to the deposition of the Mo film. This ∼300nm PyC layer served as an inert conductive substrate onto which Mo could be deposited. This method greatly improved the quality of the Te electrodeposition due to its increased conductivity of the sample, while also facilitating growth from much thinner (2 nm) metal films. A schematic of this sample geometry is shown in Figure 4.1(b).

A further step to improve the deposition of Te was to use pulsed electrodeposition rather than constant applied voltage. In this case, rather than apply a constant voltage at the reduction potential (-0.3 V wrt Ag/AgCl), the voltage alternated between -0.3 V applied for 10 ms and 0 V applied for 50 ms. This resulted in more uniform coverage of Te over the surface of the sample. Pulsed depositions have previously been shown to offer improved control of deposition properties, such as morphology and uniformity, by increasing nucleation density and reducing ion depletion at the electrode-solution interface.[141]

The growth of $MoTe_2$ thin-films was carried out in the way described for all Te TMD films in Section 2.2.4. The pressure was kept much higher than for other TAC growths - ∼700 mbar N_2 . This was to reduce vaporisation of Te from the sample surface before the growth of $MoTe_2$ was complete. Along with this, the samples were placed in nested crucibles, which, while not sealed, were used to keep the partial pressure of Te higher inside, further reducing the amount of Te needed for successful conversion. A growth time of 55 minutes at 450 °C was used for the majority of the films discussed in this chapter. At these experimental conditions there was consistent conversion to $MoTe_2$, however occasional residual Te was found on the surface. To ensure full conversion and no remaining Te, the growth time was increased to 90 minutes for subsequent telluride growths.

An image of a converted film in shown in Figure 4.2(a) inset. The films show good optical uniformity over the sample with the film's lateral dimensions limited only by the furnace size. This method easily allows for the fabrication of films of varying thickness, here samples that had an initial 20 nm of Mo deposited were used for characterisation. If the pre-deposited Mo layer is patterned, for example using a shadow mask, it would then be possible to obtain similarly patterned films of $MoTe_2$.

4.3 Raman spectroscopy of films

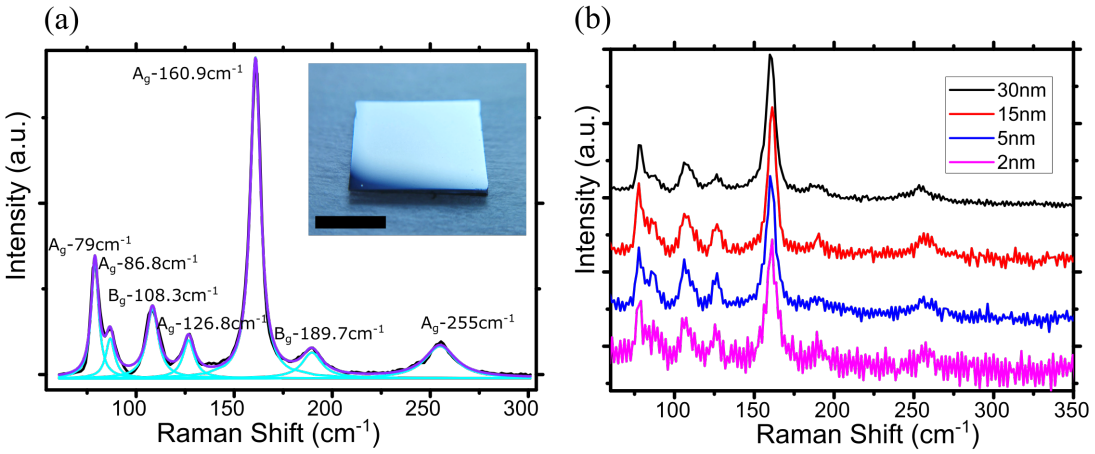


Figure 4.2: (a) Raman spectrum of a $MoTe_2$ film with 20 nm starting Mo thickness, with the symmetry and position of each mode labelled. Each of the seven peaks was fitted in Origin with a Lorentzian function (blue lines) to give the overall envelope fit of the graph (purple line). As discussed in the main text, these peak positions match well to those reported in literature for 1T' $MoTe_2$. Inset: optical image of film, scalebar is 5 mm (b)Raman spectrum of a $MoTe_2$ films with starting Mo thickness of 30, 15, 5 and 2 nm.

A typical Raman spectrum of a 20 nm $MoTe_2$ film post conversion is shown in Figure 4.2(a). Each Raman mode was fitted with Lorentzian peaks to enable accurate determination of the peak frequencies. There are seven modes visible in the spectrum with the most intense being at 160.9 cm^{-1}. 1T' $MoTe_2$ is a member of the $P2_1/m$ space group (C^2_{2h} point group), due to this low symmetry it has a large number of Raman-active modes. The peaks visible are consistent with previously-published spectra of 1T' $MoTe_2$.[53,202,203] The peaks at 79 cm^{-1}, 86.8 cm^{-1}, 126.8 cm^{-1}, 160.9 cm^{-1} and 255 cm^{-1} each have the symmetry A_g, while those at 108 cm^{-1} and 190 cm^{-1} are B_g. The peak at 160.9 cm^{-1} has been referred to as both A_g and B_g symmetry in the literature, with the earliest assignment of these symmetries I have found to be the work of Ma *et al.*[202] and Keum *et al.*[196], respectively. Taking into account the studies done by Ma *et al.* and Song *et al.*,[203] where they calculated the 1T' $MoTe_2$ peak symmetries and confirmed their predictions using polarised Raman spectroscopy, in this thesis the peak at ~161 cm^{-1} is referred to as A_g.

The Raman spectra of a series of thinner $MoTe_2$ films are shown in Figure 4.2(b). These all show similar, albeit noisier spectra, consistent with bulk-like 1T' $MoTe_2$. There is no indication of residual Te present in the Raman spectra of films obtained from the typical growth process, however, if the growth time is reduced, or the layer thickness of Te is substantially increased, both $MoTe_2$ and Te are visible in the Raman spectra.

This analysis confirms the successful conversion of the Mo metal films to 1T' phase $MoTe_2$ using this growth method.

4.4 XPS & XRD of $MoTe_2$ films

XPS analysis of the films confirmed their conversion to $MoTe_2$. Figure 4.3(a) and (b) show the fitted peaks in the Mo 3d and the Te 3d core-level regions from a typical $MoTe_2$ film. The Mo 3d core level displays a doublet associated with $MoTe_2$ at a BE of 227.7 eV and a small component from molybdenum oxide at 233.2 eV. The Te 3d core-levels associated with $MoTe_2$ and TeO_2 are at a BE of 572.2 eV and 576 eV respectively. The asymmetric shape of the components corresponding to $MoTe_2$ indicates the metallic nature of the material, further confirming that it is the 1T' phase of $MoTe_2$. The calculated stoichiometry from XPS is $MoTe_{1.8}$. While there is some level of error associated with the stoichiometry ratio from XPS, this tellurium deficiency in the material may explain the selective growth of the 1T' phase rather than 2H $MoTe_2$ discussed in Section 4.5.

Oxide components are present for both Mo and Te in the form of MoO_3 and TeO_2 as the samples were exposed to atmosphere between growth and characterisation. Of the Mo atoms, ∼13% are in an oxide, while for the Te it is 9%. TMD tellurides are known to more readily oxidised than other TMDs, especially if the films are polycrystalline.[204,205] It is likely that the oxidation process is self-limiting, as such, it is expected that analysis of the bulk would show less oxide.[206]

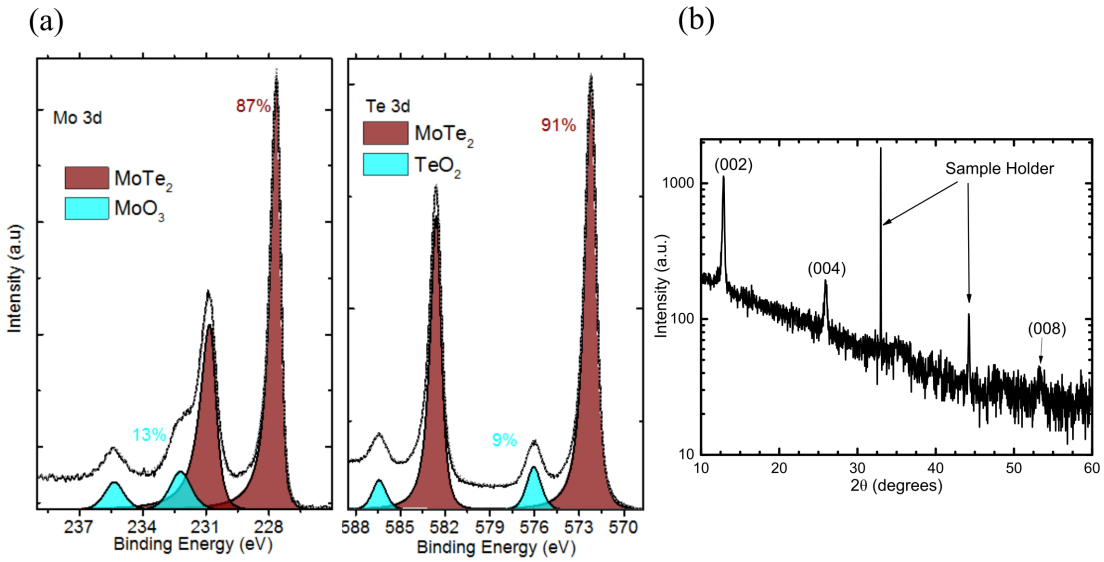


Figure 4.3: (a) Fitted XPS spectra of $MoTe_2$ showing the percentages of $MoTe_2$, MoO_3 and TeO_2 present. These peaks were charge corrected to the C 1s orbital at 284.8 eV. (b)XRD spectrum of $MoTe_2$ thin film that shows the (002), (004) and (008) peaks. The (002) peak corresponds to the distances between the layers in 1T' $MoTe_2$. The XRD spectrum is quite noisy due to the rough polycrystalline nature of the films

To further confirm the conversion of the film to 1T' $MoTe_2$, XRD was carried out with the results shown in Figure 4.3(b). In the measured XRD spectrum five peaks are visible. Two of these are associated with the sample holder, the other three correspond to the (002), (004) and (008) lattice planes of 1T' $MoTe_2$. These positions of these peaks match with previously-reported XRD of 1T' $MoTe_2$.[207] The (002) peak corresponds to the distance between the strongly bonded layers in 1T' $MoTe_2$, the so called Van der Waals gap. As the film is polycrystalline, there is a significant background and noise in the spectrum which made further analysis, such as extracting average grain size, infeasible.

4.5 Growth temperature investigation

To determine the temperature range in which $MoTe_2$ will grow using this set-up, a series of experiments were conducted in which the growth temperature for $MoTe_2$ was varied, with all other parameters kept constant. Although the binary phase

diagram for Mo and Te provides some guidance on the expected temperature range, the unique details of a growth system can result in significant departure from the phase diagram.

Figure 4.4(a) shows the Raman spectra of a number of $MoTe_2$ films grown at different temperatures between 350 °C and 750 °C. Below 450 °C there is no evidence of $MoTe_2$ and the Raman analysis reveals a spectrum identical to that of the pre-deposited Te film. This may be due to the Te not melting, as its melting point is ∼450 °C at standard pressure, which is close to the growth pressure (700 mbar) used here. Between 450°C and 650 °C there is consistent conversion to 1T' $MoTe_2$ with very similar Raman spectra. Above 650°C the film conversion was inconsistent, with a large amount of molybdenum oxides and some 1T' $MoTe_2$ signal present.[208]

The $MoTe_2$ growth at these conditions is somewhat surprising for a number of reasons. Firstly, it is at a lower temperature than has been reported by many works, only the less thermodynamically stable 1T' phase is grown and the growth only occurs up to a temperature of 650 °C. Examining the published binary phase diagram for Mo-Te, reproduced in Figure 4.4(b), it suggests the β or 1T' phase only grows above 820 °C, with the 2H phase forming below this temperature.[209] Recent work by Keum *et al.* has suggested an update to this, with mixed 2H-1T phase forming above 500 °C, Figure 4.4(c).[196] However, there is still a significant difference in this work due to the absence of 2H $MoTe_2$ growth at any temperature. The conversion temperature in this work is also lower than most reports for $MoTe_2$ growth by CVT, particularly for the 1T' phase which typically requires high temperatures for growth and a quenching cool to prevent reversion to the 2H phase.[126,129,210]

There are a number of possible reasons for the observation of low-temperature growth of exclusively the 1T' phase. The 1T' phase of $MoTe_2$ is reportedly stabilised by metallic substrates, strain and also Te vacancies, each of which

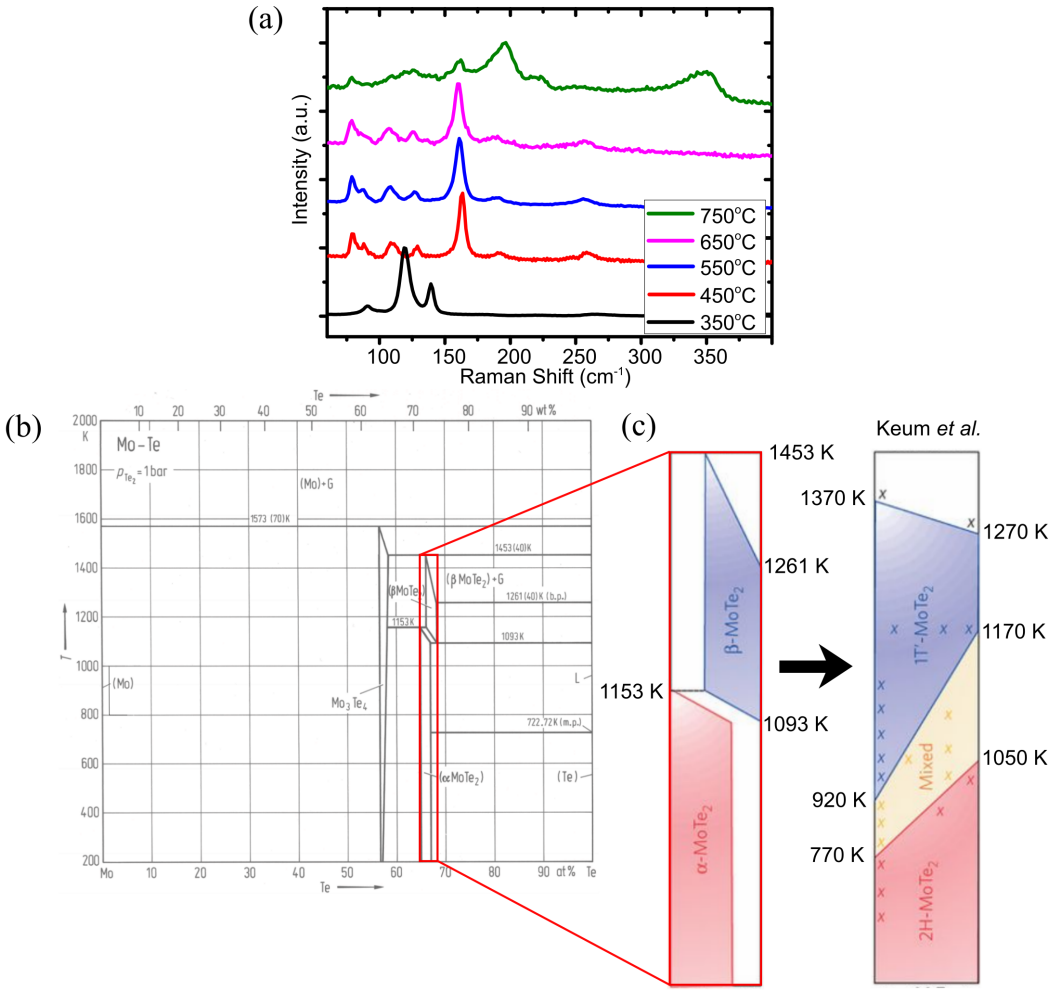


Figure 4.4: (a) Raman spectra for a number of $MoTe_2$ films grown at different temperatures. (b) Reproduction of Mo-Te binary phase diagram.[209] (c) The region of interest for $MoTe_2$, along with the updated version of this region of the phase diagram by Keum *et al.*[196]

may be present here.[23,126,198] The films are grown from Mo metal into which Te diffuses, this may have resulted in a strained film and could also explain the growth of $MoTe_2$ crystals at a high angle to the substrate. As the films are polycrystalline in nature, a large number of Te vacancies could be expected that again would stabilise the 1T' phase. A number of works have also reported the initial growth of 1T' $MoTe_2$, followed conversion to the 2H phase at longer growth times.[134,211] Finally, it has been reported recently, on similar systems, that the phase of $MoTe_2$ grown is very sensitive to the rate of Te introduction, with too rapid or too low rates leading to formation of the 1T' phase.[135] This parameter

is difficult to control in this set-up making this assertion hard to verify but it is consistent with the observed results. As such this is considered the likely reason for the observed 1T' phase growth.

A potential reason for the absence of growth above 650 °C is that the Te vaporises too rapidly, leaving insufficient residence time for efficient conversion to $MoTe_2$, or Te may be lost from initially reacted material. It has been reported that at temperatures of above 500 °C, in vacuum or Te deficient atmospheres, there is a tendency for $MoTe_2$ and WTe_2 to decompose due to loss of Te.[211–214] This of course would not be an issue in sealed ampoule systems, as used in CVT, as the atmosphere would have a high concentration of Te consistently throughout the growth.

This growth method is quite different from traditional CVD and TAC growth methods, as it does not involve any vapour phase reaction. However, the growth conditions observed highlight the significant difference between growth close to thermodynamic equilibrium, such as CVT, and this approach.

4.6 Stability of films

The stability of the $MoTe_2$ films was already discussed briefly in Section 4.4, however here it will be examined it in a broader context, while also attempting to provide some clarity on conflicting reports in literature. The surface of the $MoTe_2$ films were shown to be oxidised to a level of ∼10%, with the primary oxide components being TeO_2 and MoO_3. This correlates with other studies in literature that found $MoTe_2$ oxidises over a period of time, when exposed to atmosphere.[215,216] In particular, O_2 and H_2O were found to interact strongly with vacancies in the material.[204,217] It appears that the oxidation is confined primarily to the surface, as samples still display strong $MoTe_2$ Raman signal months after growth. It will be shown in Chapter 5 that the oxidation of WTe_2 is self limiting and this is likely to be the case here also.[206]

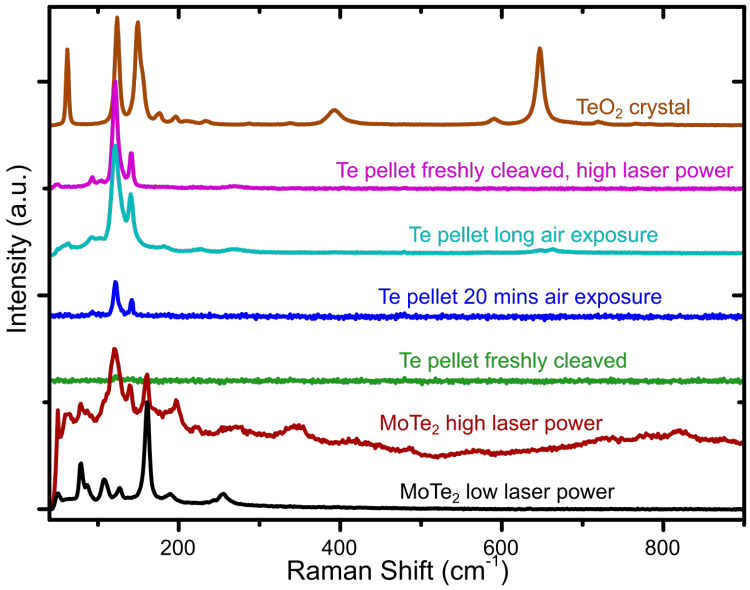


Figure 4.5: Raman spectra of a number of materials in different conditions. From bottom: $MoTe_2$ measured with usual laser power; $MoTe_2$ measured with high laser intensity; freshly cleaved Te pellet; Te pellet exposed to atmosphere for 20 minutes; Te pellet exposed to air for a number of months; freshly cleaved Te pellet measured with high laser power; TeO_2 crystal.

Shown in Figure 4.5 is the Raman spectrum of a typical 1T' $MoTe_2$ film along with the spectrum of the same film measured at a higher laser intensity. The spectrum measured at higher laser intensity has a number of small peaks which can be assigned to molybdenum oxides and two new intense peaks at $\sim$122 cm^{-1} and $\sim$140 cm^{-1}.[208] These two peaks were also seen after the laser irradiation of 2H $MoTe_2$ in the work of Tan *et al.*[218] They assigned these peaks as evidence of a phase change from 2H to 1T' $MoTe_2$. It will be demonstrated below how this assignment is incorrect, and, rather than indicating the changing phase of $MoTe_2$, they are simply indicating its decomposition.

Figure 4.5, also shows four Raman spectra taken from a Te pellet. When the surface is freshly cleaved there is essentially no Raman signal. With increasing exposure time to air, there are a number of peaks which form, the two primary ones being at $\sim$122 cm^{-1} and $\sim$140 cm^{-1}. Similar peaks are formed if a freshly cleaved area is exposed to a high laser intensity. These are the same two Raman

peaks which are formed by exposing $MoTe_2$ to a high laser power, clearly demonstrating that they cannot be evidence of the presence of any phase of $MoTe_2$ as claimed by Tan *et al.*

Assigning these peaks at ∼122 cm^{-1} and ∼140 cm^{-1} to TeO_2 would make sense based on the experimental evidence here - XPS confirmed the presence of TeO_2 on the films and as the Te pellet is exposed to air, these peaks appear. However, when crystals of TeO_2 were examined by Raman spectroscopy the spectra were somewhat different, as can be seen in Figure 4.5. As TeO_2 has a number of phases, each with quite complex Raman spectra, it can be difficult to be sure of peak assignments, however the peaks at ∼122 cm^{-1} and ∼140cm^{-1} do not match very well to any published TeO_2 spectra.[219–221]

There are a number of papers which assign these peaks as the A_1 and E_{TO} modes of crystalline tellurium.[222–225] The work of Pine *et al.* also provides a possible explanation as to why the modes seem to appear when the Te crystal is exposed to high laser intensities.[223] They measured the spectra of amorphous Te and found it to be 100 times more intense than crystalline Te, and this amorphisation was achieved by exposing crystalline Te to high laser intensities. The similarity to observed results here leads to the conclusion that the freshly cleaved Te is crystalline and therefore only has a weak Raman signal. However as the Te is exposed to atmosphere, or high laser power, it become more amorphous resulting in a much more intense Raman signal. While not possible to definitively confirm this, the peaks at ∼122 cm^{-1} and ∼140 cm^{-1} will be referred to as Te peaks in the remainder of this thesis.

4.7 Film morphology

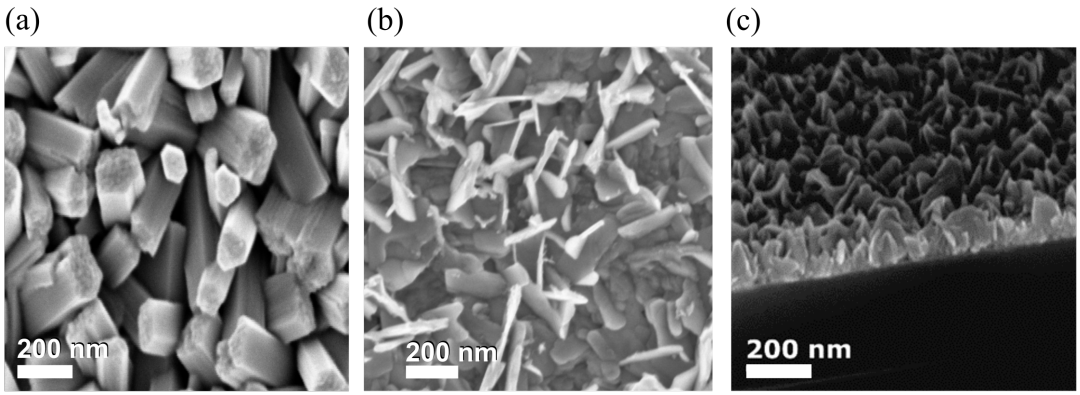


Figure 4.6: (a) SEM image of the deposited Te prior to conversion to $MoTe_2$. (b) SEM of 20 nm $MoTe_2$ film showing the rough, flake-like nature of the films. (c) SEM image of a cleaved SiO_2/Si wafer with $MoTe_2$ growth on top. This gives a good representation of the vertical alignment of the crystal growth.

4.7.1 SEM & AFM

The morphology of the $MoTe_2$ films was analysed using electron and atomic force microscopies. In Figure 4.6(a) an SEM image of the hexagonal rod-like morphology seen in the electrodeposited Te prior to conversion is presented. Figure 4.6(b) shows the flake-like morphology of the $MoTe_2$ film after conversion. The converted $MoTe_2$ film's crystal sizes are on the order of hundreds of nanometres with many protruding at a high angle to the surface. This is further demonstrated by the 'cross-section' view of a cleaved silicon wafer and $MoTe_2$ film in Figure 4.6(c). The vertical nature of the flakes is similar to the previously-reported edge-growth of MoS_2 films, though in this case the crystals are less aligned.[119]

The initial thickness of Mo was varied to examine the changes this caused to the morphology of the $MoTe_2$ films. Figure 4.7 (a)-(c) show SEM images of films grown from Mo of 50, 15 and 2 nm respectively. For the 2nm films there are interspersed, discrete $MoTe_2$ flakes, while the thicker films have larger flakes which cover the surface. The increased flake size for thicker films is related to increased reactant amounts present, and will be discussed fully in Section 5.8.

To examine the morphology changes in more detail, AFM was carried out on

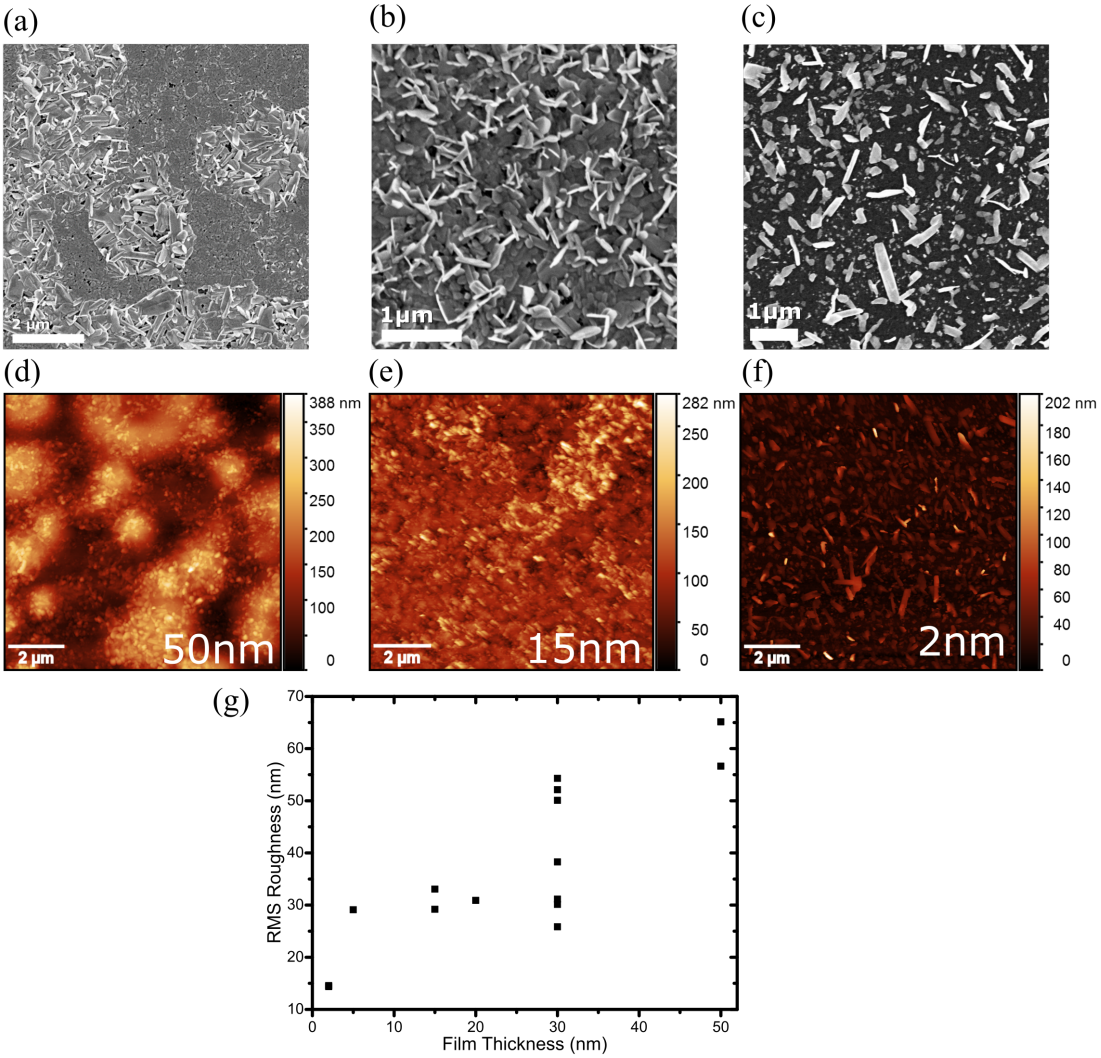


Figure 4.7: (a) - (c) SEM images of $MoTe_2$ films of 50, 15 and 2 nm respectively. All grown on PyC on SiO_2/Si, (d) - (f) AFM images of the same films (g) Plotted RMS roughness vs film thickness for a number of $MoTe_2$ films.

the same films and is shown in Figure 4.7(d)-(f). To quantify the differences seen in SEM and AFM, the RMS roughness of a number of film was extracted from AFM measurements. It was found that the roughness of the films increases with increasing thickness, Figure 4.7(g). As an aside, it can be seen that the surface of the 50 nm films has areas of larger and smaller flakes, this will be discussed further in relation to WTe_2 in Chapter 5.

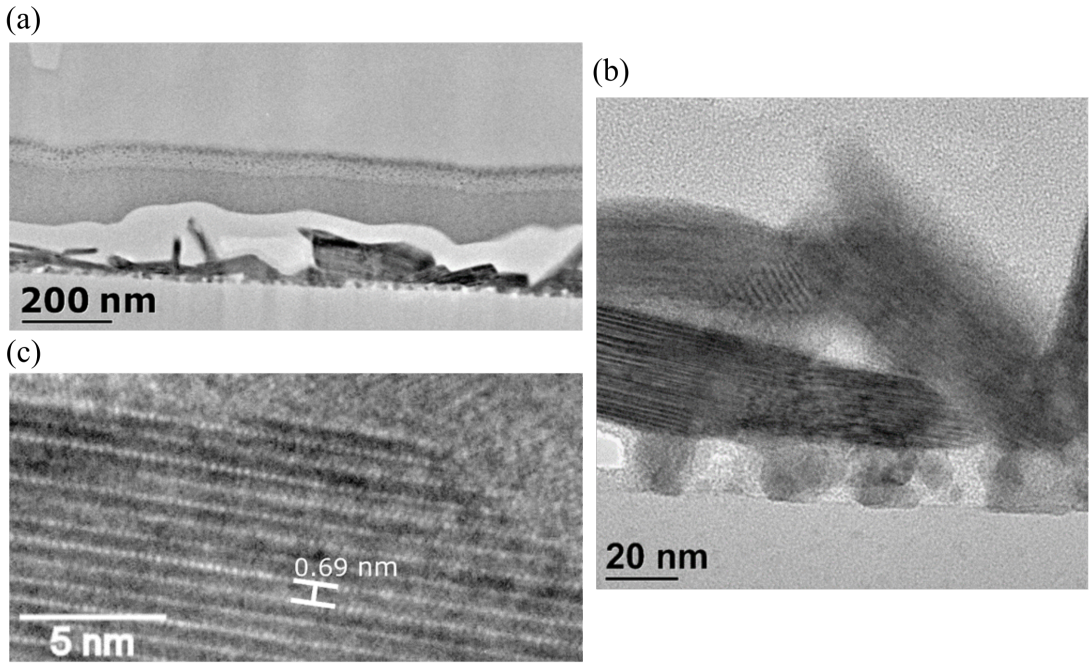


Figure 4.8: (a) & (b) TEM cross section of $MoTe_2$ film. The crystalline flakes are visible along with the amorphous sub-layer (c) TEM image of a crystal showing the layer separation of the $MoTe_2$

4.7.2 Cross-sectional TEM analysis

Additional analysis of the film morphologies and growth mechanism was obtained by preparing thinned lamellae of the $MoTe_2$ films for cross-sectional TEM. The obtained TEM images, shown in Figure 4.8 (a) and (b), again highlight the randomly-aligned nature of the domains in the film, along with the rough nature of the film surface. The TEM shows that the flakes are crystalline and protrude at a high angle to the surface. It is evident that below the crystalline $MoTe_2$ flakes there is an amorphous layer 15-20 nm thick with some voids present. Notably this layer is of a similar thickness to the initial Mo layer deposited (20 nm). When probed with EDX it was found that this amorphous layer contained both Mo and Te. Examining the layers within a crystal, Figure 4.8(c) shows an average separation of 0.69 nm, consistent with the expected layer separation of $MoTe_2$ of 0.7 nm.[207]

4.7.3 Growth mechanism

The analysis of the growth temperature range, along with the morphology of the films allows some insights into the growth mechanism of these films to be obtained. While the method used to grow the $MoTe_2$ films here can be considered an extension of previous works on the TAC of metallic films to TMDs, the nature of the reaction interface in this case is quite different. The majority of TAC works to date refer to solid films that are converted through exposure to vapour-phase chalcogens.[108,109,226] In this work, the reaction is occurring at a solid-liquid interface, which results in a much higher chalcogen concentration at the interface. This is expected to be a large part of the reason for the quite different morphology - much larger crystal sizes and more the out-of-plane nature of these crystals.

The proposed growth mechanism is that upon heating the Te begins to melt and form an intermixed layer with Mo. As the concentration of Mo in this layer increases, $MoTe_2$ crystals begin to nucleate and grow, Figure 4.9, in a manner analogous to the solution-liquid-solid growth mechanism.[227] By examining the results from the TEM, discussed in Section 4.7.2, it is clear that rather than the Mo film being converted, crystals of $MoTe_2$ nucleate from the intermixed region and then grow from this. This results in the formation of two distinct layers- the crystalline $MoTe_2$ flakes and an amorphous layer of $MoTe_x$ below this. The growth mechanism for this system will be discussed further in regard to the growth of WTe_2 in Chapter 5

4.8 Application as an electrocatalyst

TMDs have been shown to have strong electrocatalytic behaviour and the $MoTe_2$ films grown here possess many promising characteristics in this regard.[144] As they are in the 1T' phase, they have high conductivity, which facilitates improved charge transport to the active sites.[228,229] Furthermore, it has been suggested

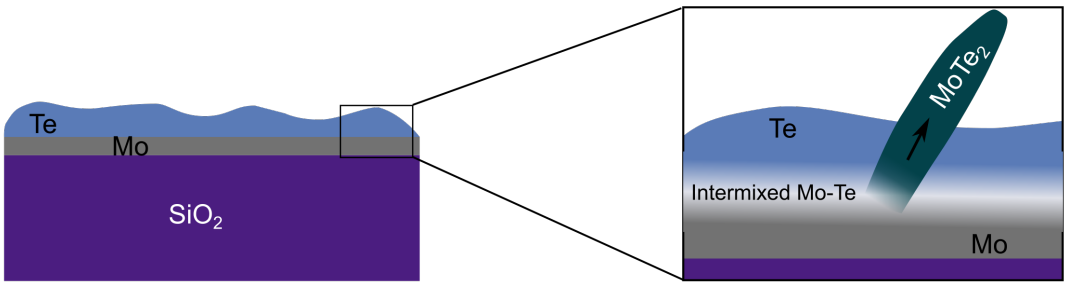


Figure 4.9: Schematic of the proposed growth mechanism for the $MoTe_2$ thin films

for other TMDs, such as MoS_2, that in the 1T phase the basal plane becomes catalytically active.[145] Finally, due to these films' polycrystalline nature and vertically oriented flakes, it is expected that there is a high percentage of undercoordinated and edge sites, both of which have been shown to improve catalytic behaviour.[119,146,147] To investigate the applicability of these films, in electrocatalytic applications, their performance as a catalyst for the HER was examined. In this case, $MoTe_2$ was grown on PyC which provides an ideal inert, conductive current collector due to its low reactivity and stability at high temperatures. This system of films on PyC has previously been used for the characterisation of other TMDs such as MoS_2.[230,231]

The catalytic performance of the $MoTe_2$ samples for the HER was measured in a three-electrode cell with 0.5 M H_2SO_4 as the electrolyte. A graphite counter electrode and a Ag/AgCl reference electrode were used. Additional experimental details are provided in Section 2.3.9. The activities of the various $MoTe_2$ films are investigated by measuring LSVs in this cell. The current density measured is proportional to the hydrogen evolved, with higher current at lower applied voltage (OP) indicative of more effective catalytic behaviour.

The results of the LSV for representative films of different thickness can be seen in Figure 4.10(a). From this it is possible to extract the onset potential of the different films, defined here as the OP required to measure a current density of 0.5 mA cm^{-2}. It is evident that the thickness of the films has a strong influence on

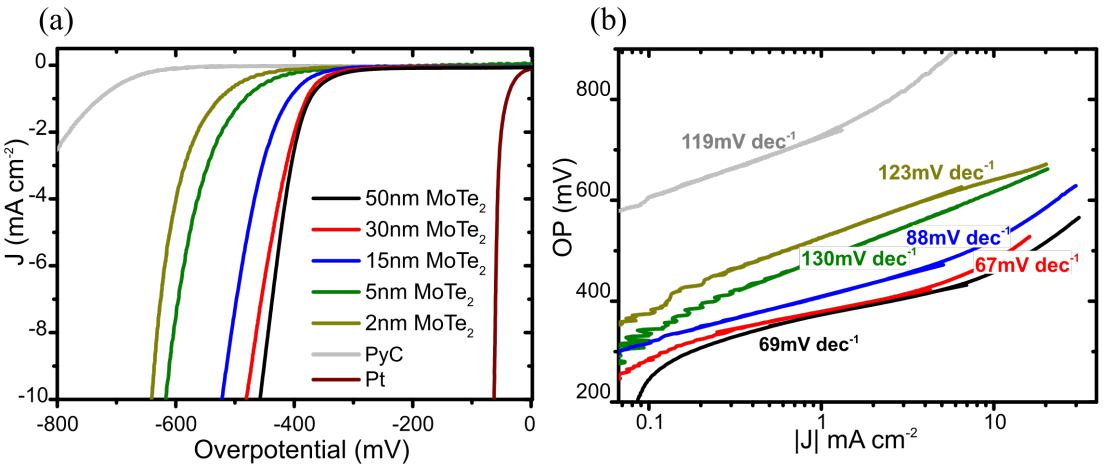


Figure 4.10: (a) LSV of $MoTe_2$ films of different thickness. All thicknesses refer to the starting Mo layer thickness. Also shown is the response of bare PyC and a 30 nm Pt film. (b) Corresponding Tafel plots, with fitted slopes, of the same samples.

their effectiveness as catalysts for the HER, with the thicker films demonstrating markedly-better behaviour. The best performing of the films examined here is the 50 nm $MoTe_2$ film, which has an onset potential of -349 mV. The thinnest 2 nm films have onset potentials of ∼-500 mV.

By plotting the log of the current density versus the OP, the Tafel plot is obtained, as shown in Figure 4(b). Taking the slope of the linear region gives the Tafel slope, which is related to the kinetics of the reaction steps involved in the evolution of hydrogen. For applications, such as HER, it is generally accepted that a lower Tafel slope is desirable as it can be understood to be the voltage increase required to increase the current density, and so hydrogen produced, by one order of magnitude.

Tafel slope values for each film are shown in Figure 4.10(b). The 30 nm and 50 nm films give the best performance by this metric with values below 70 mV dec^{-1}. These comparatively low values indicate that after the onset potential, the current increases quite quickly, leading to more competitive behaviour at higher voltages. The thinner 2 nm and 5 nm films, have much higher Tafel slopes, on the order of 120 mV dec^{-1}, indicating that it is likely the Volmer reaction step that

Table 4.1: Details of the electrocatalytic properties of $MoTe_2$ films from published literature

Reference	Tafel mV dec^{-1}	OP @ 10 mA cm^{-2}	Note
Seok *et al.*[233]	127	-0.356 V	Single crystal, area 10^{-3} cm^2
McGlynn *et al.*[81]	78	-0.34 V	Grown film, area 0.071 cm^2
Gholamvand *et al.*[80]	∼100	∼-0.44 V	Liquid exfoliated sheets
Kosmala *et al.*[232]	∼100	-0.53 V	No area given
This work	67	-0.48 V	area ∼1 cm^2

is rate limiting in these. In Figure 4.10(a) and (b), the response of a bare PyC film can also be seen, clearly this would have a negligible effect on any of the measurements due to its very low electrocatalytic activity in the measurement window.

The performance of the 1T' $MoTe_2$ films is not competitive with state-of-the-art Pt catalysts (a 30 nm film of Pt on PyC measured here has an onset potential of close to 30 mV) but it is similar to the values for other relatively large-area $MoTe_2$ electrodes reported in the literature.[81,232] A common metric used to compare different electrodes in literature is the OP required to measure 10 mA cm^{-2} (OP @ 10 mA cm^{-2}) of current density. For this reason the following section will use this metric rather than the previously defined onset potential to compare the films produced here to others reported in literature. A table of results from other published works on $MoTe_2$ are shown in Table 4.1.

The OP @ 10 mA cm^{-2} is higher than some reported works, however the Tafel slopes displayed by these films compare very favourably with other works. Films of liquid-exfoliated flakes have shown Tafel slopes of ∼100 mV dec^{-1}.[80] Seok *et al.* examined single crystals of 1T' $MoTe_2$, while McGlynn *et al.* looked at ink-jet deposited $MoTe_2$ films, these reports showed Tafel slopes of 127 and 78 mV dec^{-1} respectively.[81,233] Furthermore, both of these were smaller scale electrodes and

unlike this work were not grown directly on the current collector. This system of TMD on PyC offers a cheaper, more scalable alternative to platinum-group catalysts.

It is evident from Figure 4.10(a) that the thickness of the films has a strong influence on their effectiveness as catalysts for HER. Further insight into this behaviour can be gleaned by examining the morphologies of the films. As seen in Section 4.7.1, from both SEM and AFM, there are the noticeable differences between the films of different thicknesses, with thicker films having increased roughness. The extracted roughness was plotted against the respective onset potential (OP needed to measure 0.5 mA cm^{-2}) of each film, Figure 4.11(a). There is a clear trend that initially the onset potential drops quickly as roughness increases, while above ∼35 nm the onset potential changes much more slowly. It is expected that the decrease in onset potential correlates with roughness because a higher roughness indicates a more porous surface. This gives a greater effective surface area, and so, more active sites for the reaction to proceed. This increased porosity also offers improved access to the available active sites along with a reduction in mass transport limitations.

Not all surface information is captured by the roughness however, as the films change morphology it could also be expected that there is change in the type of surface sites exposed e.g. varying density of defects, edge sites or basal plane due to the changing crystal sizes and orientation. It is suggested that this is what is causing the rate at which the onset potential changes with roughness to vary over the measurement window. Further experiments, examining the type and density of active sites would be needed to confirm this. As is, it has been found that electrocatalytic behaviour improves with increasing thickness of the $MoTe_2$ films up to a roughness of ∼35 nm, correlating to films with an initial starting Mo thickness of 20 - 30 nm. Increasing thickness beyond this does not show significant improvements in performance.

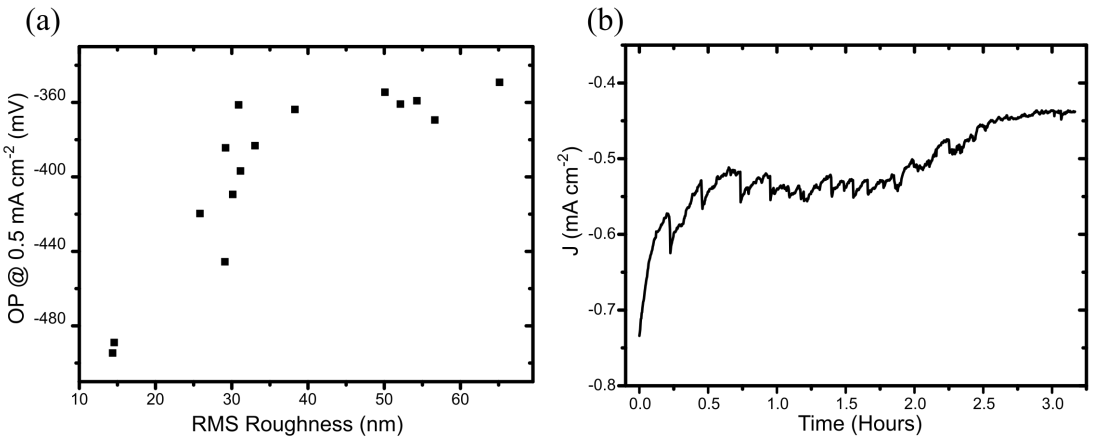


Figure 4.11: (a) Plot of the onset potential (OP required to measure 0.5 mA cm^{-2} of current density) versus the RMS roughness of the films. The onset potential drops noticeably before changing much more slowly with roughness above ∼35 nm. (b) Chronoamperometry of 30 nm $MoTe_2$ sample on PyC showing the measured current density as a function of time for a fixed applied potential of -0.6V with respect to the Ag/AgCl reference electrode.

The stability of these films in the electrochemical set-up was examined using chronoamperometry. A constant voltage of -0.6 V, with respect to the Ag/AgCl reference electrode, was applied to a sample and the current measured over a period of 190 minutes. The results are shown in Figure 4.11(b). The film showed a 40% drop in current density over the applied time period which may be due to mechanical damage caused to the electrode by H_2 bubble formation.[230]

4.9 Conclusion

In this chapter an efficient way to produce large-area thin films of 1T' $MoTe_2$ by conversion of pre-deposited Mo, and electrodeposited Te films has been demonstrated. This method is an adaption of the previously discussed TAC growth method in which both the Mo and Te are deposited onto the substrate prior to reaction in an inert atmosphere furnace. The deposition of the Te by electrodeposition affords a high level of precision in local reactant concentration and so avoids potential issues with vaporising large amounts of chalcogen. This method is not specific to $MoTe_2$ and has the potential to produce numerous different

TMD films in a reliable and scalable manner.

The films produced were phase pure with only the 1T' phase being observed. The growth of 1T' $MoTe_2$ was successful at temperatures as low as 450°C and comparatively short dwell times, which is of particular interest given the high temperatures required in other synthesis routes. This lowers the thermal budget of the synthesis and would allow the use of substrates such as aluminium, glass and polyimide. Furthermore it allows for potential back-end-of-line integration with silicon-based chips which is limited to 450°C. Interestingly the growth was not successful above 650 °C, in contrast to what would be expected from analysis of the Mo-Te binary phase diagram. This is thought to be due to the vaporisation of Te prior to conversion, or loss of Te from already converted films.

The polycrystalline films were characterized with Raman spectroscopy, XRD and XPS, with all indicating the presence of phase pure 1T' $MoTe_2$. XPS indicated that the surface was oxidised to ∼10% with the primary oxide components being MoO_3 and TeO_2. The morphology was further examined with SEM, TEM and AFM giving a clear picture of the films which differ significantly from material grown by TAC. These have much larger crystallite sizes that grow at a high angle to the surface resulting in rough films.

Application of the films as catalysts for the HER produced promising results with some films having Tafel slopes of below 70 mV dec^{-1}, comparing well with previously reported literature. Additionally, it was found that thicker films have increasingly competitive behaviour due to increased roughness. While not challenging the performance of Pt-based catalysts, they show encouraging HER results and due to their nature, offer inherent scalability. This scalability is a valuable characteristic not encompassed by typical metrics such as the current density.

This work appears to indicate that there is a wide range of Mo to Te ratios under which the $MoTe_2$ films will grow, however it does ignore the issue of how

completely the films are converting. It is clear from Raman that $MoTe_2$ is forming and from XPS that there is no residual Te or Mo on the surface but the cross sectional TEM showed that there is an amorphous layer below the surface. EDX appeared to show that there was Te in this layer but it is unknown whether this layer would reduce if there was more Te present or a longer growth time implemented. Further examination with techniques such as cross-sectional TEM would be needed to understand this more fully.

5

Tungsten Ditelluride

5.1 Introduction

WTe_2 is another telluride TMD that has recently generated a large amount of interest. As such, it is natural material to investigate to demonstrate the flexibility of this growth method.

While it is difficult to determine exactly when WTe_2 was first isolated, there are references to it as a known material in the 1920's, when the structure was reported as being the same as MoS_2.[195] This was corrected to the current distorted octahedral structure by further analysis completed in the 1950's and 1960's.[57,234] There are a number of papers from this time that investigate the structure and electrical properties of bulk WTe_2, with particular emphasis on its thermoelectric properties.[76,235–237] It is only in the last 5 years however that interest in WTe_2 on the nanoscale has dramatically taken off.

Of the Group VI TMDs studied thus far, WTe_2 is unique in that its most stable polytype is the distorted octahedral, T_d phase. This phase of TMD is of interest due to its unique electronic properties and the prediction that it could support topological electronic states.[71] Experimental results demonstrating large, non-saturating magnetoresistance and high mobilities of up to 10,000 $cm^2V^{-1}s^{-1}$

in WTe_2 have further increased interest.[73,238] WTe_2 was also the first material to be suggested as a potential type-II Weyl semimetal.[239] Since this prediction, there have been a number of experimental works that have lent credence to this assertion.[68,69,240] There have also been a number of works examining WTe_2 for other applications such as for nanoscale electrical interconnects[66], nanoribbons for electrocatalysis[82] and as an anode material for Na-ion batteries.[85]

The majority of these works have focussed on mechanically-exfoliated flakes. These have a number of draw backs, such as a lack of scalability, as detailed in Section 1.2.1. There has been some work on the bottom-up growth of nanoscale WTe_2, however large-area, reproducible synthesis remains an open challenge.[127,131] There has recently been an increase in works published on the growth of WTe_2 by various methods, but this field is far from mature and leaves a pressing need for further work on straight-forward scalable growth processes, something which this chapter will attempt to address.

5.2 Growth of WTe_2 films

The WTe_2 described throughout this chapter was grown in a manner similar to the $MoTe_2$ discussed in Chapter 4. A film of W was deposited using Ar-ion sputtering, followed by the electrodeposition of Te onto this layer. This electrodeposition was carried out by reducing TeO_2 in solution to Te, at a certain potential with respect to a Ag/AgCl reference electrode. This potential was determined experimentally using CV. A typical voltammogram for a 40 nm W film on PyC is shown in Figure 5.1. The potential is repeatedly cycled from -0.7 V to 0.7 V and back, with the current response measured. There is a clear peak signifying the reduction of TeO_2 to Te at $\sim$-0.2 V. This peak shifts towards more positive values with subsequent cycles, due to there being Te crystals already nucleated on the surface. Analysis of the CV led to a potential of -0.15 V being used for the Te depositions in this case.

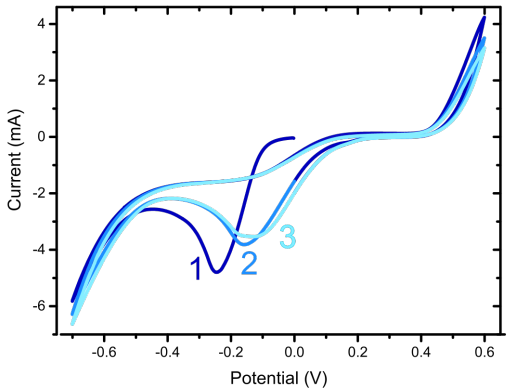


Figure 5.1: CV showing the reduction peak of TeO_2 to Te on W at ∼-0.2 V with respect to Ag/AgCl. Three consecutive sweeps are shown with the first being the darkest blue and final being the lightest.

The layers of W and Te were then reacted to form WTe_2, in nested crucibles, in a quartz furnace. The reaction was carried out under a 2 slm flow of N_2, with a pressure of ∼700 mbar, at a growth temperature of 550 °C. This temperature, and a growth time of 90 minutes, was used to ensure full conversion of all thickness films and evaporation of any remaining Te. The furnace was then cooled to below 30 °C before removing the samples. All samples are named based on their starting W thickness, as measured by the deposition tool QCM. The samples were grown on SiO_2/Si wafer with a layer of PyC, unless otherwise specified.

5.3 Raman spectroscopy of films

Bulk WTe_2 consists of Te atoms arranged in a distorted octahedral configuration around a central W atom, leading to point group C_{2v}^7 symmetry. The unit cell contains 12 atoms, with both of these factors resulting in a large number of Raman active modes.[241] A typical Raman spectrum of a 20 nm film of WTe_2, grown at 550 °C, is shown in Figure 5.2(a). This spectra closely matches previously published spectra of bulk-like WTe_2, indicating the successful growth of T_d phase WTe_2 using this method.[202,242] As there are a number of overlapping peaks in the spectrum, the peaks were fitted with Lorentzian curves to determine exact peak

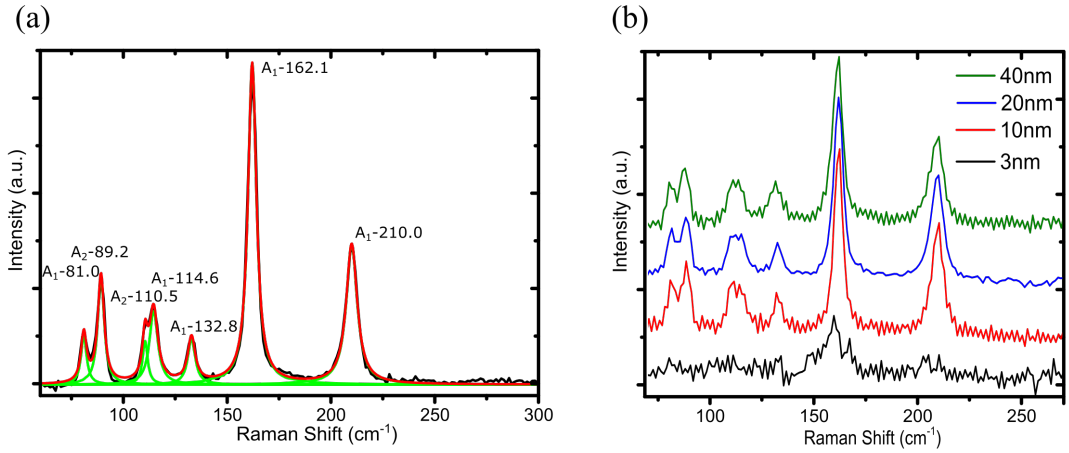


Figure 5.2: (a) Typical Raman spectrum of 20 nm WTe_2 with modes fitted with Lorentzian peaks. (b) Raman spectra of WTe_2 films with differing starting W thickness.

positions.

WTe_2 has a large number of possible Raman peaks, the position and intensity of which can be influenced by a number of factors, such as doping, strain and thickness.[242–244] The films grown here contain predominantly randomly aligned WTe_2 crystals, making assigning symmetries based on the experimental work alone not possible. For this reason, the peaks symmetries are assigned based on matching the positions and intensities to previously published works. Even so, it can be challenging to definitively assign certain peaks due the large number of modes possible in WTe_2, some of which are only separated by a few wavenumbers.[51,202] Consequently, the symmetries given here cannot be considered definitive. The peaks at 81.0 cm^{-1}, 89.2 cm^{-1}, 114.6 cm^{-1}, 132.8 cm^{-1}, 162.1 cm^{-1} and 210.0 cm^{-1} are assigned the symmetry A_1, while the peak at 110.5 cm^{-1} is A_2. While the positions remained consistent, there was found to be variations in the relative peak intensities within the films, this will be discussed further in relation to transferred flakes in Section 5.10.3.

Examining the Raman spectra of films of different thickness, Figure 5.2(b), shows the Raman signal is consistent between the various films, with only the 3 nm film showing a much noisier spectrum having only the peak at ∼162 cm^{-1}

readily discernible. It should also be mentioned that in a similar way to $MoTe_2$, WTe_2 was found to be sensitive to laser power and decomposed to form oxides if exposed to high laser intensities (∼1 mW) during Raman measurements. This made obtaining spectra with high signal-to-noise ratios challenging.

5.4 XRD of WTe_2

XRD further confirmed the conversion of the W film to WTe_2. XRD results are shown in Figure 5.3. The spectrum measured is consistent with previously reported XRD of WTe_2 with the (002), (004), (006) and (008) peaks being most prominent.[57,245] As the film is polycrystalline there is a significant background and noise in the spectrum which made further analysis, such as extracting average grain size, infeasible. The most intense WTe_2 peak in the spectrum is the (002), suggesting that this is the predominant orientation of the crystals in the film, something which will be examined further in Section 5.10.4.

5.5 XPS of WTe_2

XPS analysis allowed more quantitative information on the composition of the WTe_2 films to be obtained. These results are shown in Figure 5.4. Initial discussions will focus solely on the as grown sample, shown in the top panels of (a) and (b). Shown in the left panel is the W 4f core-level region, however the W 5p and Te 4d core levels are at similar energies, making the fitting more complicated in this case. The analysis here will only focus on the W 4f core levels, as these are the most intense.

As with $MoTe_2$, there are two doublets present for the W 4f core level, one associated with WTe_2 and the other with WO_3. Of the W atoms, 30% are in the form of WO_3, with the remaining 70% in WTe_2. Similarly in the top panel of Figure 5.4(b), there are two doublets associated with the Te 3d core level,

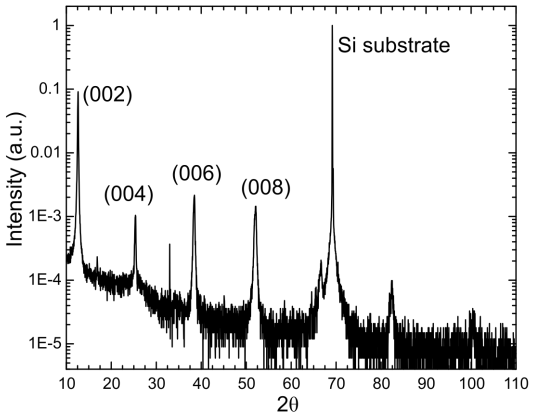


Figure 5.3: XRD of WTe_2 film with prominent peaks labelled. Similar to $MoTe_2$ the (002) peak corresponds to the Van der Waals gap between the WTe_2 sheets.

one corresponding to Te bound to W in WTe_2 and the other for Te in the form of oxides. The Te on the surface is predominantly in the form of WTe_2, with only 8% of the atoms bound to oxygen. The stoichiometry of the WTe_2 on the surface was found to be $WTe_{1.8}$, indicating a slight deficiency in Te, similar to the $MoTe_2$ film examined. Finally, the asymmetric nature of the peaks indicates the (semi-)metallic nature of the sample.

The level of oxidation observed on the surface of the WTe_2 film implies that it is prone to degradation in atmosphere, more so than $MoTe_2$. This susceptibility of WTe_2 to oxidation has previously been reported in a number of works.[131,206,246] These have concluded that the oxidation of the first few atomic layers of WTe_2 is extremely rapid, however the oxidation is self-limiting and tends not to extend far into the bulk. To investigate this, sputter XPS analysis was carried out on the sample.

The sputter XPS process is described in Section 2.3.2. Briefly, it involves XPS being measured on the sample as usual, following this Ar ion sputtering is used to remove a certain amount of material from the sample surface. XPS is then carried out again and the process repeated as many times as desired. As the whole process takes place without breaking vacuum, it offers the opportunity to measure XPS of the bulk of the material. In this case two rounds of 30 seconds

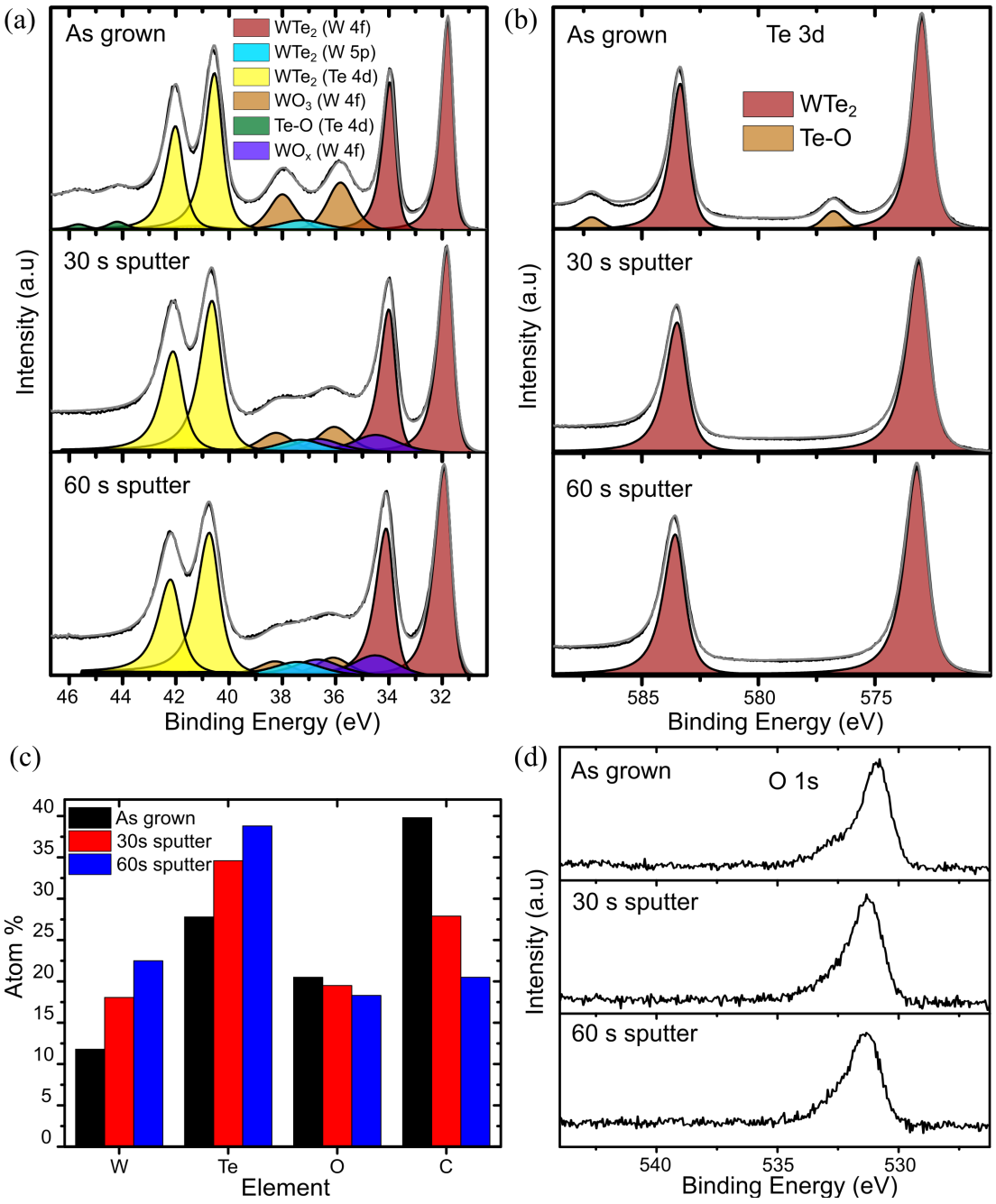


Figure 5.4: (a) XPS spectra of the W 4f region for a WTe_2 sample. The top panel is the as grown surface, while the middle and bottom are after 30 and 60 seconds of Ar-ion sputtering respectively. (b) The same data for the Te 3d BE region. (c) Chart showing the relative atomic percentages of W, Te, O and C on the surface at the three sputtering stages. (d) XPS spectra of the O 1s region of the sample with the top panel being as grown and the middle and bottom being after 30 s and 60 s sputtering respectively. All peaks were charge corrected to the C 1s orbital at 284.8 eV. Atomic percentage and stoichiometry data from these plots is given in Table 5.1.

Ar sputtering were carried out, with the results shown in Figure 5.4.

The more simple Te spectra will be discussed first. The Te 3d core-level spectra show that after 30 seconds of sputtering only a single doublet corresponding to Te in the form of WTe_2 is visible. On the surface 8% of the Te atoms were originally bound to oxygen, while this drops to below the detection limit of the tool after 30 seconds of sputtering. This indicates that the Te oxide is only present on the surface with virtually none in the bulk of the sample.

As referred to previously, the W plot is more complicated due to overlapping core levels in this energy region. For this reason, again only the W 4f will be analysed. The signal from WO_3 reduces significantly after sputtering, from about 30% initially, to 10% after 60 seconds. During the same time the percentage of W atoms in the form of WTe_2 remains roughly constant at 70%. The difference is accounted for by the development of a WO_x signal, this makes up slightly less than 20% of W atoms after 60 seconds of sputtering. This WO_x is a broad peak which is not present in the surface scan but develops after sputtering. It is also apparent that all the W peaks broaden after sputtering, due to damage or amorphisation caused by the sputtering process.

To summarise, the TeO_2 and WO_3 are primarily only measured on the surface of the films. However, a WO_x signal is present after sputtering, and the percentage of W atoms present as either WO_3 or WO_x is roughly constant throughout. Finally, the overall ratio of W to Te on the surface changes after sputtering, with the sample becoming increasingly deficient in Te. All of these factors imply one of two things. Either the sample is more Te deficient below the surface, and also has WO_x in this region but not on the surface. Or, the Te is being preferentially sputtered, meaning that the sample becomes more W rich during this process, and the WO_3 is not being effectively sputtered but rather becoming WO_x. This could be due to the difference in atomic mass between Te and W causing preferential sputtering of Te. The latter theory also correlates more sensibly with previous

Table 5.1: Data for WTe_2 sputter XPS

		Pristine	30 seconds	60 seconds
Atomic ratios	W	12%	18%	23%
	Te	28%	35%	39%
	O	21%	20%	18%
	C	39%	27%	20%
Bonding state of Te	Te - W	92%	100%	100%
	Te - O	8%	0%	0%
Bonding state of W	W - Te	71%	69%	73%
	WO_3	29%	16%	10%
	WO_x	0%	15%	17%
WTe_2 stoichiometry		$WTe_{1.70}$	$WTe_{1.78}$	$WTe_{1.50}$

reports that indicate the self-limiting nature of WTe_2 oxidation. Furthermore, this conclusion also aligns with why strong degradation of the Raman signal from the samples is not seen, even after long exposures to atmosphere. Raman is a less surface sensitive technique than XPS. As it probes a greater depth, the WTe_2 signal remains dominant.

Figure 5.4 (c) charts the relative atomic percentages of W, Te, O and C on the surface at each stage of the sputtering. There is a dramatic decrease in the percentage of C on the surface as it is cleaned by the sputtering, this is accompanied by an corresponding increase in W and Te. The percentage of O present meanwhile shows only a small decrease after the sputtering process. This relative stability is also seen in Figure 5.4 (d) where the unfitted XPS spectra of the O 1s core level is plotted. While this peak shifts and broadens slightly after sputtering, it remains otherwise relatively unchanged. All atomic ratio and stoichiometry data is given in Table 5.1.

As a final note, it should be mentioned that XPS analysis of other WTe_2 films showed higher levels of surface oxidation, indicating some variability in samples.

5.6 Morphology of films

The morphology of the WTe_2 films was examined with SEM, images of a typical film are shown in Figure 5.5(a)-(c). It is immediately apparent that the surface of the film consists of two differing morphologies. There are discrete patches containing elongated flakes of WTe_2 on the order of several micrometers and, surrounding these, are areas of smaller flakes with lengths below 500 nm. The presence of these two starkly different morphologies gives an indication of the growth mechanism of the films, and will be discussed further in Section 5.8. It should be noted that Raman analysis indicated that there is WTe_2 throughout the surface, confirming that both areas do convert to the TMD, despite appearing quite different.

Examining Figure 5.5(c), it is clear that the WTe_2 grows as distinct elongated flakes, with high aspect ratios and lengths of up to 10 μm. This is very different from the polycrystalline films seen for the TAC growth in Chapter 3, which had grain sizes of below 100 nm, or even the growth of $MoTe_2$ in Chapter 4, in which the flakes are much more integrated with the surface, forming a film.

This elongated growth is due to the quasi-1D nature of WTe_2, as discussed in Section 1.1.2. It is expected that the long axis of the flakes is parallel to the direction of the 1D chain of W atoms in the WTe_2, similar to elongated growth of WTe_2 flakes that has been seen in CVD growth of WTe_2 in a number of works.[85,126,127] WTe_2, with a very similar form factor to that seen here, was reported by Kwak *et al.* in their work on the growth of WTe_2 nanobelts.[136] In that work, films of W and Cu were deposited on a substrate, these were then exposed to Te vapour. This caused a $CuTe_x$ alloy to form, in which the WTe_2 grew. Following a post-growth etch to remove residual $CuTe_x$, WTe_2 nanobelts, very similar to the flakes grown here, were reported.

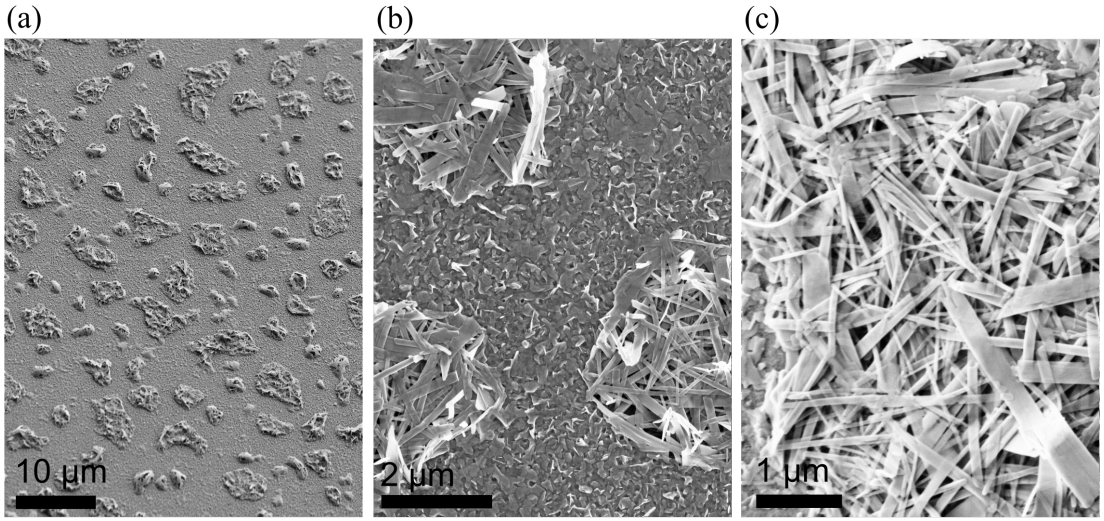


Figure 5.5: SEM images of the surface of a typical WTe_2 film grown from an initial 40 nm W film.

5.7 Growth temperature investigation

The temperatures at which WTe_2 grows, using this experimental procedure, were investigated by conducting furnace runs at various temperatures. The results indicate that the growth range is similar to that of $MoTe_2$. Looking at Figure 5.6, the Raman signal for WTe_2 is visible between 450 °C and 650 °C inclusive. The furnace run at 350 °C shows no conversion, with only the peaks of Te visible, similar to the unconverted films. At 400 °C, some conversion can be seen but the signal is quite weak and noisy. Above 650 °C, there are no products visible in the majority of the Raman spectra taken, with only occasional oxide signals present.

CVD growth of WTe_2 reported in literature is typically carried out in the region of 750 - 800 °C.[127,130] Works that have use mechanically-exfoliated flakes from CVT grown crystals of WTe_2, typically grew these at 800 - 950 °C.[51,246] Both of these methods operate in a much higher temperature regime than that used here. This method offers a significant advantage by allowing a wider choice of substrates, and increased chance of integration into pre-existing processes. The potential mechanisms of this growth method are similar to those discussed for $MoTe_2$ in Chapter 4, and are addressed below.

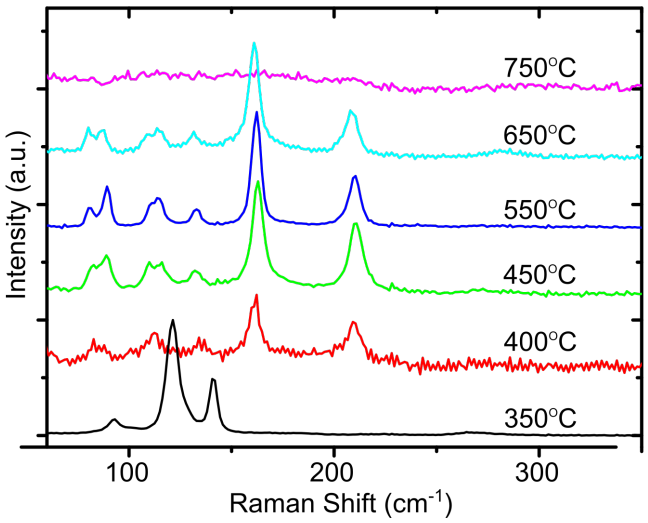


Figure 5.6: Raman spectra of WTe_2 films grown at various temperatures.

5.7.1 Growth mechanism

There are a number of challenges when analysing the growth mechanism using this system, such as ensuring exact reproducibility in reactant quantities and growth conditions, along with the inability to vary certain parameters, such as the introduction time/temperature of reactants. It is possible nevertheless to gain some insights, and draw broad conclusions about the reaction.

As already discussed for $MoTe_2$, phase diagrams can provide valuable information when analysing the growth of a material in systems such as this. Figure 5.7 is a reproduction of the binary phase diagram for W-Te.[247] The diagram indicates that WTe_2 is the only compound that forms between W and Te, and that it is stable between room temperature and 1293 K.

In this growth, Te melts as the furnace temperature rises above the Te melting point, 450 °C or 723 K. At this point, an intermixed layer forms at the boundary between the W and Te, as a result of the W dissolving into the Te. On the phase diagram this manifests as the liquid moving from the leftmost side of 100% Te, slightly towards the right, where it is a liquid alloy of WTe_x. It is clear from the phase diagram, that at these growth temperatures (450 °C to 650 °C) the alloy

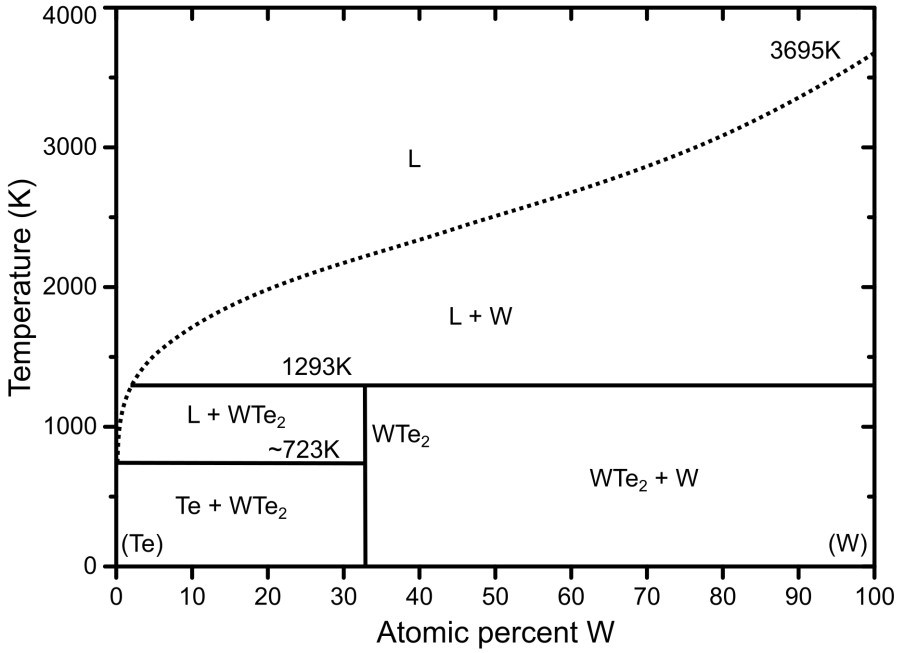


Figure 5.7: Reproduction of binary phase diagram of W-Te with the temperature measured in Kelvin.[247]

remains liquid for only a very small percentage W, beyond which it becomes supersaturated. This means that, as more W dissolves into the Te, small solid WTe_2 crystals begin to nucleate and grow within the liquid alloy. This maintains the liquid alloy composition of very close to 100% Te, while the overall system (liquid Te and WTe_2 crystals) move further towards the right with increasing W concentration.

Concurrent with this, the Te is evaporating, further increasing the W:Te ratio and driving the growth of WTe_2 crystals. If the growth is sufficiently long, all unreacted Te will evaporate, leaving a film solely of WTe_2 during the cool-down. This offers an explanation as to why the growth only occurs effectively above 450 °C, below this the formation of an intermixed layer would be greatly reduced due to the Te not melting, which would dramatically hinder the growth.

The upper bound of ∼650 °C cannot be understood from the phase diagram, which indicates stability up to ∼1000 °C. The proposed reason for the upper bound seen here is the same as was discussed for $MoTe_2$ in Section 4.5 - that

the Te evaporates too quickly to react effectively, or any WTe_2 that does form decomposes through loss of Te due to the Te-deficient environment.[212,213] This loss would not occur in CVT growth due to the vessel being sealed, maintaining high Te concentrations.

5.8 Morphology variation

Variation of the quantity of W and Te present on the sample was found to have a strong effect on the morphology of the WTe_2 films. While all were qualitatively similar, the size of the features varied greatly. To investigate this, samples were fabricated with initial W film thicknesses between 2 and 40 nm and between 5,000 and 40,000 pulses of Te. The thickness of the Te layers corresponding to different numbers of pulses will be discussed in Section 6.7. Post conversion to WTe_2, the films were analysed with SEM and average flake and patch sizes found by taking averages of over 30 flakes/patches.

The results of this analysis is shown in Figure 5.8. The effect of W and Te quantity on the length of the WTe_2 crystals is shown in Figure 5.8(a). This colourmap plot has W thickness (as measured by sputter tool QCM) on the x-axis and number of pulses during Te electrodeposition on the y-axis. The average lengths of the flakes are shown in the colour scale with red indicating longer. The data from these plots is shown in Table 5.2.

The average length of the flakes varies between <100 nm and 1600 nm, over the parameter space examined. It was found that increasing the quantity of Te has a large effect on increasing flake size, while increasing W does so to a lesser extent. In Figure 5.8(b), the same analysis is displayed for the area of the patches containing the elongated WTe_2 flakes. This shows a similar result with Te amount having a large effect on the size of the patches, while the W thickness only has an effect for the thinnest films.

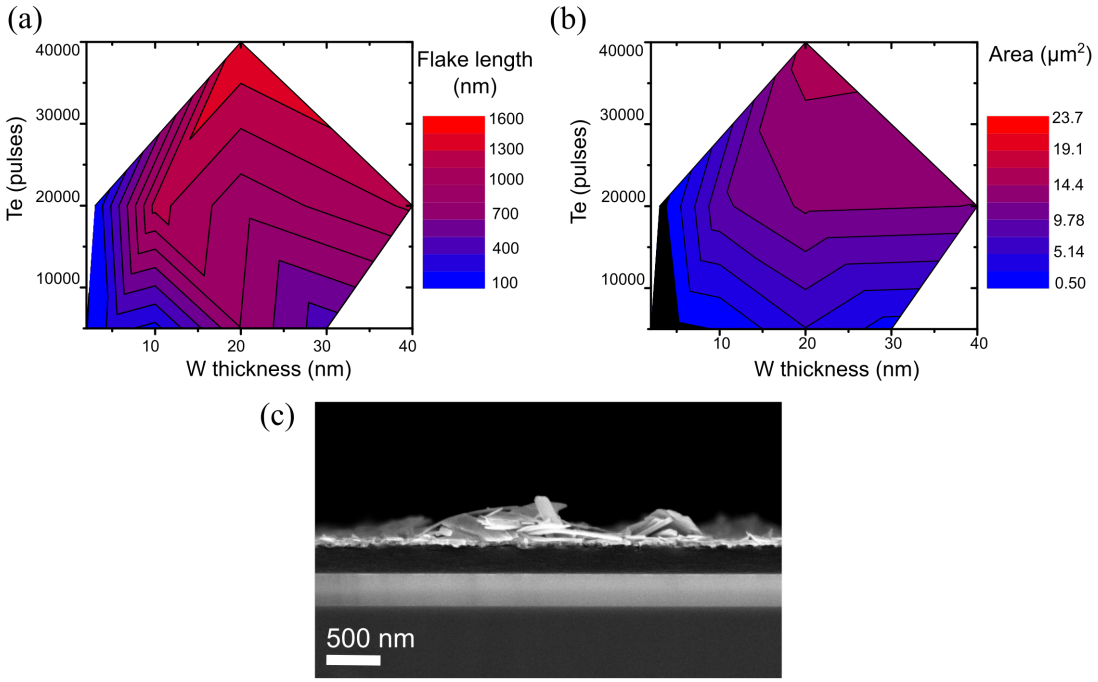


Figure 5.8: (a) Plot of the variation in flake length with changes in the amount of W and Te present. (b) Variation of patch area with changes to W and Te amounts. Data from these plots is given in Table 5.2. (c) Cross section SEM image of WTe_2 film showing raised droplets.

Table 5.2: Morphology data for WTe_2 films

W deposition (nm)	Te depoisition (pulses)	Patch Area (μm^2)	Flake length (nm)
2	5000	0.5	94
3	20000	-	114
5	5000	-	364
5	5000	0.6	230
10	5000	0.6	202
10	20000	9.2	1210
20	5000	5	846
20	20000	15	756
20	20000	12	940
20	20000	9.5	988
20	40000	0.7	1530
20	40000	24	1350
30	5000	1.8	458
40	20000	12	1180

5.8.1 Morphology mechanism

The morphology of the films can be primarily explained by considering the quantity of Te present, along with its behaviour during the growth. As the furnace reaches growth temperature, and the Te melts, the reaction between the W and Te initiates, as is described in Section 5.7.1. However, at some point the Te tends to dewet from the surface to form droplets. The dewetting of the Te indicates that the surface energy interaction between the W and Te is less than the energy that the Te gains by minimising its surface area through droplet formation. Naturally, increased amount of Te present during the reaction (thicker initial Te layer), results in larger droplets forming. These droplets are what result in the patches of larger WTe_2 flakes on the surface. It is clear that the droplets do not form immediately as Raman analysis indicated that there was WTe_2 growth over the entire surface.

The size of the WTe_2 crystals grown in the film is affected by the Te quantity in two ways. Firstly, more Te provides more reactant, allowing larger crystal growth. Secondly, as the reaction occurs in the liquid Te alloy, more Te provide a greater length of time for the reaction to occur before the Te vaporises. This explains the findings of larger crystals with increased Te in Section 5.8, but also the larger crystals in the vicinity of the Te droplets. These droplets serve as areas of high local reactant quantity, and long growth times, enabling much larger crystals to grow than in surrounding areas.

The lesser effect of W suggests that below a certain point it limits the growth, but above a particular threshold, it no longer has a strong influence on flake size. This correlates well with results published for similar systems.[66]

If one looks at a cross section SEM of these films, shown in Figure 5.8(c), it is clear that the droplets were raised above the majority of the surface and that the WTe_2 crystals grew within them. This indicates that the W tends to dissolve into the Te rather than the Te etching down into the W, as was the case in the

work of Kwak *et al.*[136]

The majority of this growth discussion is also applicable the $MoTe_2$ and $PtTe_2$ growth. However, in those cases the tendency of the Te to dewet is different. In $MoTe_2$ there is a much lower tendency for the Te to dewet from the surface of the Mo. This results in a growth that occurs more uniformly over the surface without giving the patches of large crystals. For $MoTe_2$ the flakes also grow predominantly vertically from a thin, intermixed layer of Mo and Te on the surface. The tendency of the Te film to dewet from the underlying metal is likely due to the differing surface energies of the metal films. The Te would, in theory, be less likely to dewet from a metal film with higher surface energy as this would minimise the overall energy of the system. While there are values available for the surface energies of metals, due to their strong dependency on crystallographic planes it is difficult to apply them to the rough, nanoscale, potentially oxidised films in this work.[248,249]

5.9 Application as electrocatalyst

The electrocatalytic properties of the WTe_2 films were investigated by measuring their activity as an electrocatalyst for the HER. As discussed in the introduction of this chapter there have been some investigations of WTe_2 for electrocatalytic applications. However the best results demonstrated thus far have been modest when compared to other TMDs. The experimental set-up was the same as that used for measuring the $MoTe_2$ films and is described in Section 2.3.9.

WTe_2 films were grown using on SiO_2/Si with PyC as the current collector. No consistent trends in the electrocatalytic activity was found when either the amount of W or Te used in the growth were varied, despite this being shown to play a strong role in the morphology of the films. As such, any variability in electrocatalytic behaviour was assumed to be due to other factors and all analysis was carried out on averages of different films.

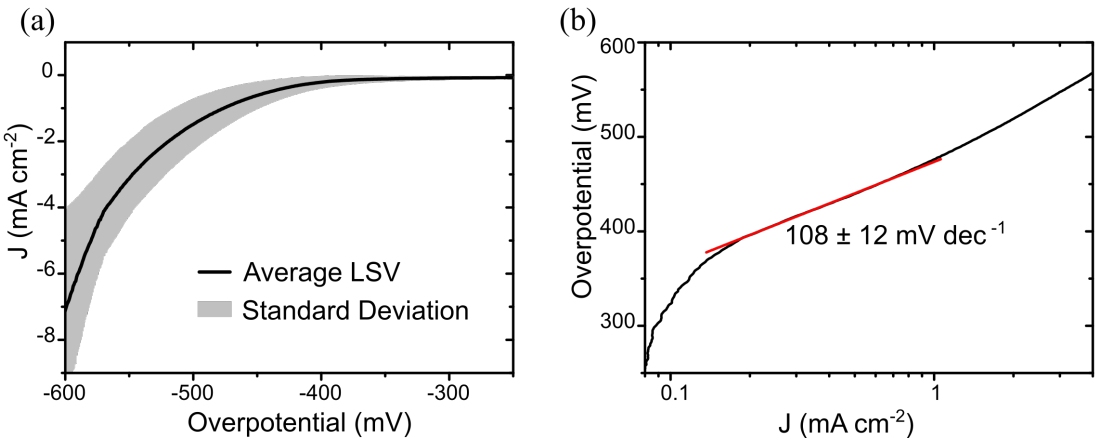


Figure 5.9: (a)Average LSV for 10 WTe_2 films with shaded grey area indicating the standard deviation of the results. (b) Corresponding Tafel plot, with fitted slope, of average WTe_2 response.

Shown in Figure 5.9(a) is an average LSV for 10 WTe_2 films, with the standard deviation shown in grey. From this, the onset potential (OP required to measure 0.5 mA cm^{-2} of current density) was found to be -440±40 mV. This is ∼100 mV higher than the average onset potential for the best performing $MoTe_2$ films, shown in Section 4.8. The average Tafel slope for WTe_2 was found to be 108±12 mV dec^{-1}, again indicating lower performance than for the $MoTe_2$ films. This behaviour is somewhat expected as previous studies using LPE flakes of the Group VI TMDs to catalyse the HER found WTe_2 to be the least active.[80] A potential explanation for this is that the W sites are reported to have a relatively large positive Gibbs free energy of adsorption for H.[83] Interestingly, the work of Li *et al.* using nanoribbons of WTe_2 for the same application, showed much more impressive catalytic response with current densities of 10 mA cm^{-2} at -430 mV OP.[82] This anomalously high result may be an indication the strong influence the form factor of a material can have for electrocatalytic applications. In this study, the overall low performance of the films may also be related to the rapid oxidation of the surface as seen in Section 5.5.

5.10 Transferred flakes of WTe_2

5.10.1 Transfer process

The films consisted of relatively large (10μm), distinct flakes of WTe_2. As many of these flakes were detached from the substrate, and one another, it offered the opportunity to isolate individual flakes by transferring them onto another substrate. This allowed examination of individual flakes, in a manner not possible as a film. The method used to transfer the flakes will be described briefly below.

In order to grow the films with the largest possible WTe_2 flakes, samples with 40 nm of W and 40,000 pulses of Te were used. All samples were grown on PyC to aid the Te electrodeposition, however this did complicate the transfer somewhat. A schematic of the transfer process is shown in Figure 5.10. Firstly, a piece of tape was pressed down onto the sample with appropriate force (firm pressure under finger), before being removed, taking the WTe_2 and PyC layers with it. A second piece of tape was then pressed onto the first and removed. This second piece then had PyC in contact with the tape, and some WTe_2 flakes on top of this. This piece was then pressed onto a fresh SiO_2/Si wafer substrate and removed, resulting in WTe_2 flakes being deposited, as can be seen in Figure 5.11. This piece of tape could be used to deposit on multiple substrates, with each repetition giving less dense arrays of WTe_2 flakes. This technique was successfully used to transfer flakes for further analysis and for electrical device fabrication. The same methodology was used to transfer WTe_2 flakes onto TEM grids for analysis.

5.10.2 AFM of flakes

Figure 5.11(a) and (b) show optical images of the flakes on the transferred substrate. The largest flakes measure about 10 μm long. A sample AFM of these flakes is shown in Figure 5.11(c). Examining the AFM images it was found that

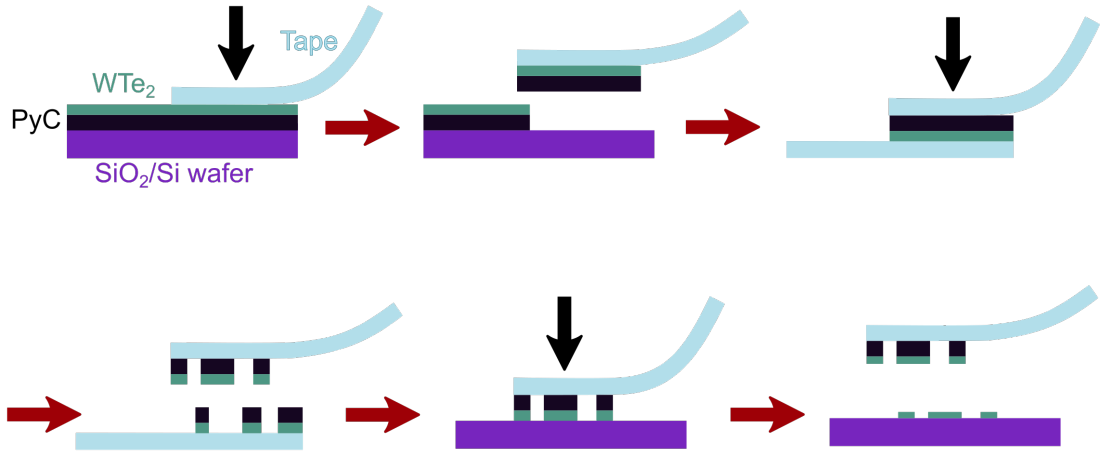


Figure 5.10: Schematic of the transfer process for obtaining individual WTe_2 flakes on a separate substrate.

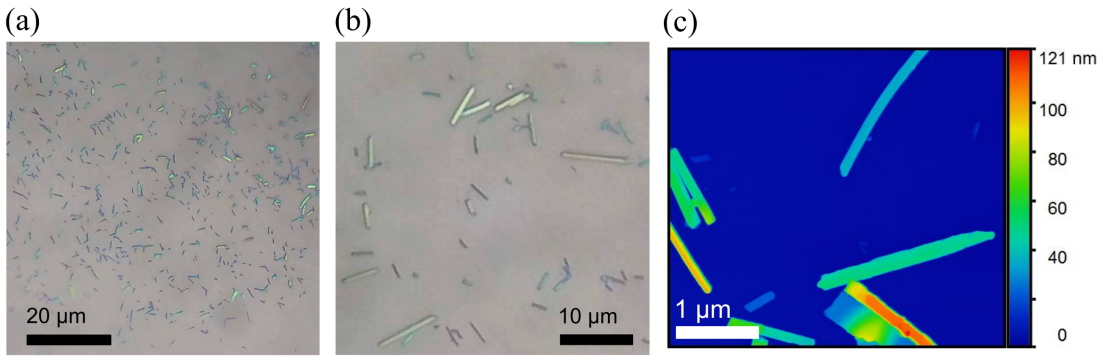


Figure 5.11: (a) & (b) Optical images of transferred WTe_2 flakes on SiO_2/Si. (c)AFM image of transferred WTe_2 flakes.

the flakes varied in thickness between 20 nm and ∼130 nm. The AFM survey primarily looked at larger flakes, and as such, it is expected smaller flakes with thicknesses below 20 nm would also be present. Even so, these flakes are well into the range of displaying bulk-like characteristics, with the number of WTe_2 layers estimated to be between ∼30 and ∼200.

5.10.3 Raman analysis

As mentioned in Section 5.3, it was noticed that there were some variations in the relative intensity of Raman peaks across, and between, the WTe_2 films measured. The ability to measure Raman spectra of individual transferred flakes allowed this to be investigated further. While straightforward in theory, this proved to

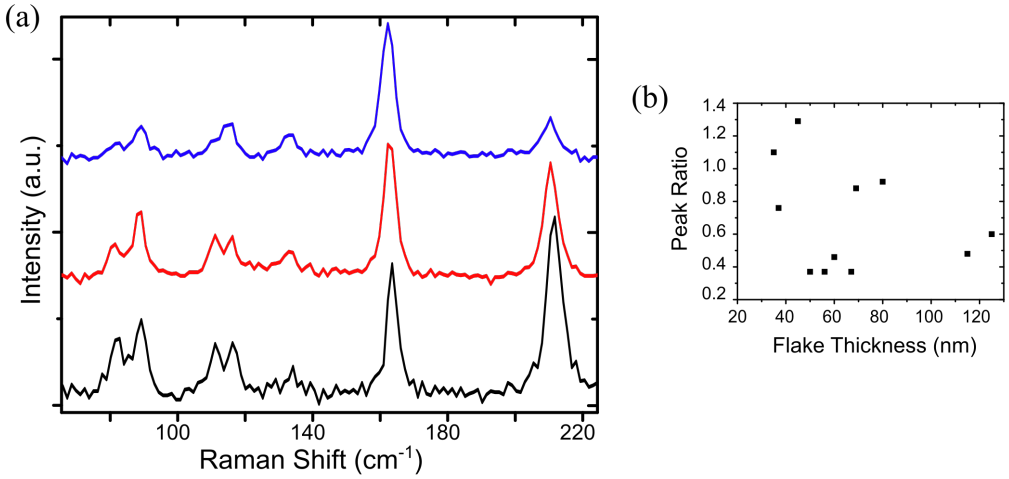


Figure 5.12: (a) A number of Raman spectra for WTe_2 flakes illustrating the differences between them, along with the high level of noise in the measurements. (b) Scatter plot of the extracted peak ratios (peak at 210 cm^{-1} to peak at 162 cm^{-1}) versus flake thickness.

be quite challenging in practice due to two factors. The size of the flakes relative to the laser spot size (∼300 nm) limited the number of individual spectra in the Raman maps taken. Secondly, the inability to use high laser power due to the tendency of WTe_2 to degrade, meant that the Raman spectra were quite noisy.

Figure 5.12(a) shows the Raman spectra for three of the flakes examined and highlights the differences seen between flakes. Only the peaks at ∼162 cm^{-1} and 210 cm^{-1} gave sufficient signal to examine trends. These peaks were fitted with Lorentzian functions and the intensity, position and full width at half maximum (FWHM) extracted. The only property that showed significant variation was the intensity ratio between these two peaks. Both of these peaks have A_1 symmetry, with the peak at ∼162 cm^{-1} being due to vibrations of atoms parallel to the WTe_2 atomic planes, while the ∼210 cm^{-1} peak is due to a vibration that has an out-of-plane component.[202] It has been previously shown in WTe_2 that the thickness of flakes can affect the relative intensities of Raman peaks, though usually in a much thinner regime, below 10 atomic layers.[59] Nevertheless, AFM was carried out on the same flakes, and the ratio of these two Raman peaks plotted against the thickness of the flakes, as shown in Figure 5.12(b). There was however,

no clear trend found between the flake thickness and the Raman spectra using this analysis. Further studies, such as polarised Raman spectroscopy, would be required to determine the factors causing variations seen in the Raman specta.

5.10.4 TEM/STEM of WTe_2 crystals

The transfer of individual WTe_2 flakes opened up the possibility of examining the WTe_2 using TEM, without having to fabricate cross-section lamellae, as was carried out for $MoTe_2$. The same transfer method, as was described for transferring onto SiO_2/Si, was used to transfer WTe_2 flakes onto TEM grids for analysis. Despite being successful, this method did tend to tear the majority of the TEM grids making the yield of samples suitable for subsequent TEM imaging quite low.

Initial analysis of the flakes was carried out using HRTEM. Figure 5.13(a) is an image from that analysis of a flake, with the corresponding fast Fourier transform (FFT) shown in (b). These highlight the crystalline nature of the WTe_2 flakes with clear lattice fringes visible in the TEM image and discrete spots in the FFT.

To further examine the the crystal structure and quality, STEM was carried out on the flakes. This analysis allowed atomic resolution images to be captured. As previously discussed, the yield of the transfer process onto TEM grids was quite low. This, combined with the majority of the flakes being quite thick, made obtaining high-contrast, atomic-resolution images of these samples quite challenging. However, by focussing on areas close to the edge of the flakes, which tended to be thinner, some atomic resolution images, such as the one shown in Figure 5.13(c), were obtained. This image clearly shows that these flakes have a high level of crystallinity, with no grain boundaries visible over the area examined.

As this image was still somewhat noisy, spatial averaging was carried out. This technique was developed by Prof. Lewys Jones and implemented in the Gatan Digital Micrograph software.[250] Initially, a small area (4 nm x 4 nm in this case),

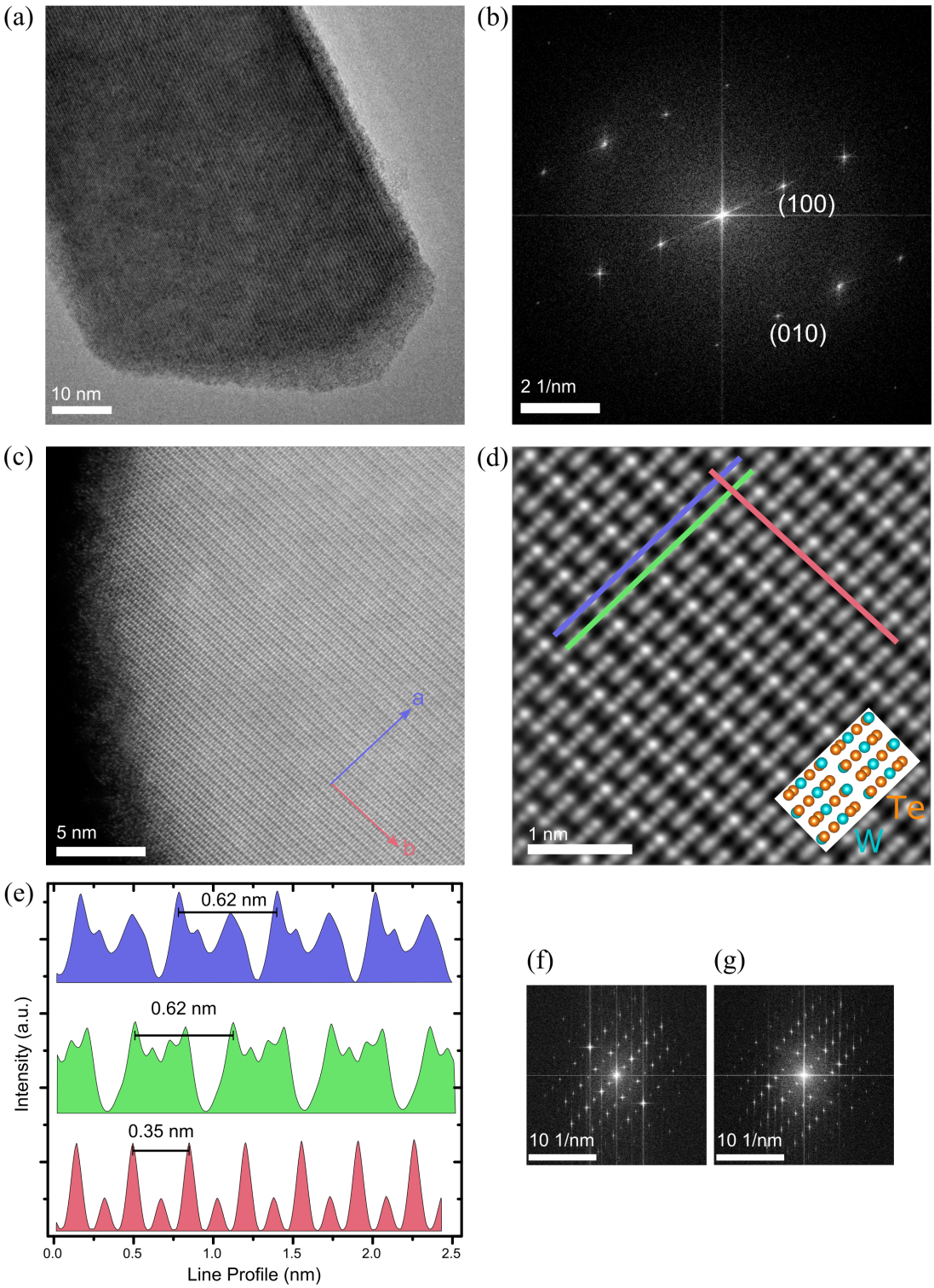


Figure 5.13: (a) HRTEM image of WTe_2, flake (b) FFT of image (a), (c) STEM image of the edge of a WTe_2 flake, with the WTe_2 crystallographic directions marked. (d) Atomic resolution image of WTe_2 crystal, compiled by averaging areas of (c). Insert: atomic positions of WTe_2 for appropriate crystallographic direction (e) Profiles of intensity measured from lines indicated in (d), (f) & (g) FFT of images of opposite ends of a flake indicating the same crystalline phase and orientation in both.

with atomic resolution is chosen. The software then scans the remainder of the image and finds all the areas with which this image matches to a high degree. All of these areas (300 in this analysis) are then extracted and stacked to form an average image. Further image processing then removes any distortion in the image. The result of this analysis is shown in Figure 5.13(d). This shows very clear atomic resolution giving and the expected T_d structure of WTe_2. This matches well to previously published images of WTe_2.[56,136]

Measuring the intensity along the two crystallographic directions of this image, gave the line profiles shown Figure 5.13(e). The red profile shows a repeating pattern every 0.35 nm. This matches closely to the lattice constant of WTe_2 along the [010] crystallographic direction of 0.3496 nm. While the repeat period in the orthogonal direction of 0.62 nm, is very close to the the unit cell length of 0.6282 nm for WTe_2 along the [100] direction. Using this information, along with the spacings obtained from the FFTs, allowed the conclusion to be drawn that it is the (001) lattice planes that are being examined in this case. A model of the expected atomic positions in this case is shown in 5.13(d) insert. This matches quite well to the alternating lines of atoms observed in the STEM image. When viewed from this direction atoms in WTe_2 do not line up in prefect atomic columns meaning that exact atomic positions cannot be assigned despite the clarity of the image.

Examining again Figure 5.13(c), it is possible to assign the lattice directions a and b, as shown by the arrows. This confirms that the W zigzag chains, which form along the b crystallographic direction in T_d WTe_2, are parallel to the long axes of the flake growth as expected.

STEM images were taken from either end of a WTe_2 flake, several micrometres in length, the FFTs of these images are shown in Figure 5.13(f) and (g). These match to a very close degree, offering further confirmation of the single crystalline nature of the flakes. It should be noted that there is some distortion in the images shown here. The orthogonal crystalline directions have measured angles

of ∼87 ° between them. This is thought to be most likely due to scan distortion or slightly misalignment of the crystalline axis during imaging.

5.10.5 Electrical characterisation

A further opportunity provided by the ability to transfer flakes, was to use EBL to fabricate electrical devices, facilitating the electrical characterisation of individual flakes. This allowed the electrical behaviour of crystalline WTe_2 to be probed without the influence of junctions between WTe_2 grains, as would be the case in polycrystalline films. The devices were patterned by EBL, and e-beam evaporation used to deposit Ti/Au (5 nm/100 nm) contacts. An AFM map of a device is shown in Figure 5.14(a).

The IV response of a flake device is shown in Figure 5.14(b). The device response is linear in the measured region, indicating the Ohmic nature of the contacts. The dimensions from AFM allowed the resistivity of the device to be calculated, this was found to be 9.3 x 10^{-6} Ω m. This low resistivity is expected due to the semimetallic nature of WTe_2. Interestingly, this resistivity matches almost exactly the values measured by Song *et al.* in their paper on the potential use of single crystal WTe_2 nanobelts as electrical interconnects in nanoelectronics.[66] These nanobelts have very similar form, crystallinity and electrical response, indicating that the WTe_2 produced in this thesis are likely of similar quality and suitable for similar applications.

The temperature dependence of the WTe_2 flake resistance was then investigated, with the results shown in Figure 5.14(c). The flake shows a very small change in resistivity with temperature with the change that is observed being that it becomes increasingly resistive as the temperature is reduced. This trend is expected for a semiconducting material but is more unusual for a metallic or semimetallic material.

The temperature dependence of the electrical resistance for some materials

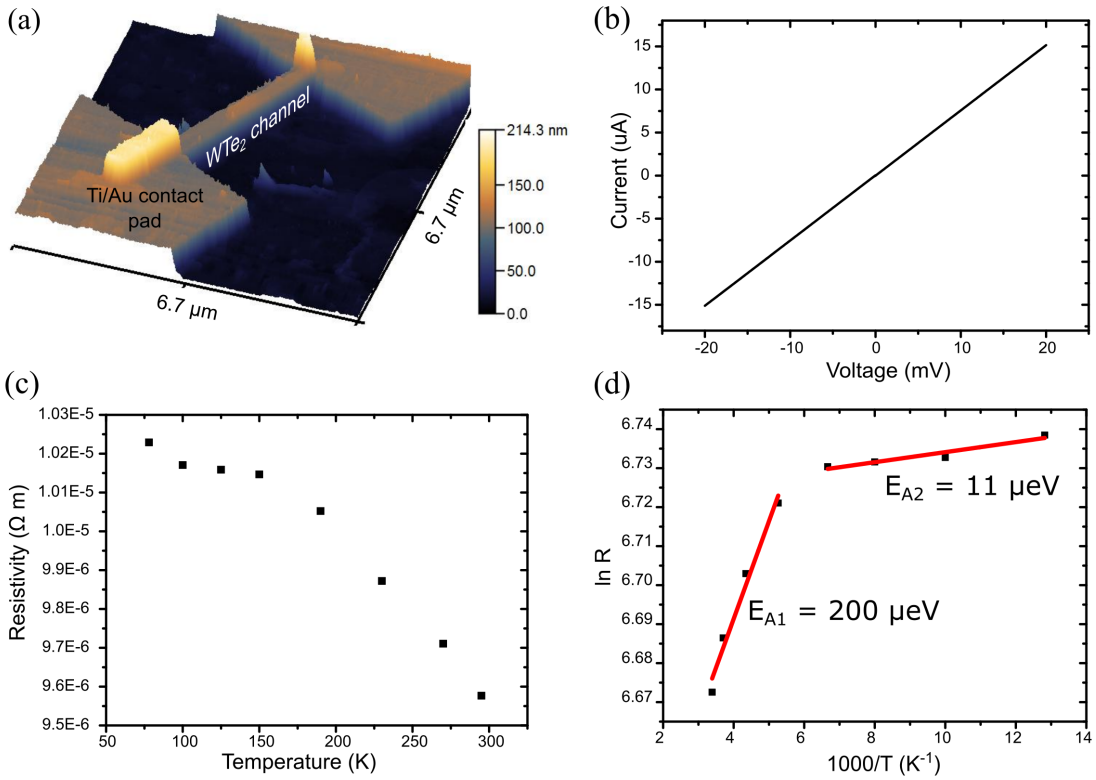


Figure 5.14: (a) AFM image of WTe_2 devices (b) IV of WTe_2 flake (c) Varation in resistivity of WTe_2 flakes with temperature change. (d) Arrhenius plot of the data shown in (c). Two linear regions are fitted and activation energies extracted.

can be explained by the thermal activated charge carriers, given by:

$$R = R_0 \exp\left(\frac{E_A}{kT}\right) \tag{5.1}$$

where R_0 is the pre-exponential factor, T is the temperature in Kelvin, k is the Boltzmann constant and E_A is the activation energy.[251] An Arrhenius plot of temperature dependant resistance allows the activation energy in Equation 5.1 to be extracted. This plot is shown in Figure 5.14(d). There are two linear regions fitted to the data giving activation energies of 200 μeV and 11 μeV in high and low temperature regions respectively. Both of these are very small activation energies showing the weak temperature dependence of the resistivity. This analysis may not be valid for WTe_2 however as the flakes are expected to be semimetallic rather than semiconducting.

There are reports in literature of thin crystals of WTe_2 showing similar reduction in resistance with increasing temperature due to Anderson localization effects, however that was for much thinner (3 - 4 layer) flakes.[66,238] The flake investigated here is estimated to be ∼120 layers thick. In this range, the majority of reports of WTe_2 showed reduced resistivity at low temperatures.[238] A potential reason for the observed result in this case could be that the oxidised surface of the flake resulted in a potential barrier between the flake and contact. The increasing temperature would then cause an increase in the current passing through the barrier. Further studies would be required to confirm this.

5.11 Conclusions

In this chapter the growth of WTe_2 films was demonstrated using a similar process to that for $MoTe_2$. This highlighted the generalisability of the technique, such that it could be expanded to another material with only minor adaptions.

The growth of T_d WTe_2 was verified using Raman spectroscopy, XPS and

XRD. Raman showed spectra that matched closely to previously reported bulk spectra of WTe_2. The XPS analysis showed that the films converted to WTe_2, however there was a large amount of the surface which had oxidised. To analyse this further sputter XPS was taken of the samples. This showed that Te oxide was only on the surface of the sample, though W oxides appeared to remain deeper into the bulk. This was concluded to be likely due to the tendency of the sputtering process to preferentially remove Te, rather than an accurate representation of the bulk characteristics of the WTe_2 films.

SEM analysis of the films showed a surface morphology with two distinct regions - patches that contained much larger micrometre long flakes of WTe_2, surrounded by areas with much smaller flakes. Both of these areas were confirmed to contain WTe_2 by Raman. The formation of this morphology was asserted to be due to the Te dewetting from the surface during the growth, resulting in droplets being formed. These droplets had a much greater supply of reactants (W and Te), resulting in the formation of the patches of larger flakes. Changing the amount of W and Te present on the substrates was found to influence both the flake and droplet size, lending credence to this assertion.

WTe_2 was found to grow between 450 °C and 650 °C using this method. The lower limit being due to the melting point of Te, while the upper is thought to be as a result of rapid loss of Te from the system at higher temperatures. This low temperature growth is a distinct advantage of this growth method in comparison to the majority of previously reported growths of WTe_2.

The transfer of individual flakes allowed for TEM analysis to be conducted. This confirmed the single crystal nature of the flakes and also gave information on the crystallographic direction in the flakes, indicating that the (001) planes of the flakes were predominantly parallel to the substrate surface. The longest axis of the flakes was found to be parallel to the zigzag chains formed by the W atoms.

The application of the WTe_2 films as an electrocatalyst of the HER did not show very active behaviour, potentially due to the highly oxidised surface. Initial investigations of the transferred flakes showed promising electrical results, with conductivities matching previously reported values for WTe_2. The unusual variation of the resistance of the flakes with temperature requires further study to fully explain. These initial electrical results are similar to other previously reported works and highlight the high crystalline quality of the flakes produced, and potential for electronic applications.

This chapter has demonstrated the potential of this growth technique to produce films of TMDs at relatively low temperatures and short times. The directed pre-deposition of the reactants opens up opportunities for patterned growth over large areas, while avoiding the use of potentially hazardous gas-phase Te based precursors.

6

Platinum Ditelluride

6.1 Introduction

The current interest in nanoscale Group X TMDs was initially sparked by theoretical papers extolling the promise of PtS_2 and $PtSe_2$ for photocatalytic applications.[252] PtS_2 has proven quite difficult to fabricate, with PtS often the resulting product of growth attempts.[253] $PtSe_2$ has been fabricated using a number of methods and characterised to reveal a thickness dependant change from semiconducting to semimetallic behaviour.[111,254] Nanoscale $PtTe_2$ is still a relatively unexplored system, with only a small number of published works examining it experimentally.[132,255]

The synthesis of $PtTe_2$ through the reaction of elemental Pt and Te was reported as early as 1897.[193] It has also been reported mineralogically for over 70 years, with descriptions of it in the 1949 Geological Survey as moncheite, though the same name is used to describe $PtTe_2$ with a certain percentage of Pd and Bi.[256] The long history of study of $PtTe_2$ is perhaps not surprising due to the relative scarcity and value of Pt metal. Aside from geological studies, there have also been a number of papers examining the bulk properties of crystalline $PtTe_2$ grown by CVT methods.[257–259] It is only in the last few years however, that it

has been examined as a layered 2D material.

While 1T' $MoTe_2$ and WTe_2 have been shown to be type-II Weyl semimetals, $PtTe_2$ has been predicted to be a potential type-II Dirac semimetal.[70,260,261] These closely related material types are of interest as systems in which to investigate novel quantum phenomena, and for potential applications in spintronics and quantum computing.[262,263] Much of the recent work on $PtTe_2$ has focussed on examining it in the context of these exotic electronic properties.[264,265] $PtTe_2$ has also been examined as a catalyst. It was found to have the greatest electrocatalytic effect for the HER of all the Pt dichalcogenides.[266,267] It has further been reported that the activity of the basal plane can be increased through defect engineering.[268] Finally, it has been reported to be as effective for catalysis of the ORR as Pt/C, while being less toxic by certain metrics.[79]

These potential applications have generated interest in the growth of $PtTe_2$, however, the vast majority of reports published thus far have used $PtTe_2$ crystals grown by CVT.[79,264] This growth method is both time and energy intensive, requiring long anneals at temperatures of up to 1000 °C. The works which have focussed on CVD-grown samples have only demonstrated small discrete flakes, none of which have been monolayer.[132] All these factors leave a pressing case for developing a growth method for $PtTe_2$ that yields large-area samples in a scalable and efficient manner.

6.2 Growth of $PtTe_2$ films

The fabrication of $PtTe_2$ thin films was achieved using a process similar to that described in the previous two chapters for $MoTe_2$ and WTe_2. A brief description will be given here with a focus on the changes specific to $PtTe_2$.

An initial Pt metal layer was deposited onto the substrate using Ar-ion sputtering. The adhesion of this Pt metal to the SiO_2/Si wafer substrates was found to be very poor. This resulted in the Pt film delaminating from the substrate

during the Te electrodeposition process. This precluded any samples of $PtTe_2$ being examined directly on SiO_2/Si. To circumvent this issue, a layer of PyC was grown on the SiO_2/Si prior to deposition of the Pt, as described in Section 2.2.5. This resulted in improved adhesion of the Pt, allowing successful Te electrodeposition on the sample. CV was used to determine the appropriate biasing for the electrodeposition of Te on Pt. A bias of -0.2 V with respect to the Ag/AgCl reference electrode was chosen. The same pulsed electrodeposition program, of 10 ms on and 50 ms off, as previously used for $MoTe_2$ was used.

The furnace step was carried out as previously described. The samples were placed in nested crucibles in the quartz-tube furnace. The furnace was evacuated and filled with N_2 at a pressure of ∼700 mbar. All samples had a growth step consisting of a 90 minute dwell at 450 °C, unless otherwise specified. The samples were then cooled to below 30 °C over three hours under a N_2 atmosphere.

6.3 Raman spectroscopy of $PtTe_2$

The Raman spectrum of a typical film synthesised at 450 °C is presented in Figure 6.1. There are two primary peaks visible in the spectrum, centred at ∼111 cm^{-1} and ∼158 cm^{-1}. These are consistent with previously reported peak positions, and relative intensities, for bulk-like $PtTe_2$.[61,260] $PtTe_2$ is isostructural with $PtSe_2$ and has a CdI_2 lattice type structure, with space group $P\bar{3}m1$ and point group D_{3d}. There are 3 atoms in the unit cell and the D_{3d} symmetry results in the two Raman active modes seen here, the in-plane E_g mode at ∼111 cm^{-1} and the out-of-plane A_{1g} at ∼158 cm^{-1}. This offers initial confirmation of the successful growth of $PtTe_2$.

To investigate the Raman spectra of individual crystals of $PtTe_2$, a similar transfer process to that described for WTe_2 in Section 5.10.1 was used. AFM was used to find the physical dimensions of each flake before Raman mapping was performed. It was found that there was a relationship found between the A_{1g}/E_g

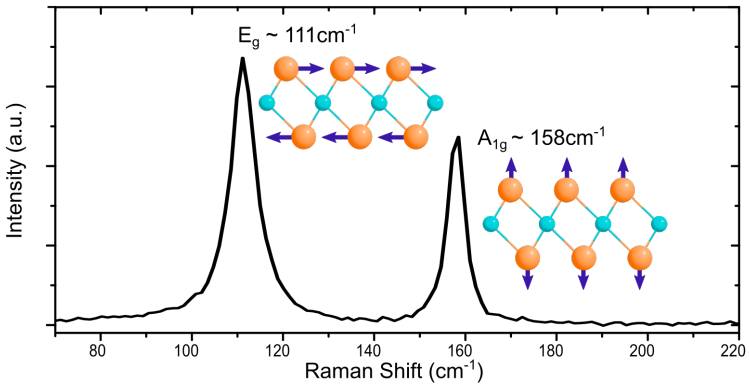


Figure 6.1: Raman spectra of typical $PtTe_2$ film showing the two primary modes and their vibrations on a ball and stick lattice model.

peaks intensity ratio and the thickness of the crystals, while the peak position remained invariant. The out-of-plane A_{1g} peak was found to become relatively less intense as the flake thickness increased, shown in Figure 6.2(a). Published works on $PtSe_2$ have shown the opposite behaviour, with the out-of-plane mode becoming more intense as the films get thicker.[111] In that case however, it was a very different thickness regime being examined, 1 - 10 atomic layers. The crystals being examined here are between ∼150 and ∼450 layers thick - far beyond the range where layer-dependent changes would be expected in the Raman spectra. For this reason it is thought that the changes seen here are not directly related to the thickness.

To analyse this further, SEM images of the same flakes were taken, a representative image of which is shown in Figure 6.2(b). Due to the relatively large step sizes in the crystals, the angle between the visible crystal planes and the substrate can be estimated from the SEM images. The angle of a TMD crystal, relative to the substrate, has previously been shown to influence the ratio of peak intensities in Raman.[119] The influence of this angle on the Raman spectra measured here was examined by plotting the estimated angles against the A_{1g}/E_g peak ratio, displayed in Figure 6.2(c). There is correlation between the angle and the intensity ratio of the peaks. However, a further complication in this system is the variety of shapes, and so step-edge density in the flakes examined, which

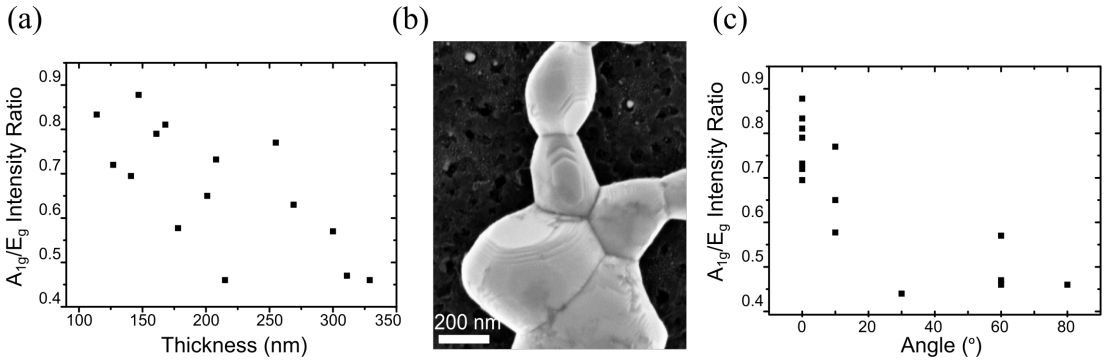


Figure 6.2: (a) Scatter plot showing the relation between the $PtTe_2$ flake thickness and the A_{1g}/E_g intensity ratio. (b) Example of anSEM image of $PtTe_2$ crystal showing the visible step-edges (c) Scatter plot of the estimated angle between the crystal planes and the surface and the Raman intensity peak ratio.

could also influence the Raman measured. Due to this, and the SEM not giving definitive measurements of angle or determination of specific crystalline planes, the reasons for this peak ratio variation cannot be conclusively assigned.

6.4 XPS analysis of films

XPS analysis allowed further confirmation of the growth of $PtTe_2$ films using this growth method. Figure 6.3(a) and (b) display the spectra of the Pt 4f and Te 3d core-level regions of a typical film of $PtTe_2$. The Pt 4f region shows two sets of doublets associated with the Pt $4f_{7/2}$ and $4f_{5/2}$ core levels. The most intense of these is Pt bound to Te, while the smaller component indicates Pt bound to oxygen. Similarly for the Te 3d core levels, the peak for Te bound to Pt is much more intense than the tellurium oxide peak. From these it can be calculated that 10% of the Pt atoms, and 19% of the Te atoms on the surface are in oxide states, while the remainder are $PtTe_2$.

The calculated stoichiometry of the $PtTe_2$ on the surface is $PtTe_{1.8}$, indicating a Te deficiency in the lattice. This is somewhat lower than expected, however when all oxides are included, the Pt:Te ratio is 1:1.94. This value is much closer to the expected 1:2 ratio, likely indicating that immediately after the growth,

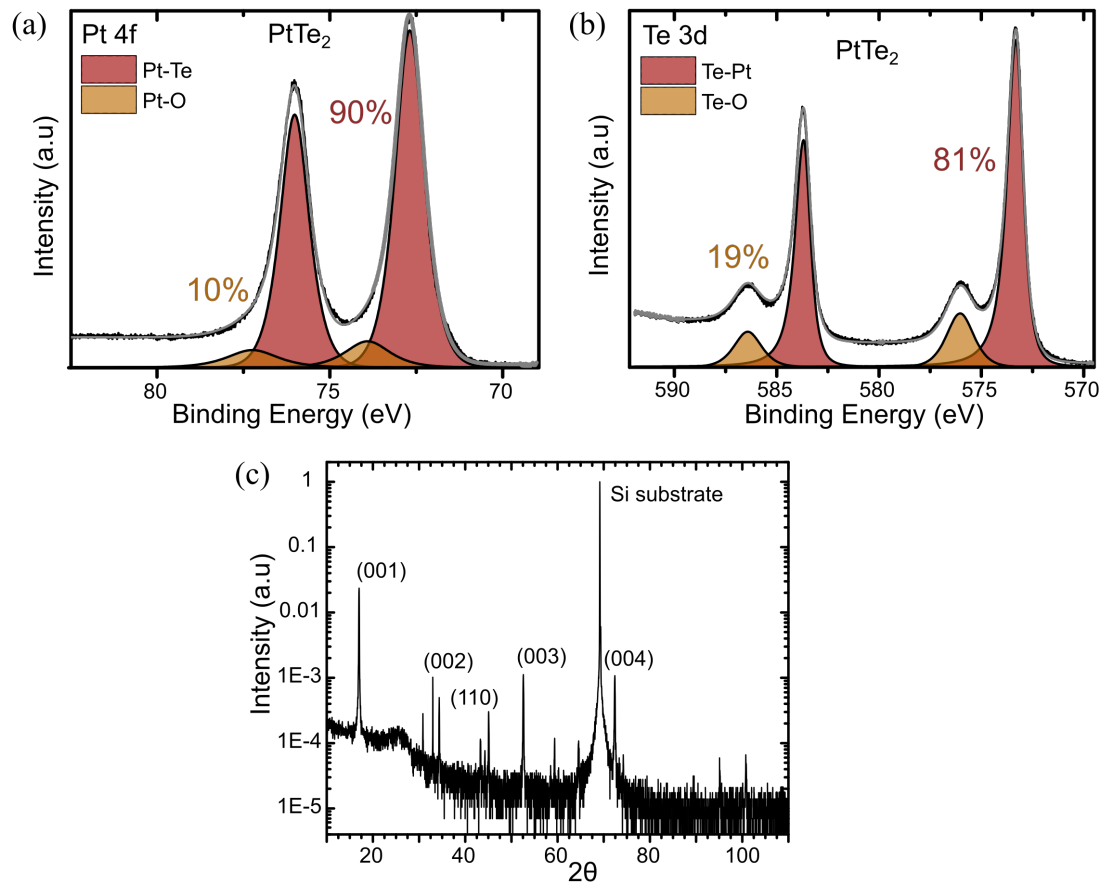


Figure 6.3: (a) and (b) XPS spectra of a $PtTe_2$ film showing the Pt 4f and the Te 3d core levels respectively (c) XRD spectra of $PtTe_2$ film with the most intense peaks labelled. These peaks were charge corrected to the C 1s orbital at 284.8 eV. All XPS data is tabulated in Table 6.1.

the sample contains stoichiometric $PtTe_2$, which then becomes oxidised through atmospheric exposure. It could also be expected that the bulk contains a much lower amount of oxide, similar to other TMDs, and as such is much closer to the correct stoichiometry of $PtTe_2$. All atomic ratio and stoichiometry data for $PtTe_2$ XPS is tabulated in Table 6.1.

Table 6.1: Data for $PtTe_2$ XPS of normal (Figure 6.3), low coverage (Figure 6.7(d)) and post ORR samples (Figure 6.12)

		Normal	Low coverage	Post ORR
Atomic ratio	Pt	34%	34%	61%
of Pt to Te	Te	66%	66%	39%
Bonding state	Te - Pt	81%	19%	52%
of Te	Te - O	70%	30%	48%
Bonding state	Pt - Te	90%	92%	86%
of Pt	Pt - O	10%	8%	14%
$PtTe_2$ stoichiometry		$PtTe_{1.78}$	$PtTe_{1.50}$	$PtTe_{0.49}$

6.5 XRD of films

To obtain additional confirmation of the character of the films, XRD was carried out on a typical sample made from a 10 nm Pt film. The results of this are shown in Figure 6.3(c). There is a large number of a peaks visible in the spectrum, the most intense of these being associated with the substrate at ∼69 °. The other prominent peaks correspond well to the predicted, and previously published spectra for $PtTe_2$.[78,132,260] The (001), (011), (002), (012), (110), (003), (013), (004) and (121) peaks are all discernable, with the most intense of these being labelled on the graph. This offers further confirmation of the growth of crystalline $PtTe_2$, with the noisy background of the spectrum indicative of the polycrystalline nature of the film.

6.6 Growth mechanism and optimisation

As with the other telluride TMDs, while optimising the growth of $PtTe_2$, the temperature range in which it successfully grew was examined. Raman spectroscopy

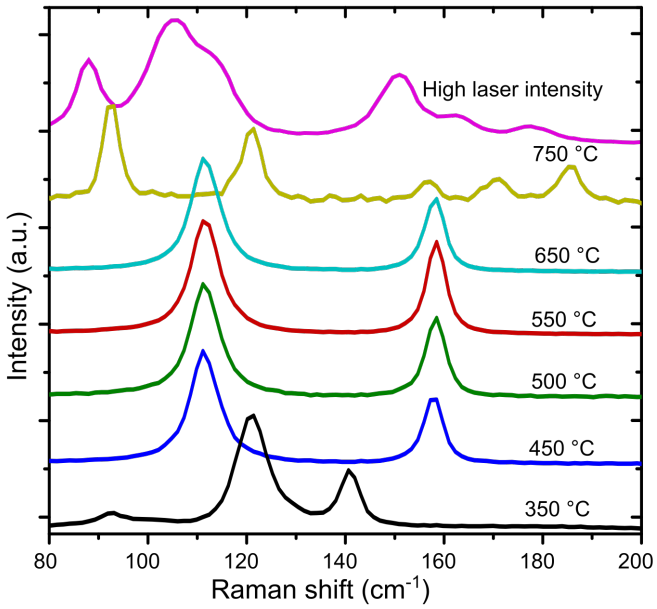


Figure 6.4: (a) Raman spectra of $PtTe_2$ films grown at different temperatures. Also shown is a Raman spectrum of $PtTe_2$ film measured with high laser intensity.

was used to verify successful growth during this process. A series of furnace runs were conducted with a different temperature chosen for the 90 minute growth phase of each.

The Raman spectra of films grown at temperatures between 350 °C and 750 °C are shown in Figure 6.4. Similar to that which was found for $MoTe_2$ and WTe_2, the growth of $PtTe_2$ is only successful above 450 °C, the melting point of Te. As was discussed for the other telluride TMDs, this is due to inefficient reaction between the Te and transition metal when the Te is in the solid phase. Identical Raman spectra, showing the expected E_g and A_g peaks, are visible for films grown between 450 °C and 650 °C. The majority of films grown at 750 °C gave no Raman signal, with some showing a number of peaks, similar to those seen in Figure 6.4. While these peaks are expected to be related to the formation of a platinum oxide, no clear matches in literature could be found, though the peak at ∼186 cm^{-1} is potentially indicative of Pt_3O_4.[269] To investigate this further, films of $PtTe_2$ grown at 450 °C were measured with a much higher laser power than usual, in a similar way to the experiments carried out on $MoTe_2$ in Section

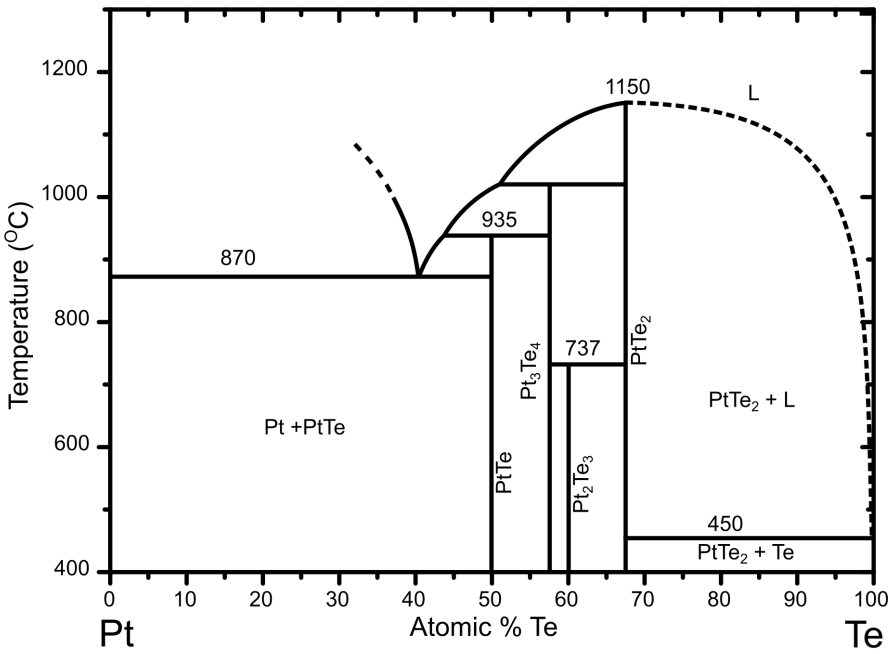


Figure 6.5: Binary phase diagram of Pt-Te system, reproduced from reference.[270]

4.6. The aim was to allow Raman of oxidised films to be examined. The resultant Raman spectrum is shown in Figure 6.4. This spectrum has the expected $PtTe_2$ peaks and a number of other peak unknown peaks. Some of these unknown peaks may be those seen in the Raman of the 750 °C film. Further study would be required to confirm the nature of these peaks.

The inability to grow the films at a higher temperature is again due to the practicalities of this system. At higher temperatures the evaporation of Te before reaction with Pt is complete, or loss of Te from any material which does react inhibits the formation of $PtTe_2$. It is also possible that an unstable product with a lower Te:Pt ratio forms (e.g. Pt_3Te_4), this could then decompose quickly after the growth.

Displayed in Figure 6.5 is a reproduction of the binary phase diagram for Pt-Te.[270] While this growth system is not a near equilibrium process, it is still a useful exercise to examine the diagram. The phase diagram shows that in the case of an atomic ratio of greater than 2:1 for Te:Pt, $PtTe_2$ will be the sole reaction

product, and that this is stable up to 1150°C, though this contrasts with what is observed in this work. There are also a number of other products which may form with lower Te:Pt ratios.

By examining phase diagram, the temperatures of the $PtTe_2$ growth and the similarities to the other materials, the following growth mechanism is proposed. The Te melts as the furnace reaches 450°C, into this a certain amount of Pt dissolves, forming a $PtTe_x$ alloy. As more Pt dissolves, and Te evaporates, the Pt:Te ratio moves the phase from the right-most side of the diagram. This causes $PtTe_2$ solid crystals to begin to nucleate and grow within the liquid. As the growth run continues more $PtTe_2$ nucleates and grows until all the unreacted Te has evaporated.

6.7 Morphology of $PtTe_2$ films

Through the Raman, XPS and XRD analysis it was confirmed that $PtTe_2$ was successfully synthesised. To characterise the films further, SEM and AFM were used to provide information on the film morphology. SEM images of a film are shown in Figure 6.6(a) and (b). Firstly, it is evident that the flakes in these films are much more '3D' than those of either $MoTe_2$ or WTe_2. These $PtTe_2$ flakes do not have any axis that is more than an order of magnitude larger than the others. Another interesting feature is the visibility of very clear crystalline steps and facets on the flakes. This would indicate that these are single crystalline, while also allowing determination of the approximate angle between the layers and the substrate.

Further characterisation was carried out using AFM, shown in Figure 6.6(c) and (d). The AFM allowed the physical dimensions of the crystals to be measured precisely. The crystals are quite thick, with those in Figure 6.6(c), varying between 100 - 400 nm. Laterally, the dimensions are also on the order of a few hundred nanometres. These are much smaller laterally than either the WTe_2 or

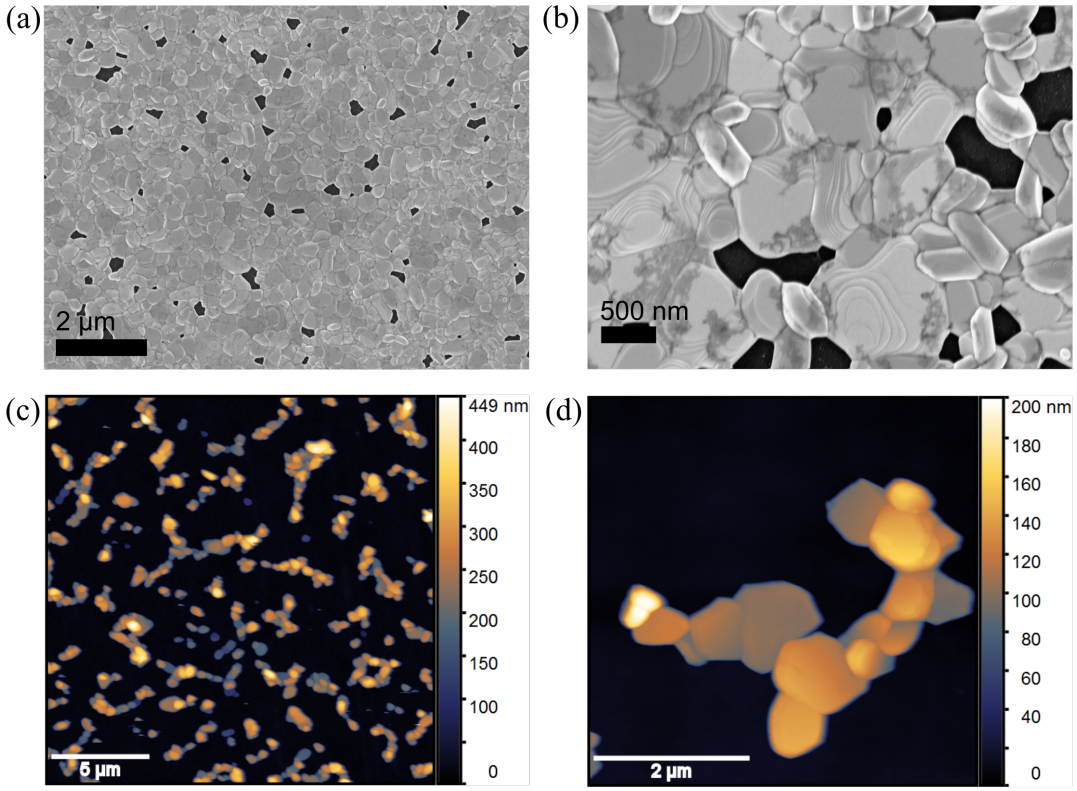


Figure 6.6: (a) & (b) SEM images of $PtTe_2$ films grown from 40 nm Pt and 10,000 pulses of Te. (c) and (d) AFM images of $PtTe_2$ flakes.

$MoTe_2$, while at the same time being thicker. These flakes could not be described as a 2D form of $PtTe_2$ due to the thickness and aspect ratio of the flakes.

It is evident from the AFM and SEM that there are bare patches, of varying sizes, on the surface that do not appear to have any $PtTe_2$ growth on them. To study this, Raman mapping of the samples was carried out and is shown in Figure 6.7. This map of the $PtTe_2$ A_{1g} peak intensity demonstrates that $PtTe_2$ is only present in the areas with visible crystals. The remaining areas were found to only show the Raman signal of PyC.

This proves that there is no $PtTe_2$ in these areas, however Raman would not show any signal from Pt metal that could potentially be present. Therefore XPS analysis was carried on the sample, with the spectra shown in Figure 6.7(c) and (d). This analysis yielded spectra indicating only two states of Pt present. The vast majority of the Pt on the surface was bound to Te, while a small component

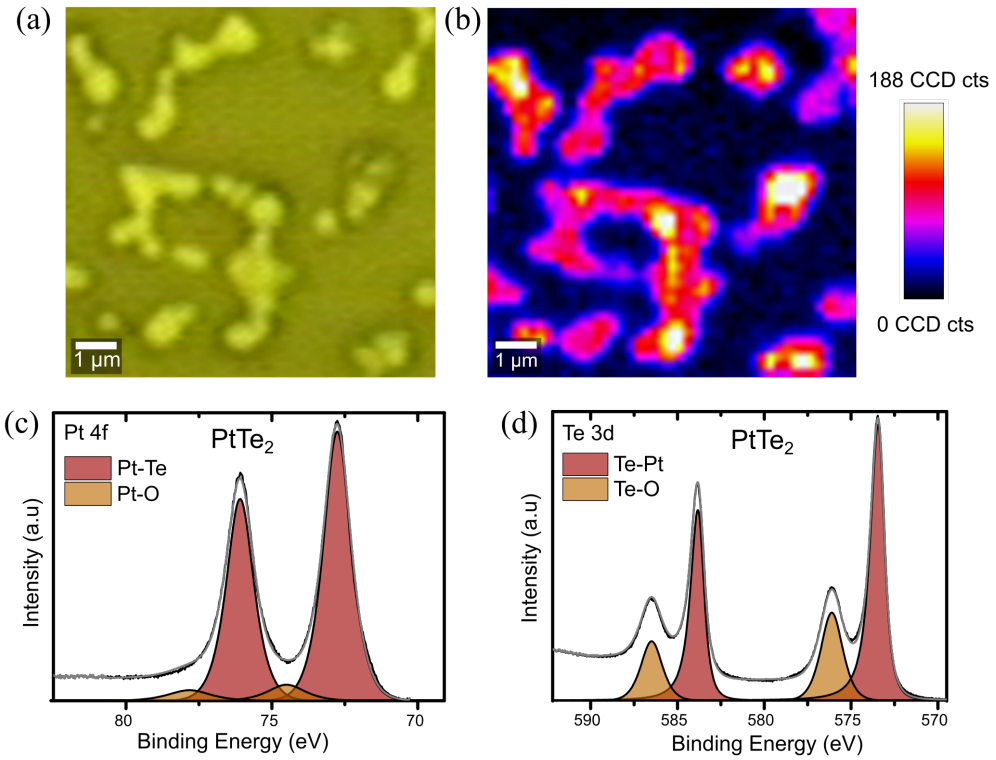


Figure 6.7: (a) Optical image of $PtTe_2$ film. (b) Raman map of the $PtTe_2$ A_{1g} peak intensity for the area shown in (a). (c) & (d) XPS of sample partially covered with $PtTe_2$ indicating only two states of Pt present. These peaks were charge corrected to the C 1s orbital at 284.8 eV. The results of this XPS analysis are shown in Table 6.1

was in platinum oxide states. There was no indication of elemental Pt, within the limits of detection of the measurement. This is despite the surface coverage of the sample being below 30% $PtTe_2$. This gives strong evidence that there is no Pt on the surface between the visible $PtTe_2$ crystals, indicating that both the Pt and Te dewet from the PyC during the growth. This would leave much greater amount of reactant concentrated in certain areas, allowing for the much thicker crystals to grow.

Morphology change with reactant quantity

The extent to which the quantity of Pt and Te present during the growth influenced the $PtTe_2$ flake size and surface coverage was investigated. The quantity of Pt was varied by simply changing the thickness of the deposited Pt layer.

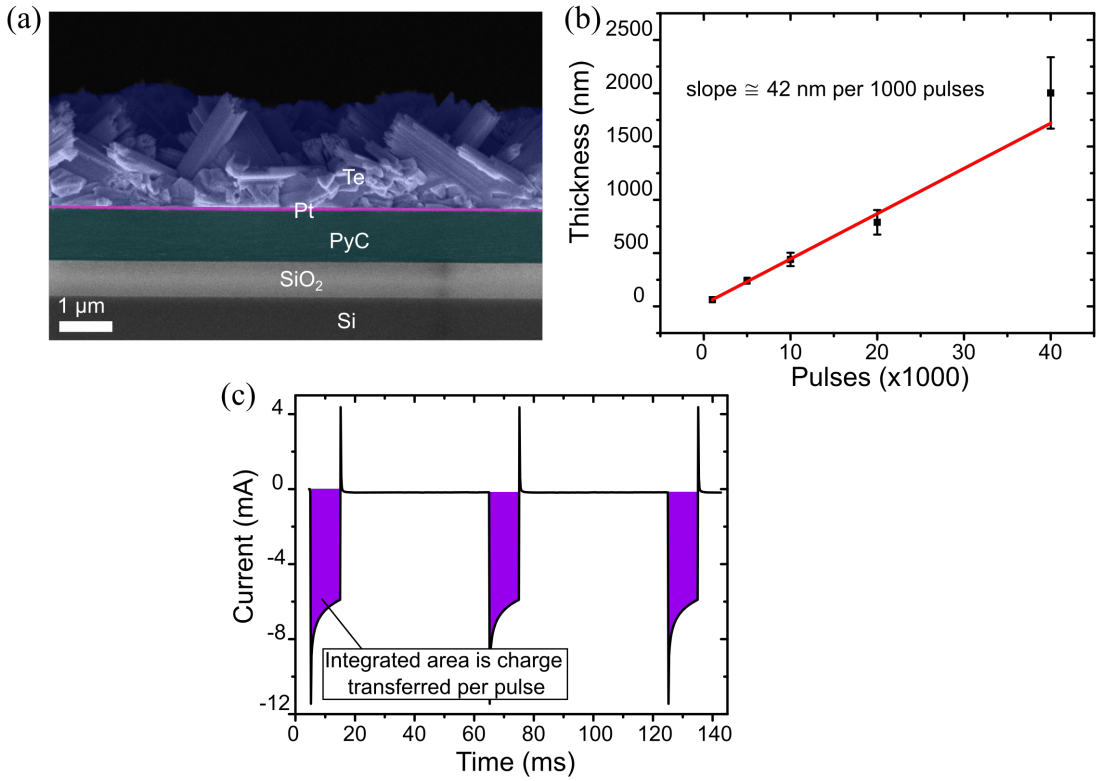


Figure 6.8: (a) SEM image along the break of a sample with the PyC, Pt and Te layers highlighted. (b) Plot of the number of pulses of Te deposited during electrodeposition versus the the thickness of the Te layer as measured by SEM. (c) Section of a typical current vs time plot of electrodeposition of Te on Pt.

The Te quantity was varied by changing the number of pulses applied during the electrodeposition.

How the Te layer thickness varied with number of applied pulses was found by cleaving the wafers and measuring the Te film thickness along the break with SEM. Figure 6.8 shows a typical SEM image of a cleaved wafer, along with the scatter plot of the Te thickness versus number of pulses. From the slope, an approximate relation of 1000 pulses giving 42 nm of Te was extracted. While this gives the approximate thickness of the Te film, since the film is porous, it does not give an accurate measure of the amount of Te present.

Shown in Figure 6.8(c) is a plot of the current vs time plot for three typical pulses during the electrodeposition of Te on Pt. Taking the integrated area under each peak gives the charge transferred through the cell for each pulse.

By multiplying by the number of pulses, an estimate for the charge transfer during a deposition can be obtained. Using Equation 1.5, it is then possible to calculate approximately the number of moles of Te deposited on a sample during the deposition. Finally, a thickness of the expected Te film can be found by using the bulk density of Te. This method predicts a Te layer thickness of 33 nm/1000 pulses. While there are associated errors with this calculation, it is reassuring that it is quite close to the thickness measured by SEM of 42 nm/1000 pulses. The predicted thickness being lower makes sense as the Te film that is electrodeposited is porous, and so less dense than bulk Te. Taking the ratio of these thicknesses gives an estimate for the density of the Te films of 75 - 80% that of bulk Te.

This calculation enables the approximate ratio of Te to Pt in samples to be calculated. For a film of 20 nm Pt and 10,000 pulses the ratio of Pt:Te is approximately 1:8, meaning that there is a four times excess of Te present on the sample.

Figure 6.9(a) shows the effect of the quantity of Pt and Te present on the sample on the percentage of the surface covered by $PtTe_2$ in the final films. This is measured by finding the average coverage of multiple SEM images of each film. In the range examined, the coverage varies between 15%(blue) and 100%(red), indicating the strong effect these parameters have on the growth. The surface coverage is highest when the ratio of Te:Pt is low. There are a number of potential driving forces for this behaviour. Naturally, the surface energy of the liquid $PtTe_x$ alloy would be reduced by dewetting from the surface and forming beads or droplets. The difference between $PtTe_2$ and the other telluride TMDs is that the adhesion of the Pt to the PyC substrate is low. This implies that there would be little resistance to the liquid $PtTe_x$ alloy beading up into a more energetically favourable shape during growth. With more Te present these droplets would tend to be larger, also leaving larger areas without any $PtTe_2$ and so reducing

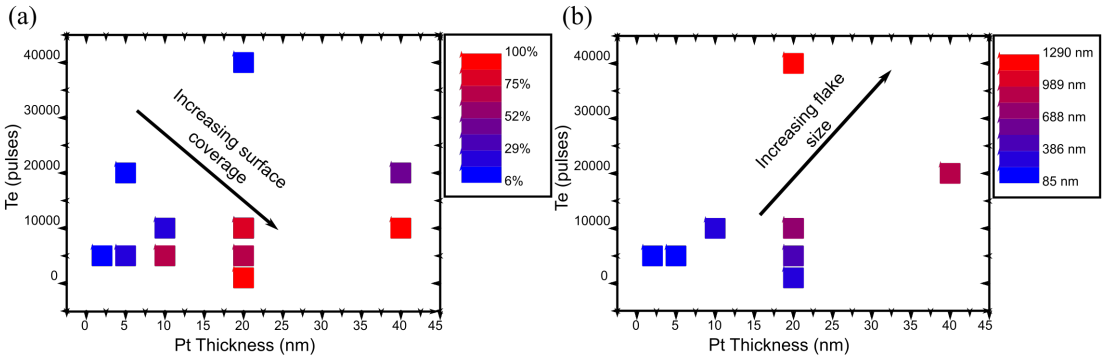


Figure 6.9: (a) Plot of the variation in surface coverage of $PtTe_2$ with thickness of Pt layer and number of Te pulses during electrodeposition. (b) Plot of the effect of the same parameters on the average lateral flake size in the $PtTe_2$ films. This data making up these graphs is shown in Table 6.2.

the surface coverage.

The dewetting would also be influenced by the stronger interlayer bonds in $PtTe_2$ than are present in the other telluride TMDs.[271,272] The distances between Te atoms in adjacent $PtTe_2$ layers are comparable to those for in trigonal and monoclinic tellurium (3.4Å vs 3.5Å), indicating that it would not be accurate to regard the interlayer interactions as purely Van der Waals.[21] This would encourage the growth of thick flakes with small lateral dimensions.

Analysis of how the same parameters, Pt and Te amounts, affect the size of $PtTe_2$ flakes formed is shown in Figure 6.9(b). The average flake length (average largest lateral dimension of flakes as measured by SEM) increases when the amount of Te and Pt are both high. The flakes on films grown from 20 nm Pt and 40,000 pulses of Te have an average length of ~1.3 μm. The high amounts of Pt and Te allow for larger crystal growth. This is further enhanced however, as the reduced surface coverage seen with high Pt and Te amounts would increase reactant quantities in certain areas. The data from Figure 6.9 (a) and (b) is shown in Table 6.2.

These morphology results are similar to other reports, where $PtTe_2$ was found to be more inclined towards growth in small thick flakes than TMDs such as MoS_2.[60,132] This dewetting would limit the range of films that can be examined

Table 6.2: Morphology data for $PtTe_2$ films

Pt deposition (nm)	Te depoisition (pulses)	Surface coverage	Largest lateral dimension (nm)
2	5000	12%	90
5	5000	21%	201
5	20000	7%	-
10	10000	22%	308
10	5000	75%	-
20	1000	98%	352
20	5000	68%	427
20	10000	17%	943
20	10000	79%	-
20	10000	49%	810
20	40000	7%	1285
40	20000	44%	902
40	10000	93%	-

for applications where uniform films would be required. Low Te amounts can be used to ensure full surface coverage, but would require careful implementation to ensure films are converting fully down through the Pt layer and would also limit the size of the $PtTe_2$ grains in the films. Another potential solution would be to develop a substrate on which Pt has stronger adhesion, or even use a adhesive metal layer such as Ti beneath the Pt.

6.8 Application as an electrocatalyst

There has been little work on the electrocatalytic properties of $PtTe_2$ published thus far. The few papers that have been published, have demonstrated efficient catalysis for the HER and ORR.[79,266,267] This fits with the expectation of semimetallic 1T phase TMDs showing promising electrocatalytic results. The polycrystalline nature of the films grown in this work could be expected to further enhance these properties.

Although certainly interesting to study, it is important to bear in mind, when touting $PtTe_2$ for catalytic applications, that Pt is an excellent catalyst of numer-

ous reactions in its own right. It is also an extremely expensive material and as such, any application of $PtTe_2$ as a catalyst would need to justify the cost of both the raw Pt and the processing. It should be noted however, that $PtTe_2$ is only ∼43% Pt by weight, meaning any results that are close to matching Pt would be potentially economically viable if it could be grown efficiently on a large scale.

6.8.1 Hydrogen Evolution Reaction

Here $PtTe_2$ films were examined as electrocatalysts for the HER. As discussed in Section 6.7, the films of $PtTe_2$ tended to dewet from the substrate and not provide full, or uniform, surface coverage under a number of experimental conditions. For this reason, there was a limited range of parameters under which the films could be grown and used for this application. For this reason only films grown from 20 nm Pt with 5,000 pulses of Te and 10 nm Pt with 2,500 pulses of Te were examined in this section.

Shown in Figure 6.10(a) are the LSV results for a 10 nm $PtTe_2$ film, a 30 nm Pt film and for bare PyC. The $PtTe_2$ film shows strong electrocatlytic behaviour with an onset potential (OP required to measure a current density of 0.5 mA cm^{-2}) of -219 mV. This onset potential demonstrates that $PtTe_2$ films are much more active than either the $MoTe_2$ or WTe_2 films in the previous chapters. The PyC shows essentially no activity in this voltage window, while the Pt control shows an onset potential of ∼-30 mV.

The Tafel plot for each of these is shown in Figure 6.10(b). The Tafel slope of the $PtTe_2$ film was 85 mV dec^{-1}. The Pt film shows the expected very low slope of 38 mV dec^{-1}, while the PyC again shows little activity with a high Tafel slope. This analysis has shown that $PtTe_2$ films grown in this manner are an effective catalyst of the HER due to the evolution of substantial amounts of H_2 at relatively low overpotentials.

A common metric used in literature to compare the behaviour of electrocata-

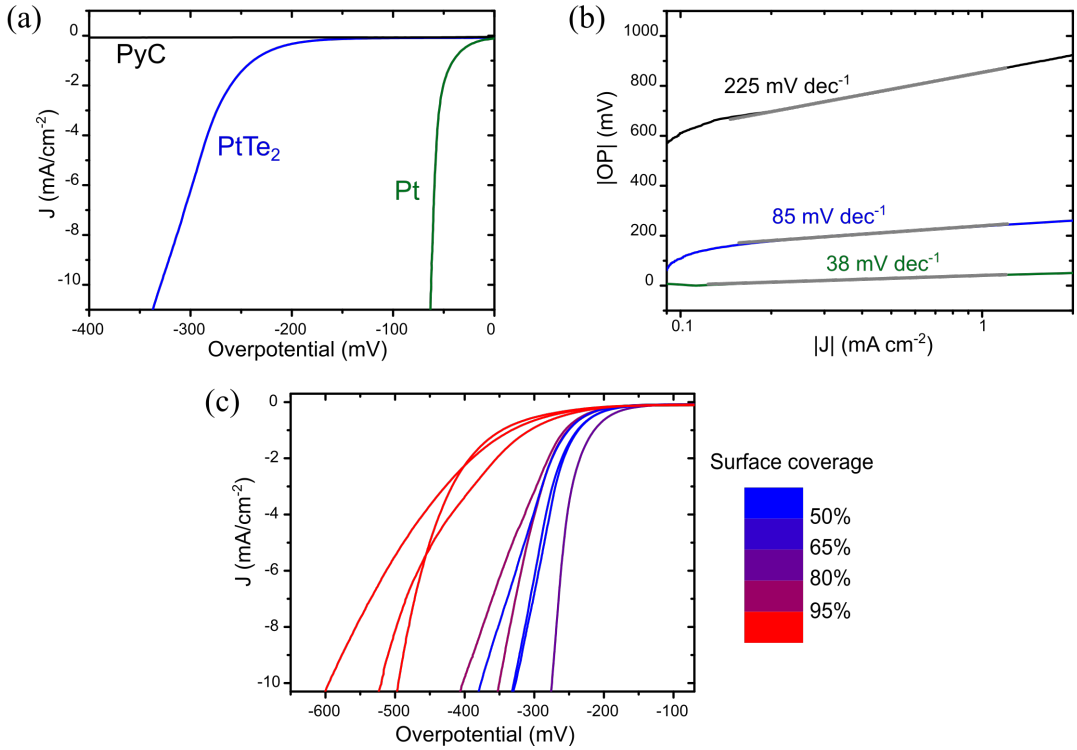


Figure 6.10: (a) LSV of a 20 nm $PtTe_2$ film, Pt film and PyC for the HER (b) Tafel plot of the same samples. (c) LSV of a number of $PtTe_2$ films, colour coded by their measured surface coverage.

lysts of the HER is the OP @ 10 mA cm^{-2}. Using this metric the $PtTe_2$ electrodes measured in this work were also found to perform well, requiring an OP of ∼ -330 mV to measure a current density of 10 mA cm^{-2}. Chia *et al.* examined the suitability of PtS_2, $PtSe_2$ and $PtTe_2$ as catalysts for the HER, concluding that $PtTe_2$ was the best performing. They reported that an OP of -530 mV @ 10 mA cm^{-2} for $PtTe_2$. This is much higher than the films examined in this work, indicating the better catalytic performance of these films. This may be due to the polycrystalline nature of the films, as edge sites and defects have previously been shown to offer improved catalytic performance for Pt based TMDs.[268,272,273]

A number of films with different levels of $PtTe_2$ surface coverage were tested to examine whether this had any influence on their catalytic behaviour. The LSVs of these films are shown in Figure 6.10(c), with each LSV colour coded by the percentage of surface coverage. While this is a reasonably small sample size,

the general trend appears to indicate that it is films with a lower surface coverage of $PtTe_2$ that perform better. Initially this would seem quite counter intuitive as less surface coverage implies that the samples have less of the surface covered with catalytically active $PtTe_2$, with the remainder being inactive PyC. It has already been shown in Section 6.7 that there is not any significant amount of elemental Pt on the surface of these samples. However, samples with lower surface coverage tend to have thicker flakes. This may in turn lead to a greater roughness and density of $PtTe_2$ edge sites, with these having been previously shown to be the most catalytically active sites in TMDs.[272,273] Further investigations, involving measurements of the real surface area of the films, would be required to confirm this.

6.8.2 Oxygen Reduction Reaction

Following the promising HER results demonstrated, the $PtTe_2$ films were examined for their catalytic activities towards the ORR. Previous reports have highlighted that $PtTe_2$ shows strong catalytic behaviour, very close to Pt/C, for this system.

LSV analysis of a typical $PtTe_2$ film is shown in Figure 6.11(a), also shown is the behaviour of a PyC and Pt film. The blue and red curves, labelled $PtTe_2$ LSV 1 and LSV 2 respectively, are two subsequent LSVs of the same $PtTe_2$ film, with LSV 2 performed immediately after LSV 1. There is a dramatic improvement in catalytic activity of the film after the first run, which itself did not show strong catalysis of the ORR. The green trace is the response measured by the $PtTe_2$ film after the electrolyte has been purged with Ar for 20 minutes. The absence of any peak in this case confirms that the measured values for the other films are due to the ORR. The response for Pt and PyC electrodes is also shown. Pt is an efficient catalyst for ORR, while the the reaction requires a much higher OP when the PyC electrode is being used.

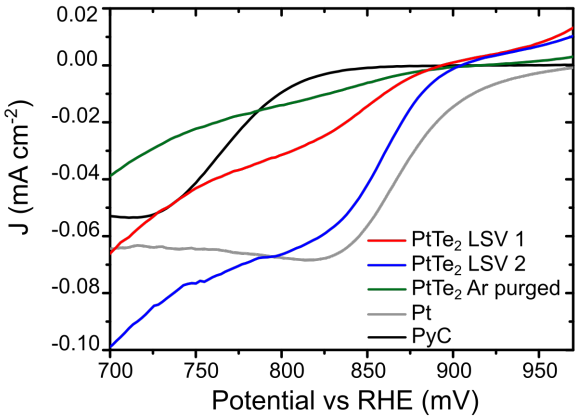


Figure 6.11: (a) LSV of samples of $PtTe_2$,Pt and PyC with and without Ar purge of electrolyte.

The half-wave potential, $E_{1/2}$ allows the catalytic activity of films to be quantified. This is the potential at which the current due to the ORR is equal to half of the diffusion limited ORR current. A value closer to the thermodynamic potential of oxygen reduction is preferable.

Examining the blue $PtTe_2$ LSV (labelled $PtTe_2$ LSV 2), its $E_{1/2}$ was found to be 862 mV, compared to 770 mV for PyC and 876 mV for the Pt film. The thermodynamic potential for oxygen reduction is 1.23V (vs. RHE), having an $E_{1/2}$ value close to this implies the catalyst is effective because the OP required to catalyse the reaction is low. The $PtTe_2$ film has an $E_{1/2}$ only 15 mV different from that of Pt, implying a very similar level of catalytic activity. This measurement is consistent with the reported values in literature, where the $PtTe_2$ was found to less active than Pt/C by only 18 mV, though the metric used to measure the activity in that paper was slightly different.[79]

The dramatic improvement in the $PtTe_2$ electrode between LSV 1 and LSV 2 is striking. This change was investigated by performing XPS on the samples after the ORR measurements. This is shown in Figure 6.12. It is clear that there are only two states of Pt present in the XPS spectrum - Pt bound to Te and Pt bound to oxygen. This is similar to the spectrum of the as grown $PtTe_2$ films seen in Section 6.4. It was found that after the HER almost 50% of the Te on the

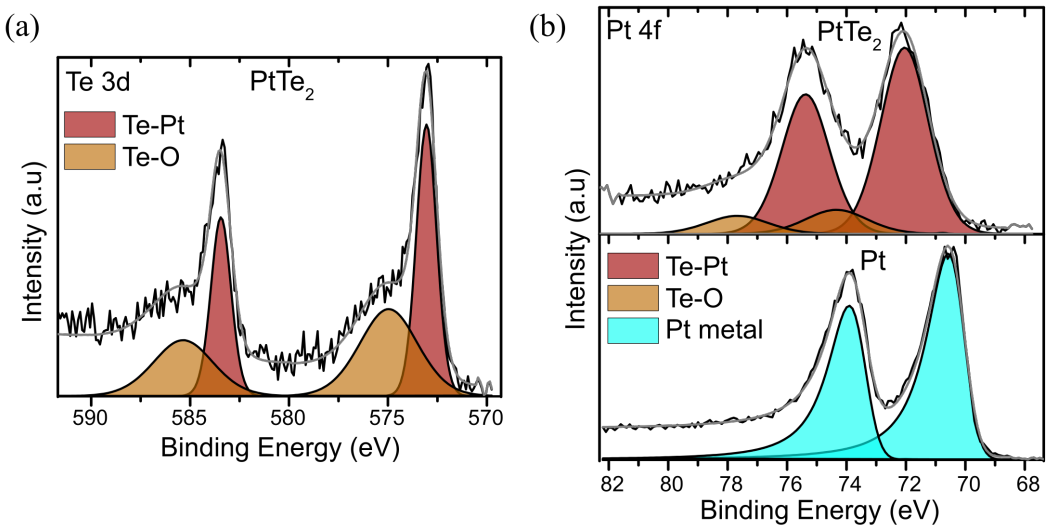


Figure 6.12: (a) Te 3d core-level spectrum of $PtTe_2$ film measured after ORR (b) Pt 4f core-level spectra of $PtTe_2$ after the ORR measurements. A spectra of the Pt 4f level of the elemental Pt film is also shown for comparison. The results of this XPS analysis are shown in Table 6.1

surface was in the form of oxide, while for the Pt about 14% of the atoms were bound to oxygen. This increase in oxide is notable, but it is the significant change in the stoichiometry of the $PtTe_2$ that is most surprising. The stoichiometry of the the '$PtTe_2$' is in fact $PtTe_{0.5}$, details given in Table 6.1. This is a huge change from before the ORR measurements and indicates that the sample is now very Pt rich on the surface, to the extent that it could not be described it as $PtTe_2$. Despite this, there was no indication of Pt in an elemental state found on the surface within the limits of detection. This may imply a single sub-stoichiometric $PtTe_x$ is forming on the surface during the electrochemical measurements and that this material is much more electrocatalytically active than as synthesised $PtTe_2$. PtO_x has also been shown to be catalytically active towards the HER and so the high level of oxidation post ORR must also be considered.[274,275] The ORR results therefore require further investigation before any firm conclusions can be drawn.

Previously published work by Rosli *et al.*, in which they study $PtTe_2$ as an electrocatalyst for the ORR, does not mention observing similar Te loss during

measurements.[79] The CVT crystals used in that study however are likely to be less prone to degradation than the polycrystalline films used in this thesis, which have a higher density of under-coordinated edge sites. Interestingly, XPS measurements of $PtTe_2$ crystals in other works by the same group do indicate a Te deficiency, perhaps showing that it is not solely an issue with the films examined here.[266]

6.9 Conclusion

In this chapter the growth and characterisation of $PtTe_2$ thin films was outlined. The fabrication process for $PtTe_2$ was similar to that described for the other telluride TMDs, predeposition of Pt and Te layers that are then reacted in a furnace under N_2 atmosphere. The conversion was successful using a growth time of 90 minutes, at temperatures between 450°C and 650°C. This is the lowest growth temperature for $PtTe_2$ currently reported, with all others involving temperatures above 700 °C. This could facilitates the growth on a wide variety of substrate, including flexible films such as polyimide.

Raman characterisation showed typical spectra for bulk-like $PtTe_2$ for all films. There was no significant peak shifting observed, however the intensity ratio of the two primary peaks was found to vary with thickness. This it thought to be likely due to the angle of the flakes with respect to the surface, however further work would be required to verify this. XPS showed phase-pure 1T $PtTe_2$ with metallic character. The surfaces of the films were found to be oxidised to about 10% indicating stability similar to that of the 1T' $MoTe_2$ films discussed in Chapter 4. XRD showed the expected peaks of $PtTe_2$ and indicated its polycrystalline nature.

The morphology of the films was found to be discrete single crystalline flakes of $PtTe_2$. These flakes are much more 3D in nature that those of $MoTe_2$ or WTe_2, grown by the same method. The $PtTe_2$ flakes had lateral dimensions of between

200 nm and 1 μm and thicknesses of between 100 nm and 400 nm. Analysing the variation in the morphology showed that the flakes increased in size with increasing Pt and Te amount present. This did however also result in a reduction in surface coverage, as the Pt and Te tended to dewet from the PyC substrate during growth. This was as a result of the poor adhesion between the Pt and the substrate and the stronger interlayer bonding in $PtTe_2$ encouraging thicker flake growth.

Finally the $PtTe_2$ films were examined as electrocatalyts of the HER and the ORR. The films showed strong catalytic behaviour for both. The $PtTe_2$ films showed more activity towards the HER than either $MoTe_2$ or WTe_2 films, along with stronger performance than previously reported works on CVT $PtTe_2$. For the ORR the films showed very strong catalytic behaviour, but only after an initial LSV was completed. This change was investigated with XPS after the catalytic measurements and it was found that while there was no evidence of elemental Pt on the surface, the samples were very Te deficient to be described as $PtTe_2$. For this reason, although promising, there is an caveat beside the performance of these samples towards the ORR.

7

Conclusions & Future Work

In this thesis a new, scalable method for the fabrication of telluride TMDs was developed and thoroughly examined. Specifically, the TAC growth method, previously used to grow sulfide and selenide TMDs, was adapted by depositing both the transition metal and chalcogen layers on the substrate prior to the furnace step. The motivation for this was two-fold. Firstly, there is currently a high level of interest in telluride TMDs, making investigations of potential synthesis routes a worthwhile endeavour. Despite this, the majority of studies on these have been carried out on CVT grown crystals and mechanically exfoliated flakes. These methods are time and energy intensive, along with not being scalable. This creates a pressing need for scalable growth methods to be investigated. Secondly, the standard TAC method, which does produce large-area films, requires large quantities of vaporised chalcogen; this is not ideal in the case of Te as it results in potential for exposure to toxic tellurium compounds.

In Chapter 3 the production of TMD films was explored by the standard TAC method. Films of MoS_2, $MoSe_2$, WS_2 and WSe_2 were grown and characterised. The rough polycrystalline morphology of the films, with grains on the order of tens of nanometres, was highlighted through AFM and SEM. Electrical investigations revealed that the resistivity values of the WSe_2 films were significantly lower than

any of the other films and well below that expected for bulk WSe_2. This result, along with the XPS analysis that indicated some elemental W present in the film, led to the conclusion that the W films were not fully converting to WSe_2.

The TAC films were then combined with the goal of manufacturing heterojunction or p-n junction diodes. Neither the sulfide, nor selenide, film combinations yielded any rectifying diode behaviour. This was concluded to be due to the rough, polycrystalline nature of the films inhibiting the formation of a clear junction between the films. Along with this, alloying between the films during growth, indicated by Raman analysis, would have prevented the formation of a sharp interface and depletion region between the films.

Having obtained an understanding of the TAC method, the growth of telluride TMDs was then examined through the modification of this process. To avoid high amounts of vaporised chalcogen during the growth, the Te was electrodeposited onto the substrate prior to the furnace step. This process was optimised by using a conductive PyC layer beneath the metal, and by using a pulsed rather than DC deposition. Along with pre-depositing the Te, the furnace run was conducted near atmospheric pressure (∼700 mbar) to maintain a high concentration of Te during the growth.

This modified TAC method allowed the successful growth of 1T' $MoTe_2$, T_d WTe_2 and 1T $PtTe_2$ films. The films of each material were found to grow between 450 °C and 650 °C. The lower temperature limit was judged to be defined by the melting point of Te, while the upper was due to the rapid vaporisation of the Te at higher temperatures inhibiting the growth. Raman and XRD of each showed bulk-like spectra, confirming the successful growth of the desired materials. It is interesting to note that all three telluride TMD grow in similar, relatively low, temperature ranges. This shows the potential promise for this growth method to be used with a much wider range of substrates and processes than CVT. The shorter growth times involved and ability to tune the morphology are other

significant advantages.

The XPS analysis of $MoTe_2$ and $PtTe_2$ both showed metallic, single-phase TMDs, with approximately 15% of the surface atoms in the form of oxides. The WTe_2 films were more susceptible to oxidation, however sputter XPS indicated that this oxidation was self-limiting and did not extend into the bulk of the material.

The solid-liquid growth interface was found to produce film morphologies significantly different from standard TAC. The telluride TMDs grown by the modified TAC method had larger grain sizes. $MoTe_2$ films consisted of crystalline flakes on the order of hundreds of nanometres, while WTe_2 films showed two morphologies on the surface, areas of large (1 - 10 μm) distinct flakes surrounded by smaller crystals. This behaviour was likely caused by the tendency of Te to dewet from the W surface during the growth. During the $PtTe_2$ growth both the Pt and Te are thought to dewet from the substrate, resulting in flakes with lateral dimensions below a micrometre and thicknesses of between 100 nm and 400 nm. With all dimensions within about an order of magnitude of each other, these $PtTe_2$ flakes cannot be considered 2D materials. This is as a result of the relatively strong interlayer bonds in $PtTe_2$ in comparison to other TMDs.

TEM images of individual WTe_2 flakes confirmed that they consisted of the T_d phase and showed that each was a single crystal with the W chains along the longest flake axis. Initial electrical measurements of individual flakes were promising, indicating high conductivities in line with previous reports for WTe_2.

All of the films were also investigated for electrocatalytic applications. The WTe_2 films did not show strong electrocatlysis of the HER. The performance of $MoTe_2$ was superior, comparing well with other reports of HER catalysis using 1T' $MoTe_2$. It was further found that thicker, rougher films showed improved behaviour. These films have the added advantage of being grown in a scalable manner, at a relatively low temperature, directly on the current collector.

The $PtTe_2$ films were examined as electrocatalysts for both the HER and ORR. The HER and ORR results showed very strong behaviour. XPS investigation of the $PtTe_2$ films after the ORR measurements indicated that the films were losing Te during the electrochemical measurements. This may mean that the catalytic behaviour is due to the formation of elemental Pt states on the surface.

Overall this thesis has demonstrated an effective method to grow films of $MoTe_2$, WTe_2 and $PtTe_2$. These were grown over large areas, at relatively low temperatures and short growth times. The films were thoroughly characterised and their potential applicability highlighted, primarily through electrocatalytic measurements.

7.1 Future work

The growth method used for the telluride TMDs in this thesis was shown to be quite versatile, with three TMDs fabricated with only minor variation in the process. Therefore, a natural next step would be to expand it to grow other TMDs. Although the sulfide and selenide TMDs can be produced by the standard TAC method, producing them from pre-deposited metal and chalcogen layers may yield films with much larger grain sizes. It would be then interesting to compare the films grown by the different methods. Aside from this there is potential to grow many other difficult to fabricate TMDs using this method, such as $PdTe_2$, or $NbTe_2$. A further potential study would be creating alloys such as $MoWTe_2$, which would be interesting for phase-change applications. This could be achieved through deposition of alternating sputtered layers of Mo and W, or using controlled composition metal targets, prior to Te deposition.

Narrowing focus to only the materials examined within this thesis still leaves a large amount of scope for further work. Firstly, a wider examination of the parameter space to investigate heating and cooling rates may yield more insights into the crystal growth and nucleation process. Attempting to convert films in a

sealed vessel could confirm whether the upper temperature limit of 650 °C is due to loss of Te during the growth. This experiment may also shed light on why the 2H phase of $MoTe_2$ does not readily grow using this system. Further experiments involving cross-sectional TEM would be valuable in determining more precisely the quantities of Te necessary to fully convert films and better characterise the voids seen in the $MoTe_2$ films.

With regards to application of the grown TMDs, there remains a wide variety of potential avenues of research. The promising initial electrical measurements on WTe_2 warrant further investigation, with indications from TEM that their single-crystalline nature could allow magnetoresistance measurements. A more in-depth study into the variation in resistance with temperature could also prove insightful.

The development of a method to efficiently deposit Te on patterned samples through some form of masking would open a range of opportunities. This would allow simple patterning of devices, akin to the shadow masking discussed in Chapter 3. A way of controlling the dewetting of the films during the growth process, through substrate choice or interface engineering, would also be highly beneficial for subsequent studies of electrocatalytic applications.

Bibliography

[1] N. Taniguchi, *Proceedings of the International Conference on Production Engineering, Tokyo, Part II*, 1974.

[2] P. Schulz, *Ciencia Hoje*, 2013, **308**, 1.

[3] M. José-Yacamán, L. Rendón, J. Arenas and M. C. S. Puche, *Science*, 1996, **273**, 223–225.

[4] I. Freestone, N. Meeks, M. Sax and C. Higgitt, *Gold Bulletin*, 2007, **40**, 270–277.

[5] G. Binnig, H. Rohrer, C. Gerber and E. Weibel, *Applied Physics Letters*, 1982, **40**, 178–180.

[6] G. Binnig and H. Rohrer, *Surface Science*, 1983, **126**, 236–244.

[7] P. Harris, *C*, 2018, **4**, 4.

[8] H. W. Kroto, J. R. Heath, S. C. O'Brien, R. F. Curl and R. E. Smalley, *Nature*, 1985, **318**, 162–163.

[9] S. Iijima, *Nature*, 1991, **354**, 56–58.

[10] A. M. Rao, *Science*, 1997, **275**, 187–191.

[11] K. S. Novoselov, *Science*, 2004, **306**, 666–669.

[12] K. F. Mak, C. Lee, J. Hone, J. Shan and T. F. Heinz, *Physical Review Letters*, 2010, **105**, 136805.

[13] G. R. Bhimanapati, Z. Lin, V. Meunier, Y. Jung, J. Cha, S. Das, D. Xiao, Y. Son, M. S. Strano, V. R. Cooper, L. Liang, S. G. Louie, E. Ringe, W. Zhou, S. S. Kim, R. R. Naik, B. G. Sumpter, H. Terrones, F. Xia, Y. Wang, J. Zhu, D. Akinwande, N. Alem, J. A. Schuller, R. E. Schaak, M. Terrones and J. A. Robinson, *ACS Nano*, 2015, **9**, 11509–11539.

[14] S. Helveg, J. V. Lauritsen, E. Lægsgaard, I. Stensgaard, J. K. Nørskov, B. S. Clausen, H. Topsøe and F. Besenbacher, *Physical Review Letters*, 2000, **84**, 951–954.

[15] R. F. Frindt, *Journal of Applied Physics*, 1966, **37**, 1928–1929.

[16] W. Choi, N. Choudhary, G. H. Han, J. Park, D. Akinwande and Y. H. Lee, *Materials Today*, 2017, **20**, 116–130.

[17] M. Samadi, N. Sarikhani, M. Zirak, H. Zhang, H.-L. Zhang and A. Z. Moshfegh, *Nanoscale Horizons*, 2018, **3**, 90–204.

[18] J. Wilson and A. Yoffe, *Advances in Physics*, 1969, **18**, 193–335.

[19] S. K. C, C. Zhang, S. Hong, R. M. Wallace and K. Cho, *2D Materials*, 2015, **2**, 035019.

[20] R. Wang, Y. Yu, S. Zhou, H. Li, H. Wong, Z. Luo, L. Gan and T. Zhai, *Advanced Functional Materials*, 2018, **28**, 1802473.

[21] D. Dai, H.-J. Koo, M.-H. Whangbo, C. Soulard, X. Rocquefelte and S. Jobic, *Journal of Solid State Chemistry*, 2003, **173**, 114–121.

[22] X. Chia and M. Pumera, *Chemical Society Reviews*, 2018, **47**, 5602–5613.

[23] K.-A. N. Duerloo, Y. Li and E. J. Reed, *Nature Communications*, 2014, **5**, 4214.

[24] P. Song, C. Hsu, M. Zhao, X. Zhao, T.-R. Chang, J. Teng, H. Lin and K. P. Loh, *2D Materials*, 2018, **5**, 031010.

[25] A. Castellanos-Gomez, V. Singh, H. S. J. van der Zant and G. A. Steele, *Annalen der Physik*, 2014, **527**, 27–44.

[26] J. Wu, Y. Chen, J. Wu and K. Hippalgaonkar, *Advanced Electronic Materials*, 2018, **4**, 1800248.

[27] C. Gong, Y. Zhang, W. Chen, J. Chu, T. Lei, J. Pu, L. Dai, C. Wu, Y. Cheng, T. Zhai, L. Li and J. Xiong, *Advanced Science*, 2017, **4**, 1700231.

[28] Q. H. Wang, K. Kalantar-Zadeh, A. Kis, J. N. Coleman and M. S. Strano, *Nature Nanotechnology*, 2012, **7**, 699–712.

[29] Y. Liu, N. O. Weiss, X. Duan, H.-C. Cheng, Y. Huang and X. Duan, *Nature Reviews Materials*, 2016, **1**, 16042.

[30] X. Duan, C. Wang, A. Pan, R. Yu and X. Duan, *Chemical Society Reviews*, 2015, **44**, 8859–8876.

[31] G. Fiori, F. Bonaccorso, G. Iannaccone, T. Palacios, D. Neumaier, A. Seabaugh, S. K. Banerjee and L. Colombo, *Nature Nanotechnology*, 2014, **9**, 768–779.

[32] V. Podzorov, M. E. Gershenson, C. Kloc, R. Zeis and E. Bucher, *Applied Physics Letters*, 2004, **84**, 3301–3303.

[33] D. He, Y. Pan, H. Nan, S. Gu, Z. Yang, B. Wu, X. Luo, B. Xu, Y. Zhang, Y. Li and et al., *Applied Physics Letters*, 2015, **107**, 183103.

[34] Q. Wang, J. Lai and D. Sun, *Optical Materials Express*, 2016, **6**, 2313.

[35] K. F. Mak and J. Shan, *Nature Photonics*, 2016, **10**, 216–226.

[36] J. Shim, H.-Y. Park, D.-H. Kang, J.-O. Kim, S.-H. Jo, Y. Park and J.-H. Park, *Advanced Electronic Materials*, 2017, **3**, 1600364.

[37] F. H. L. Koppens, T. Mueller, P. Avouris, A. C. Ferrari, M. S. Vitiello and M. Polini, *Nature Nanotechnology*, 2014, **9**, 780–793.

[38] S. Bertolazzi, J. Brivio and A. Kis, *ACS Nano*, 2011, **5**, 9703–9709.

[39] P. Bollella, G. Fusco, C. Tortolini, G. Sanzò, G. Favero, L. Gorton and R. Antiochia, *Biosensors and Bioelectronics*, 2017, **89**, 152–166.

[40] C. Yim, K. Lee, N. McEvoy, M. O'Brien, S. Riazimehr, N. C. Berner, C. P. Cullen, J. Kotakoski, J. C. Meyer, M. C. Lemme and G. S. Duesberg, *ACS Nano*, 2016, **10**, 9550–9558.

[41] Z. Sun, N. Talreja, H. Tao, J. Texter, M. Muhler, J. Strunk and J. Chen, *Angewandte Chemie International Edition*, 2018, **57**, 7610–7627.

[42] C. R. Zhu, D. Gao, J. Ding, D. Chao and J. Wang, *Chemical Society Reviews*, 2018, **47**, 4332–4356.

[43] J. Hong, C. Jin, J. Yuan and Z. Zhang, *Advanced Materials*, 2017, **29**, 1606434.

[44] L. Tao, X. Duan, C. Wang, X. Duan and S. Wang, *Chemical Communications*, 2015, **51**, 7470–7473.

[45] D. Deng, K. S. Novoselov, Q. Fu, N. Zheng, Z. Tian and X. Bao, *Nature Nanotechnology*, 2016, **11**, 218–230.

[46] M. Velický and P. S. Toth, *Applied Materials Today*, 2017, **8**, 68–103.

[47] A. Dankert and S. P. Dash, *Nature Communications*, 2017, **8**, 16093.

[48] Y. K. Luo, J. Xu, T. Zhu, G. Wu, E. J. McCormick, W. Zhan, M. R. Neupane and R. K. Kawakami, *Nano Letters*, 2017, **17**, 3877–3883.

[49] W. Shi, J. Ye, Y. Zhang, R. Suzuki, M. Yoshida, J. Miyazaki, N. Inoue, Y. Saito and Y. Iwasa, *Scientific Reports*, 2015, **5**, 12534.

[50] Y. Wang, S. Li and J. Yi, *Scientific Reports*, 2016, **6**, 24153.

[51] C.-H. Lee, E. C. Silva, L. Calderin, M. A. T. Nguyen, M. J. Hollander, B. Bersch, T. E. Mallouk and J. A. Robinson, *Scientific Reports*, 2015, **5**, 10013.

[52] X. Li, S. Zhang and Q. Wang, *Nanoscale*, 2017, **9**, 562–569.

[53] T. A. Empante, Y. Zhou, V. Klee, A. E. Nguyen, I.-H. Lu, M. D. Valentin, S. A. N. Alvillar, E. Preciado, A. J. Berges, C. S. Merida, M. Gomez, S. Bobek, M. Isarraraz, E. J. Reed and L. Bartels, *ACS Nano*, 2017, **11**, 900–905.

[54] D. Rhodes, D. A. Chenet, B. E. Janicek, C. Nyby, Y. Lin, W. Jin, D. Edelberg, E. Mannebach, N. Finney, A. Antony, T. Schiros, T. Klarr, A. Mazzoni, M. Chin, Y. c Chiu, W. Zheng, Q. R. Zhang, F. Ernst, J. I. Dadap, X. Tong, J. Ma, R. Lou, S. Wang, T. Qian, H. Ding, R. M. Osgood, D. W. Paley, A. M. Lindenberg, P. Y. Huang, A. N. Pasupathy, M. Dubey, J. Hone and L. Balicas, *Nano Letters*, 2017, **17**, 1616–1622.

[55] Y. Qi, P. G. Naumov, M. N. Ali, C. R. Rajamathi, W. Schnelle, O. Barkalov, M. Hanfland, S.-C. Wu, C. Shekhar, Y. Sun, V. Süß, M. Schmidt, U. Schwarz, E. Pippel, P. Werner, R. Hillebrand, T. Förster, E. Kampert, S. Parkin, R. J. Cava, C. Felser, B. Yan and S. A. Medvedev, *Nature Communications*, 2016, **7**, 11038.

[56] N. Lu, C. Zhang, C.-H. Lee, J. P. Oviedo, M. A. T. Nguyen, X. Peng, R. M. Wallace, T. E. Mallouk, J. A. Robinson, J. Wang, K. Cho and M. J. Kim, *The Journal of Physical Chemistry C*, 2016, **120**, 8364–8369.

[57] B. E. Brown, *Acta Crystallographica*, 1966, **20**, 268–274.

[58] E. Torun, H. Sahin, S. Cahangirov, A. Rubio and F. M. Peeters, *Journal of Applied Physics*, 2016, **119**, 074307.

[59] Y. Kim, Y. I. Jhon, J. Park, J. H. Kim, S. Lee and Y. M. Jhon, *Nanoscale*, 2016, **8**, 2309–2316.

[60] L. Fu, D. Hu, R. G. Mendes, M. H. Rümmeli, Q. Dai, B. Wu, L. Fu and Y. Liu, *ACS Nano*, 2018, **12**, 9405–9411.

[61] S. Hao, J. Zeng, T. Xu, X. Cong, C. Wang, C. Wu, Y. Wang, X. Liu, T. Cao, G. Su, L. Jia, Z. Wu, Q. Lin, L. Zhang, S. Yan, M. Guo, Z. Wang, P. Tan, L. Sun, Z. Ni, S.-J. Liang, X. Cui and F. Miao, *Advanced Functional Materials*, 2018, **28**, 1803746.

[62] H.-J. Chuang, B. Chamlagain, M. Koehler, M. M. Perera, J. Yan, D. Mandrus, D. Tománek and Z. Zhou, *Nano Letters*, 2016, **16**, 1896–1902.

[63] Y. Chen, X. Wang, G. Wu, Z. Wang, H. Fang, T. Lin, S. Sun, H. Shen, W. Hu, J. Wang, J. Sun, X. Meng and J. Chu, *Small*, 2018, **14**, 1703293.

[64] H. Huang, J. Wang, W. Hu, L. Liao, P. Wang, X. Wang, F. Gong, Y. Chen, G. Wu, W. Luo, H. Shen, T. Lin, J. Sun, X. Meng, X. Chen and J. Chu, *Nanotechnology*, 2016, **27**, 445201.

[65] M. Kuiri, B. Chakraborty, A. Paul, S. Das, A. K. Sood and A. Das, *Applied Physics Letters*, 2016, **108**, 063506.

[66] S. Song, S.-Y. Kim, J. Kwak, Y. Jo, J. H. Kim, J. H. Lee, J.-U. Lee, J. U. Kim, H. D. Yun, Y. Sim, J. Wang, D. H. Lee, S.-H. Seok, T. il Kim, H. Cheong, Z. Lee and S.-Y. Kwon, *Advanced Science*, 2018, 1801370.

[67] A. N. Berger, E. Andrade, A. Kerelsky, D. Edelberg, J. Li, Z. Wang, L. Zhang, J. Kim, N. Zaki, J. Avila, C. Chen, M. C. Asensio, S.-W. Cheong, B. A. Bernevig and A. N. Pasupathy, *npj Quantum Materials*, 2018, **3**, 2.

[68] P. Li, Y. Wen, X. He, Q. Zhang, C. Xia, Z.-M. Yu, S. A. Yang, Z. Zhu, H. N. Alshareef and X.-X. Zhang, *Nature Communications*, 2017, **8**, 2150.

[69] W. Zhang, Q. Wu, L. Zhang, S.-W. Cheong, A. A. Soluyanov and W. Wu, *Physical Review B*, 2017, **96**, 165125.

[70] O. Pavlosiuk and D. Kaczorowski, *Scientific Reports*, 2018, **8**, 11297.

[71] X. Qian, J. Liu, L. Fu and J. Li, *Science*, 2014, **346**, 1344–1347.

[72] P. Lu, J.-S. Kim, J. Yang, H. Gao, J. Wu, D. Shao, B. Li, D. Zhou, J. Sun, D. Akinwande, D. Xing and J.-F. Lin, *Physical Review B*, 2016, **94**, 224512.

[73] M. N. Ali, J. Xiong, S. Flynn, J. Tao, Q. D. Gibson, L. M. Schoop, T. Liang, N. Haldolaarachchige, M. Hirschberger, N. P. Ong and R. J. Cava, *Nature*, 2014, **514**, 205–208.

[74] W.-D. Kong, S.-F. Wu, P. Richard, C.-S. Lian, J.-T. Wang, C.-L. Yang, Y.-G. Shi and H. Ding, *Applied Physics Letters*, 2015, **106**, 081906.

[75] F. C. Chen, H. Y. Lv, X. Luo, W. J. Lu, Q. L. Pei, G. T. Lin, Y. Y. Han, X. B. Zhu, W. H. Song and Y. P. Sun, *Physical Review B*, 2016, **94**, 235154.

[76] E. Revolinsky and D. Beerntsen, *Journal of Applied Physics*, 1964, **35**, 2086–2089.

[77] G. Zhang and Y.-W. Zhang, *Journal of Materials Chemistry C*, 2017, **5**, 7684–7698.

[78] A. Politano, G. Chiarello, C.-N. Kuo, C. S. Lue, R. Edla, P. Torelli, V. Pellegrini and D. W. Boukhvalov, *Advanced Functional Materials*, 2018, **28**, 1706504.

[79] N. F. Rosli, C. C. Mayorga-Martinez, N. M. Latiff, N. Rohaizad, Z. Sofer, A. C. Fisher and M. Pumera, *ACS Sustainable Chemistry & Engineering*, 2018, **6**, 7432–7441.

[80] Z. Gholamvand, D. McAteer, C. Backes, N. McEvoy, A. Harvey, N. C. Berner, D. Hanlon, C. Bradley, I. Godwin, A. Rovetta, M. E. G. Lyons, G. S. Duesberg and J. N. Coleman, *Nanoscale*, 2016, **8**, 5737–5749.

[81] J. C. McGlynn, I. Cascallana-Matías, J. P. Fraser, I. Roger, J. McAllister, H. N. Miras, M. D. Symes and A. Y. Ganin, *Energy Technology*, 2017, **6**, 345–350.

[82] J. Li, M. Hong, L. Sun, W. Zhang, H. Shu and H. Chang, *ACS Applied Materials & Interfaces*, 2017, **10**, 458–467.

[83] Y. Zhou, J. L. Silva, J. M. Woods, J. V. Pondick, Q. Feng, Z. Liang, W. Liu, L. Lin, B. Deng, B. Brena, F. Xia, H. Peng, Z. Liu, H. Wang, C. M. Araujo and J. J. Cha, *Advanced Materials*, 2018, **30**, 1706076.

[84] Y. Li, K.-A. N. Duerloo, K. Wauson and E. J. Reed, *Nature Communications*, 2016, **7**, 10671.

[85] M. Hong, J. Li, W. Zhang, S. Liu and H. Chang, *Energy & Fuels*, 2018, **32**, 6371–6377.

[86] H. P. Boehm, A. Clauss, G. O. Fischer and U. Hofmann, *Zeitschrift f r anorganische und allgemeine Chemie*, 1962, **316**, 119–127.

[87] A. K. Geim, *Physica Scripta*, 2012, **T146**, 014003.

[88] C. Tan, Z. Lai and H. Zhang, *Advanced Materials*, 2017, **29**, 1701392.

[89] J. N. Coleman, M. Lotya, A. Oâ€™Neill, S. D. Bergin, P. J. King, U. Khan, K. Young, A. Gaucher, S. De, R. J. Smith and et al., *Science*, 2011, **331**, 568–571.

[90] K. R. Paton, E. Varrla, C. Backes, R. J. Smith, U. Khan, A. Oâ€™Neill, C. Boland, M. Lotya, O. M. Istrate, P. King and et al., *Nat Mater*, 2014, **13**, 624–630.

[91] A. G. Kelly, T. Hallam, C. Backes, A. Harvey, A. S. Esmaeily, I. Godwin, J. Coelho, V. Nicolosi, J. Lauth, A. Kulkarni, S. Kinge, L. D. A. Siebbeles, G. S. Duesberg and J. N. Coleman, *Science*, 2017, **356**, 69–73.

[92] C. Backes, K. R. Paton, D. Hanlon, S. Yuan, M. I. Katsnelson, J. Houston, R. J. Smith, D. McCloskey, J. F. Donegan and J. N. Coleman, *Nanoscale*, 2016, **8**, 4311–4323.

[93] K. S. Novoselov and A. H. C. Neto, *Phys. Scr.*, 2012, **T146**, 014006.

[94] F. Bonaccorso and Z. Sun, *Optical Materials Express*, 2013, **4**, 63.

[95] R. D. Yoshio Nishi, *Handbook of Semiconductor Manufacturing Technology*, CRC Press, 2nd edn., 2007.

[96] M. Amani, M. L. Chin, A. G. Birdwell, T. P. O'Regan, S. Najmaei, Z. Liu, P. M. Ajayan, J. Lou and M. Dubey, *Applied Physics Letters*, 2013, **102**, 193107.

[97] Y.-H. Lee, X.-Q. Zhang, W. Zhang, M.-T. Chang, C.-T. Lin, K.-D. Chang, Y.-C. Yu, J. T.-W. Wang, C.-S. Chang, L.-J. Li and T.-W. Lin, *Advanced Materials*, 2012, **24**, 2320–2325.

[98] A. L. Elías, N. Perea-López, A. Castro-Beltrán, A. Berkdemir, R. Lv, S. Feng, A. D. Long, T. Hayashi, Y. A. Kim, M. Endo, H. R. Gutiérrez, N. R. Pradhan, L. Balicas, T. E. Mallouk, F. López-Urías, H. Terrones and M. Terrones, *ACS Nano*, 2013, **7**, 5235–5242.

[99] H. R. Gutiérrez, N. Perea-López, A. L. Elías, A. Berkdemir, B. Wang, R. Lv, F. López-Urías, V. H. Crespi, H. Terrones and M. Terrones, *Nano Letters*, 2013, **13**, 3447–3454.

[100] K. Kang, S. Xie, L. Huang, Y. Han, P. Y. Huang, K. F. Mak, C.-J. Kim, D. Muller and J. Park, *Nature*, 2015, **520**, 656–660.

[101] S. M. Eichfeld, L. Hossain, Y.-C. Lin, A. F. Piasecki, B. Kupp, A. G. Birdwell, R. A. Burke, N. Lu, X. Peng, J. Li, A. Azcatl, S. McDonnell, R. M. Wallace, M. J. Kim, T. S. Mayer, J. M. Redwing and J. A. Robinson, *ACS Nano*, 2015, **9**, 2080–2087.

[102] Y. Gong, J. Lin, X. Wang, G. Shi, S. Lei, Z. Lin, X. Zou, G. Ye, R. Vajtai, B. I. Yakobson, H. Terrones, M. Terrones, B. K. Tay, J. Lou, S. T. Pantelides, Z. Liu, W. Zhou and P. M. Ajayan, *Nature Materials*, 2014, **13**, 1135–1142.

[103] J. Chen, W. Zhou, W. Tang, B. Tian, X. Zhao, H. Xu, Y. Liu, D. Geng, S. J. R. Tan, W. Fu and K. P. Loh, *Chemistry of Materials*, 2016, **28**, 7194–7197.

[104] F. Wang, Z. Wang, C. Jiang, L. Yin, R. Cheng, X. Zhan, K. Xu, F. Wang, Y. Zhang and J. He, *Small*, 2017, **13**, 1604298.

[105] J. Wong, D. Jariwala, G. Tagliabue, K. Tat, A. R. Davoyan, M. C. Sherrott and H. A. Atwater, *ACS Nano*, 2017, **11**, 7230–7240.

[106] J. Creighton, *Introduction to Chemical Vapor Deposition (CVD)*, Chemical Vapor Deposition (ASM International), 2001.

[107] V. K. Kumar, S. Dhar, T. H. Choudhury, S. A. Shivashankar and S. Raghavan, *Nanoscale*, 2015, **7**, 7802–7810.

[108] Y. Zhan, Z. Liu, S. Najmaei, P. M. Ajayan and J. Lou, *Small*, 2012, **8**, 966–971.

[109] R. Gatensby, N. McEvoy, K. Lee, T. Hallam, N. C. Berner, E. Rezvani, S. Winters, M. O'Brien and G. S. Duesberg, *Applied Surface Science*, 2014, **297**, 139–146.

[110] G. Papari, C. Koral, T. Hallam, G. Duesberg and A. Andreone, *Materials*, 2018, **11**, 1613.

[111] M. O'Brien, N. McEvoy, C. Motta, J.-Y. Zheng, N. C. Berner, J. Kotakoski, K. Elibol, T. J. Pennycook, J. C. Meyer, C. Yim, M. Abid, T. Hallam, J. F. Donegan, S. Sanvito and G. S. Duesberg, *2D Materials*, 2016, **3**, 021004.

[112] R. Duffy, P. Foley, B. Filippone, G. Mirabelli, D. O'Connell, B. Sheehan, P. Carolan, M. Schmidt, K. Cherkaoui, R. Gatensby, T. Hallam, G. Duesberg, F. Crupi, R. Nagle and P. K. Hurley, *ECS Journal of Solid State Science and Technology*, 2016, **5**, Q3016–Q3020.

[113] Y.-C. Lin, W. Zhang, J.-K. Huang, K.-K. Liu, Y.-H. Lee, C.-T. Liang, C.-W. Chu and L.-J. Li, *Nanoscale*, 2012, **4**, 6637.

[114] J. H. Yu, H. R. Lee, S. S. Hong, D. Kong, H.-W. Lee, H. Wang, F. Xiong, S. Wang and Y. Cui, *Nano Letters*, 2015, **15**, 1031–1035.

[115] A. Tarasov, P. M. Campbell, M.-Y. Tsai, Z. R. Hesabi, J. Feirer, S. Graham, W. J. Ready and E. M. Vogel, *Advanced Functional Materials*, 2014, **24**, 6389–6400.

[116] T. Hallam, H.-Y. Kim, M. O'Brien, R. Gatensby, N. McEvoy and G. S. Duesberg, 2015 45th European Solid State Device Research Conference (ESSDERC), 2015.

[117] K. Lee, R. Gatensby, N. McEvoy, T. Hallam and G. S. Duesberg, *Advanced Materials*, 2013, **25**, 6699–6702.

[118] R. Gatensby, T. Hallam, K. Lee, N. McEvoy and G. S. Duesberg, *Solid-State Electronics*, 2016, **125**, 39–51.

[119] D. Kong, H. Wang, J. J. Cha, M. Pasta, K. J. Koski, J. Yao and Y. Cui, *Nano Letters*, 2013, **13**, 1341–1347.

[120] Y. Shi, H. Li and L.-J. Li, *Chemical Society Reviews*, 2015, **44**, 2744–2756.

[121] B. Predel, *Li-Mg ... Nd-Zr (Landolt-Börnstein: Numerical Data and Functional Relationships in Science and Technology - New Series) (Vol 5)*, Springer, 1997.

[122] T. Weber, J. C. Muijsers, J. H. M. C. van Wolput, C. P. J. Verhagen and J. W. Niemantsverdriet, *The Journal of Physical Chemistry*, 1996, **100**, 14144–14150.

[123] C.-R. Wu, X.-R. Chang, C.-H. Wu and S.-Y. Lin, *Scientific Reports*, 2017, **7**, 42146.

[124] B. Wang, S. Yang, C. Wang, M. Wu, L. Huang, Q. Liu and C. Jiang, *Nanoscale*, 2017, **9**, 10733–10740.

[125] S.-Y. Kim, J. Kwak, C. V. Ciobanu and S.-Y. Kwon, *Advanced Materials*, 2019, 1804939.

[126] L. Zhou, K. Xu, A. Zubair, X. Zhang, F. Ouyang, T. Palacios, M. S. Dresselhaus, Y. Li and J. Kong, *Advanced Functional Materials*, 2016, **27**, 1603491.

[127] K. Chen, Z. Chen, X. Wan, Z. Zheng, F. Xie, W. Chen, X. Gui, H. Chen, W. Xie and J. Xu, *Advanced Materials*, 2017, **29**, 1700704.

[128] J. H. Sung, H. Heo, S. Si, Y. H. Kim, H. R. Noh, K. Song, J. Kim, C.-S. Lee, S.-Y. Seo, D.-H. Kim, H. K. Kim, H. W. Yeom, T.-H. Kim, S.-Y. Choi, J. S. Kim and M.-H. Jo, *Nature Nanotechnology*, 2017, **12**, 1064–1070.

[129] T. Kim, H. Park, D. Joung, D. Kim, R. Lee, C. H. Shin, M. Diware, W. Chegal, S. H. Jeong, J. C. Shin, J. Park and S.-W. Kang, *Advanced Materials Interfaces*, 2018, **5**, 1800439.

[130] J. Zhou, F. Liu, J. Lin, X. Huang, J. Xia, B. Zhang, Q. Zeng, H. Wang, C. Zhu, L. Niu, X. Wang, W. Fu, P. Yu, T.-R. Chang, C.-H. Hsu, D. Wu, H.-T. Jeng, Y. Huang, H. Lin, Z. Shen, C. Yang, L. Lu, K. Suenaga, W. Zhou, S. T. Pantelides, G. Liu and Z. Liu, *Advanced Materials*, 2016, **29**, 1603471.

[131] C. H. Naylor, W. M. Parkin, Z. Gao, H. Kang, M. Noyan, R. B. Wexler, L. Z. Tan, Y. Kim, C. E. Kehayias, F. Streller, Y. R. Zhou, R. Carpick, Z. Luo, Y. W. Park, A. M. Rappe, M. Drndić, J. M. Kikkawa and A. T. C. Johnson, *2D Materials*, 2017, **4**, 021008.

[132] H. Ma, P. Chen, B. Li, J. Li, R. Ai, Z. Zhang, G. Sun, K. Yao, Z. Lin, B. Zhao, R. Wu, X. Tang, X. Duan and X. Duan, *Nano Letters*, 2018, **18**, 3523–3529.

[133] S. Hussain, S. A. Patil, D. Vikraman, N. Mengal, H. Liu, W. Song, K.-S. An, S. H. Jeong, H.-S. Kim and J. Jung, *Scientific Reports*, 2018, **8**, 29.

[134] L. Zhou, A. Zubair, Z. Wang, X. Zhang, F. Ouyang, K. Xu, W. Fang, K. Ueno, J. Li, T. Palacios, J. Kong and M. S. Dresselhaus, *Advanced Materials*, 2016, **28**, 9526–9531.

[135] L. Yang, W. Zhang, J. Li, S. Cheng, Z. Xie and H. Chang, *ACS Nano*, 2017, **11**, 1964–1972.

[136] J. Kwak, Y. Jo, S. Song, J. H. Kim, S.-Y. Kim, J.-U. Lee, S. Lee, J. Park, K. Kim, G.-D. Lee, J.-W. Yoo, S. Y. Kim, Y.-M. Kong, G.-H. Lee, W.-G. Lee, J. Park, X. Xu, H. Cheong, E. Yoon, Z. Lee and S.-Y. Kwon, *Advanced Materials*, 2018, **30**, 1707260.

[137] L. R. F. Allen J. Bard, *Electrochemical methods : fundamentals and applications*, John Wiley, 2nd edn., 2001.

[138] V. S. Saji and R. Cook, *Corrosion Protection and Control Using Nanomaterials*, WOODHEAD PUB, 2012.

[139] S. E. Group, *Instrumental methods in electrochemistry*, Horwood, 2001.

[140] A. C. Fisher, *Electrode Dynamics*, OXFORD UNIV PR, 1996.

[141] V. Richoux, S. Diliberto, C. Boulanger and J. Lecuire, *Electrochimica Acta*, 2007, **52**, 3053–3060.

[142] T. F. Jaramillo, K. P. Jorgensen, J. Bonde, J. H. Nielsen, S. Horch and I. Chorkendorff, *Science*, 2007, **317**, 100–102.

[143] J. D. Benck, T. R. Hellstern, J. Kibsgaard, P. Chakthranont and T. F. Jaramillo, *ACS Catalysis*, 2014, **4**, 3957–3971.

[144] M. Chhowalla, H. S. Shin, G. Eda, L.-J. Li, K. P. Loh and H. Zhang, *Nature Chemistry*, 2013, **5**, 263–275.

[145] D. Voiry, M. Salehi, R. Silva, T. Fujita, M. Chen, T. Asefa, V. B. Shenoy, G. Eda and M. Chhowalla, *Nano Letters*, 2013, **13**, 6222–6227.

[146] C. Tsai, K. Chan, J. K. Nørskov and F. Abild-Pedersen, *Surface Science*, 2015, **640**, 133–140.

[147] J. Xie, H. Zhang, S. Li, R. Wang, X. Sun, M. Zhou, J. Zhou, X. W. D. Lou and Y. Xie, *Advanced Materials*, 2013, **25**, 5807–5813.

[148] *Handbook of Fuel Cells*, ed. W. Vielstich, A. Lamm, H. A. Gasteiger and H. Yokokawa, John Wiley & Sons, Ltd, 2010.

[149] T. Shinagawa, A. T. Garcia-Esparza and K. Takanabe, *Scientific Reports*, 2015, **5**, 13801.

[150] J. R. Ferraro, *Introductory Raman Spectroscopy*, ACADEMIC PR INC, 2002.

[151] R. Egerton, *Physical Principles of Electron Microscopy*, Springer US, 2006.

[152] C. Sah, *Fundamentals of Solid State Electronics*, World Scientific, 1996.

[153] I. Schroeder, *Modelling of Interface Carrier Transport for Device Simulation*, Springer, 1994.

[154] A. K. Geim and I. V. Grigorieva, *Nature*, 2013, **499**, 419–425.

[155] S. Velez, D. Ciudad, J. Island, M. Buscema, O. Txoperena, S. Parui, G. A. Steele, F. Casanova, H. S. J. van der Zant, A. Castellanos-Gomez and et al., *Nanoscale*, 2015, **37**, 15442.

[156] D. S. Schulman, A. J. Arnold and S. Das, *Chemical Society Reviews*, 2018, **47**, 3037–3058.

[157] *The PN Junction Diode: Volume II*, ed. G. Neudeck and R. Pierret, Addison-Wesley, 1989.

[158] N. Flory, A. Jain, P. Bharadwaj, M. Parzefall, T. Taniguchi, K. Watanabe and L. Novotny, *Applied Physics Letters*, 2015, **107**, 123106.

[159] R. Cheng, D. Li, H. Zhou, C. Wang, A. Yin, S. Jiang, Y. Liu, Y. Chen, Y. Huang and X. Duan, *Nano Letters*, 2014, **14**, 5590–5597.

[160] Y. Sata, R. Moriya, T. Yamaguchi, Y. Inoue, S. Morikawa, N. Yabuki, S. Masubuchi and T. Machida, *Jpn. J. Appl. Phys.*, 2015, **54**, 04DJ04.

[161] M. Shanmugam, T. Bansal, C. A. Durcan and B. Yu, *Appl. Phys. Lett.*, 2012, **101**, 263902.

[162] J. Bardeen, *Physical Review*, 1947, **71**, 717–727.

[163] W. Monch, *Reports on Progress in Physics*, 1990, **53**, 221–278.

[164] J.-K. Huang, J. Pu, C.-L. Hsu, M.-H. Chiu, Z.-Y. Juang, Y.-H. Chang, W.-H. Chang, Y. Iwasa, T. Takenobu and L.-J. Li, *ACS Nano*, 2014, **8**, 923–930.

[165] M. Bosi, *RSC Adv.*, 2015, **5**, 75500–75518.

[166] D. Nečas and P. Klapetek, *Open Physics*, 2012, **10**, 181.

[167] A. Lennartson, *The Chemical Works of Carl Wilhelm Scheele*, Springer International Publishing, 2017.

[168] P. Joensen, R. Frindt and S. Morrison, *Materials Research Bulletin*, 1986, **21**, 457–461.

[169] J. Gusakova, X. Wang, L. L. Shiau, A. Krivosheeva, V. Shaposhnikov, V. Borisenko, V. Gusakov and B. K. Tay, *physica status solidi (a)*, 2017, **214**, 1700218.

[170] A. Kuc, N. Zibouche and T. Heine, *Physical Review B*, 2011, **83**, 245213.

[171] H.-P. Komsa and A. V. Krasheninnikov, *Physical Review B*, 2015, **91**, 125304.

[172] N. Kaushik, A. Nipane, F. Basheer, S. Dubey, S. Grover, M. M. Deshmukh and S. Lodha, *Applied Physics Letters*, 2014, **105**, 113505.

[173] K. Dolui, I. Rungger and S. Sanvito, *Physical Review B*, 2013, **87**, 165402.

[174] G.-S. Kim, S.-H. Kim, J. Park, K. H. Han, J. Kim and H.-Y. Yu, *ACS Nano*, 2018, **12**, 6292–6300.

[175] Y. Zhao, K. Xu, F. Pan, C. Zhou, F. Zhou and Y. Chai, *Advanced Functional Materials*, 2016, **27**, 1603484.

[176] P. Zhao, D. Kiriya, A. Azcatl, C. Zhang, M. Tosun, Y.-S. Liu, M. Hettick, J. S. Kang, S. McDonnell, S. KC, J. Guo, K. Cho, R. M. Wallace and A. Javey, *ACS Nano*, 2014, **8**, 10808–10814.

[177] F. Urban, N. Martucciello, L. Peters, N. McEvoy and A. Di Bartolomeo, *Nanomaterials*, 2018, **8**, 901.

[178] C. Zhang, C. Gong, Y. Nie, K.-A. Min, C. Liang, Y. J. Oh, H. Zhang, W. Wang, S. Hong, L. Colombo, R. M. Wallace and K. Cho, *2D Materials*, 2016, **4**, 015026.

[179] T. Roy, M. Tosun, J. S. Kang, A. B. Sachid, S. B. Desai, M. Hettick, C. C. Hu and A. Javey, *ACS Nano*, 2014, **8**, 6259–6264.

[180] D. Xiao, G.-B. Liu, W. Feng, X. Xu and W. Yao, *Physical Review Letters*, 2012, **108**, 196802.

[181] Y.-P. Gao, X. Wu, K.-J. Huang, L.-L. Xing, Y.-Y. Zhang and L. Liu, *CrystEngComm*, 2017, **19**, 404–418.

[182] D. Voiry, J. Yang and M. Chhowalla, *Advanced Materials*, 2016, **28**, 6197–6206.

[183] R. Gatensby, *Ph.D. thesis*, School of Chemistry, Trinity College Dublin, 2017.

[184] M. Placidi, M. Dimitrievska, V. Izquierdo-Roca, X. Fontane, A. Castellanos-Gomez, A. Perez-Tomas, N. Mestres, M. Espindola-Rodriguez, S. Lopez-Marino, M. Neuschitzer, V. Bermudez, A. Yaremko and A. Perez-Rodriguez, *2D Mater.*, 2015, **2**, 035006.

[185] W. Zhao, Z. Ghorannevis, K. K. Amara, J. R. Pang, M. Toh, X. Zhang, C. Kloc, P. H. Tan and G. Eda, *Nanoscale*, 2013, **5**, 9677.

[186] P. Tonndorf, R. Schmidt, P. Battger, X. Zhang, J. Barner, A. Liebig, M. Albrecht, C. Kloc, O. Gordan, D. R. T. Zahn and et al., *Optics Express*, 2013, **21**, 4908.

[187] S. Das, H.-Y. Chen, A. V. Penumatcha and J. Appenzeller, *Nano Lett.*, 2013, **13**, 100.

[188] S. Das and J. Appenzeller, *Appl. Phys. Lett.*, 2013, **103**, 103501.

[189] K.-K. Kam, *Retrospective Theses and Dissertations*, 1982, **8356**, 1.

[190] Y. Xue, Y. Zhang, Y. Liu, H. Liu, J. Song, J. Sophia, J. Liu, Z. Xu, Q. Xu, Z. Wang, J. Zheng, Y. Liu, S. Li and Q. Bao, *ACS Nano*, 2015, **10**, 573–580.

[191] H. Liu, S. Hussain, A. Ali, B. A. Naqvi, D. Vikraman, W. Jeong, W. Song, K.-S. An and J. Jung, *RSC Advances*, 2018, **8**, 25514–25518.

[192] D. Dumcenco, K. Chen, Y. Wang, Y. Huang and K. Tiong, *Journal of Alloys and Compounds*, 2010, **506**, 940–943.

[193] C. Roessler, *Zeitschrift für anorganische Chemie*, 1897, **15**, 405–411.

[194] A. Morette, *Compt. Rend*, 1942, **215**, 86.

[195] V. M. Goldschmidt, *Transactions of the Faraday Society*, 1929, **25**, 253.

[196] D. H. Keum, S. Cho, J. H. Kim, D.-H. Choe, H.-J. Sung, M. Kan, H. Kang, J.-Y. Hwang, S. W. Kim, H. Yang, K. J. Chang and Y. H. Lee, *Nature Physics*, 2015, **11**, 482–486.

[197] J. C. Park, S. J. Yun, H. Kim, J.-H. Park, S. H. Chae, S.-J. An, J.-G. Kim, S. M. Kim, K. K. Kim and Y. H. Lee, *ACS Nano*, 2015, **9**, 6548–6554.

[198] S. Cho, S. Kim, J. H. Kim, J. Zhao, J. Seok, D. H. Keum, J. Baik, D.-H. Choe, K. J. Chang, K. Suenaga, S. W. Kim, Y. H. Lee and H. Yang, *Science*, 2015, **349**, 625–628.

[199] M. C. Yarema, *PEDIATRICS*, 2005, **116**, e319–e321.

[200] L. S. Brooks, *Journal of the American Chemical Society*, 1952, **74**, 227–229.

[201] L.-F. Huang and Z. Zeng, *The Journal of Physical Chemistry C*, 2015, **119**, 18779–18789.

[202] X. Ma, P. Guo, C. Yi, Q. Yu, A. Zhang, J. Ji, Y. Tian, F. Jin, Y. Wang, K. Liu, T. Xia, Y. Shi and Q. Zhang, *Physical Review B*, 2016, **94**, 214105.

[203] Q. Song, H. Wang, X. Pan, X. Xu, Y. Wang, Y. Li, F. Song, X. Wan, Y. Ye and L. Dai, *Scientific Reports*, 2017, **7**, 1758.

[204] B. Chen, H. Sahin, A. Suslu, L. Ding, M. I. Bertoni, F. M. Peeters and S. Tongay, *ACS Nano*, 2015, **9**, 5326–5332.

[205] G. Mirabelli, C. McGeough, M. Schmidt, E. K. McCarthy, S. Monaghan, I. M. Povey, M. McCarthy, F. Gity, R. Nagle, G. Hughes, A. Cafolla, P. K. Hurley and R. Duffy, *Journal of Applied Physics*, 2016, **120**, 125102.

[206] F. Ye, J. Lee, J. Hu, Z. Mao, J. Wei and P. X.-L. Feng, *Small*, 2016, **12**, 5802–5808.

[207] A. Roy, H. C. P. Movva, B. Satpati, K. Kim, R. Dey, A. Rai, T. Pramanik, S. Guchhait, E. Tutuc and S. K. Banerjee, *ACS Applied Materials & Interfaces*, 2016, **8**, 7396–7402.

[208] M. Camacho-López, L. Escobar-Alarcón, M. Picquart, R. Arroyo, G. Córdoba and E. Haro-Poniatowski, *Optical Materials*, 2011, **33**, 480–484.

[209] B. Predel, in *Li-Mg – Nd-Zr*, Springer-Verlag, pp. 1–3.

[210] Y. Yoo, Z. P. DeGregorio, Y. Su, S. J. Koester and J. E. Johns, *Advanced Materials*, 2017, **29**, 1605461.

[211] J.-H. Huang, K.-Y. Deng, P.-S. Liu, C.-T. Wu, C.-T. Chou, W.-H. Chang, Y.-J. Lee and T.-H. Hou, *Advanced Materials Interfaces*, 2017, **4**, 1700157.

[212] J. E. Callanan, G. Hope, R. D. Weir and E. F. Westrum, *The Journal of Chemical Thermodynamics*, 1992, **24**, 627–638.

[213] S. K. Srivastava and B. N. Avasthi, *Journal of Materials Science*, 1985, **20**, 3801–3815.

[214] H. Zhu, Q. Wang, L. Cheng, R. Addou, J. Kim, M. J. Kim and R. M. Wallace, *ACS Nano*, 2017, **11**, 11005–11014.

[215] X. Zheng, Y. Wei, C. Deng, H. Huang, Y. Yu, G. Wang, G. Peng, Z. Zhu, Y. Zhang, T. Jiang, S. Qin, R. Zhang and X. Zhang, *ACS Applied Materials & Interfaces*, 2018, **10**, 30045–30050.

[216] H. C. Diaz, R. Chaghi, Y. Ma and M. Batzill, *2D Materials*, 2015, **2**, 044010.

[217] L. Yang, H. Wu, W. Zhang, Z. Chen, J. Li, X. Lou, Z. Xie, R. Zhu and H. Chang, *Nanoscale*, 2018, **10**, 19906–19915.

[218] Y. Tan, F. Luo, M. Zhu, X. Xu, Y. Ye, B. Li, G. Wang, W. Luo, X. Zheng, N. Wu, Y. Yu, S. Qin and X.-A. Zhang, *Nanoscale*, 2018, **10**, 19964–19971.

[219] V. Rodriguez, M. Couzi, F. Adamietz, M. Dussauze, G. Guery, T. Cardinal, P. Veber, K. Richardson and P. Thomas, *Journal of Raman Spectroscopy*, 2013, **44**, 739–745.

[220] M. Mazzuca, J. Portier, B. Tanguy, F. Romain, A. Fadli and S. Turrell, *Journal of Molecular Structure*, 1995, **349**, 413–416.

[221] J. Champarnaud-Mesjard, S. Blanchandin, P. Thomas, A. Mirgorodsky, T. Merle-Méjean and B. Frit, *Journal of Physics and Chemistry of Solids*, 2000, **61**, 1499–1507.

[222] Y. C. Her and S. L. Huang, *Nanotechnology*, 2013, **24**, 215603.

[223] A. S. Pine and G. Dresselhaus, *Physical Review B*, 1971, **4**, 356–371.

[224] M. H. Brodsky, R. J. Gambino, J. E. Smith and Y. Yacoby, *Physica Status Solidi (b)*, 1972, **52**, 609–614.

[225] Y. Du, G. Qiu, Y. Wang, M. Si, X. Xu, W. Wu and P. D. Ye, *Nano Letters*, 2017, **17**, 3965–3973.

[226] M. R. Laskar, L. Ma, S. Kannappan, P. S. Park, S. Krishnamoorthy, D. N. Nath, W. Lu, Y. Wu and S. Rajan, *Applied Physics Letters*, 2013, **102**, 252108.

[227] T. J. Trentler, K. M. Hickman, S. C. Goel, A. M. Viano, P. C. Gibbons and W. E. Buhro, *Science*, 1995, **270**, 1791–1794.

[228] X. Chia, A. Y. S. Eng, A. Ambrosi, S. M. Tan and M. Pumera, *Chemical Reviews*, 2015, **115**, 11941–11966.

[229] Q. Tang and D. en Jiang, *ACS Catalysis*, 2016, **6**, 4953–4961.

[230] D. McAteer, Z. Gholamvand, N. McEvoy, A. Harvey, E. O'Malley, G. S. Duesberg and J. N. Coleman, *ACS Nano*, 2015, **10**, 672–683.

[231] H. Nolan, N. McEvoy, M. O'Brien, N. C. Berner, C. Yim, T. Hallam, A. R. McDonald and G. S. Duesberg, *Nanoscale*, 2014, **6**, 8185.

[232] T. Kosmala, H. C. Diaz, H.-P. Komsa, Y. Ma, A. V. Krasheninnikov, M. Batzill and S. Agnoli, *Advanced Energy Materials*, 2018, **8**, 1800031.

[233] J. Seok, J.-H. Lee, S. Cho, B. Ji, H. W. Kim, M. Kwon, D. Kim, Y.-M. Kim, S. H. Oh, S. W. Kim, Y. H. Lee, Y.-W. Son and H. Yang, *2D Materials*, 2017, **4**, 025061.

[234] O. Knop and H. Haraldsen, *Canadian Journal of Chemistry*, 1956, **34**, 1142–1145.

[235] J. A. Champion, *British Journal of Applied Physics*, 1965, **16**, 1035–1037.

[236] S. Kabashima, *Journal of the Physical Society of Japan*, 1966, **21**, 945–948.

[237] J. P. Troadec, D. Bideau and E. Guyon, *Journal of Physics C: Solid State Physics*, 1981, **14**, 4807–4819.

[238] L. Wang, I. Gutiérrez-Lezama, C. Barreteau, N. Ubrig, E. Giannini and A. F. Morpurgo, *Nature Communications*, 2015, **6**, 9892.

[239] A. A. Soluyanov, D. Gresch, Z. Wang, Q. Wu, M. Troyer, X. Dai and B. A. Bernevig, *Nature*, 2015, **527**, 495–498.

[240] A. J. Frenzel, C. C. Homes, Q. D. Gibson, Y. M. Shao, K. W. Post, A. Charnukha, R. J. Cava and D. N. Basov, *Physical Review B*, 2017, **95**, 245140.

[241] Y. Cao, N. Sheremetyeva, L. Liang, H. Yuan, T. Zhong, V. Meunier and M. Pan, *2D Materials*, 2017, **4**, 035024.

[242] Y. C. Jiang, J. Gao and L. Wang, *Scientific Reports*, 2016, **6**, 19624.

[243] W. Yang, Z.-Y. Yuan, Y.-Q. Luo, Y. Yang, F.-W. Zheng, Z.-H. Hu, X.-H. Wang, Y.-A. Liu and P. Zhang.

[244] G. Kukucska and J. Koltai, *physica status solidi (b)*, 2017, **254**, 1700184.

[245] J. X. Gong, J. Yang, M. Ge, Y. J. Wang, D. D. Liang, L. Luo, X. Yan, W. L. Zhen, S. R. Weng, L. Pi, C. J. Zhang and W. K. Zhu.

[246] J. M. Woods, J. Shen, P. Kumaravadivel, Y. Pang, Y. Xie, G. A. Pan, M. Li, E. I. Altman, L. Lu and J. J. Cha, *ACS Applied Materials & Interfaces*, 2017, **9**, 23175–23180.

[247] B. Predel, in *Pu-Re – Zn-Zr*, Springer-Verlag, pp. 1–2.

[248] L. Vitos, A. Ruban, H. Skriver and J. Kollár, *Surface Science*, 1998, **411**, 186–202.

[249] A. Papakondylis and P. Sautet, *The Journal of Physical Chemistry*, 1996, **100**, 10681–10688.

[250] L. Jones, H. Yang, T. J. Pennycook, M. S. J. Marshall, S. V. Aert, N. D. Browning, M. R. Castell and P. D. Nellist, *Advanced Structural and Chemical Imaging*, 2015, **1**, 8.

[251] M. Lai, J.-H. Lim, S. Mubeen, Y. Rheem, A. Mulchandani, M. A. Deshusses and N. V. Myung, *Nanotechnology*, 2009, **20**, 185602.

[252] H. L. Zhuang and R. G. Hennig, *The Journal of Physical Chemistry C*, 2013, **117**, 20440–20445.

[253] D. Zhao, S. Xie, Y. Wang, H. Zhu, L. Chen, Q. Sun and D. W. Zhang, *AIP Advances*, 2019, **9**, 025225.

[254] Y. Wang, L. Li, W. Yao, S. Song, J. T. Sun, J. Pan, X. Ren, C. Li, E. Okunishi, Y.-Q. Wang, E. Wang, Y. Shao, Y. Y. Zhang, H. tao Yang, E. F. Schwier, H. Iwasawa, K. Shimada, M. Taniguchi, Z. Cheng, S. Zhou, S. Du, S. J. Pennycook, S. T. Pantelides and H.-J. Gao, *Nano Letters*, 2015, **15**, 4013–4018.

[255] A. Politano, G. Chiarello, B. Ghosh, K. Sadhukhan, C.-N. Kuo, C. S. Lue, V. Pellegrini and A. Agarwal, *Physical Review Letters*, 2018, **121**, 086804.

[256] M. F. Thomas L.Wright, *Geological Survey Bulletin*, 1949, **1213**, 1.

[257] E. F. Westrum, H. G. Carlson, F. Gr⊘nvold and A. Kjekshus, *The Journal of Chemical Physics*, 1961, **35**, 1670–1676.

[258] P. J. Orders, J. Liesegang, R. C. G. Leckey, J. G. Jenkin and J. D. Riley, *Journal of Physics F: Metal Physics*, 1982, **12**, 2737–2753.

[259] G. Y. Guo and W. Y. Liang, *Journal of Physics C: Solid State Physics*, 1986, **19**, 5365–5380.

[260] M. Yan, H. Huang, K. Zhang, E. Wang, W. Yao, K. Deng, G. Wan, H. Zhang, M. Arita, H. Yang, Z. Sun, H. Yao, Y. Wu, S. Fan, W. Duan and S. Zhou, *Nature Communications*, 2017, **8**, 257.

[261] D. Fu, X. Bo, F. Fei, B. Wu, M. Gao, X. Wang, M. Naveed, S. A. Shah, H. Bu, B. Wang, L. Cao, W. Zou, X. Wan and F. Song, *Physical Review B*, 2018, **97**, 245109.

[262] Y. Wu, D. Mou, N. H. Jo, K. Sun, L. Huang, S. L. Bud'ko, P. C. Canfield and A. Kaminski, *Physical Review B*, 2016, **94**, 121113.

[263] F. Fei, X. Bo, R. Wang, B. Wu, J. Jiang, D. Fu, M. Gao, H. Zheng, Y. Chen, X. Wang, H. Bu, F. Song, X. Wan, B. Wang and G. Wang, *Physical Review B*, 2017, **96**, 041201.

[264] F. Liu, J. Li, K. Zhang, S. Peng, H. Huang, M. Yan, N. Li, Q. Zhang, S. Guo, X. Lü, P. Cai, L. Yin, S. Zhou, W. Duan, J. Shen and W. Yang, *Science China Physics, Mechanics & Astronomy*, 2018, **62**, 48211.

[265] B. Ghosh, F. Alessandro, M. Zappia, R. Brescia, C.-N. Kuo, C. S. Lue, G. Chiarello, A. Politano, L. S. Caputi, A. Agarwal and A. Cupolillo, *Physical Review B*, 2019, **99**, 045414.

[266] X. Chia, A. Adriano, P. Lazar, Z. Sofer, J. Luxa and M. Pumera, *Advanced Functional Materials*, 2016, **26**, 4306–4318.

[267] X. Chia, Z. Sofer, J. Luxa and M. Pumera, *ACS Applied Materials & Interfaces*, 2017, **9**, 25587–25599.

[268] H. Huang, X. Fan, D. J. Singh and W. Zheng, *ACS Omega*, 2018, **3**, 10058–10065.

[269] G. W. Graham, W. H. Weber, J. R. McBride and C. R. Peters, *Journal of Raman Spectroscopy*, 1991, **22**, 1–9.

[270] W.-S. Kim, *Metals and Materials*, 1996, **2**, 9–14.

[271] Y. Zhao, J. Qiao, P. Yu, Z. Hu, Z. Lin, S. P. Lau, Z. Liu, W. Ji and Y. Chai, *Advanced Materials*, 2016, **28**, 2399–2407.

[272] D. Hu, T. Zhao, X. Ping, H. Zheng, L. Xing, X. Liu, J. Zheng, L. Sun, C. Tao, L. Gu, D. Wang and L. Jiao, *Angewandte Chemie*, 2019.

[273] S. Lin, Y. Liu, Z. Hu, W. Lu, C. H. Mak, L. Zeng, J. Zhao, Y. Li, F. Yan, Y. H. Tsang, X. Zhang and S. P. Lau, *Nano Energy*, 2017, **42**, 26–33.

[274] M. K. Kundu, T. Bhowmik, R. Mishra and S. Barman, *ChemSusChem*, 2018, **11**, 2388–2401.

[275] Y. Zhan, Y. Li, Z. Yang, X. Wu, M. Ge, X. Zhou, J. Hou, X. Zheng, Y. Lai, R. Pang, H. Duan, X. Chen, H. Nie and S. Huang, *Advanced Science*, 2019, **6**, 1801663.